

PIER MOMENT-ROTATION OF COMPACT AND
NONCOMPACT HPS70W I-GIRDERS

Bryan A. Hartnagel, Ph.D., P.E.

An Vinh Tran, Ph.D.

June 2003

ACKNOWLEDGEMENTS

The authors gratefully acknowledge the sponsors of the project and Colorado State University. The project would not have been a success without generous funding from Mountain Plains Consortium, steel plate donations from Bethlehem Lukens Plate, a division of Bethlehem Steel Corporation, Burns Harbor, Indiana, and girder fabrication from Zimmerman Metals, Inc., Denver, CO. The authors would like to sincerely thank the faculty and staff of Colorado State University (CSU), College of Engineering, and Department of Civil Engineering for their support. The authors also express their appreciation to all technical staff and students working at the Structures Lab of the Engineering Research Center – CSU, especially Horacio Garza Jr., Dr. Abdalla Shigidi, Michael Griffeth, and Brian Valentine, for their assistance in the experiments of the project. The authors also owe thanks to Hibbitt, Karlsson & Sorensen, Inc. and the Academic Computing and Networking Services – CSU for providing the ABAQUS finite element program useful in the numerical analysis of the project.

DISCLAIMER

The contents of this report reflect the views of the authors, who are responsible for the facts and the accuracy of the information presented. This document is disseminated under the sponsorship of the

Department of Transportation, University Centers Program, in the interest of information exchange. The U.S. Government assumes no liability for the contents or use thereof.

ABSTRACT

A project to study the pier moment-rotation behavior of compact and noncompact high performance steel HPS70W bridge I-girders was conducted at Colorado State University in the context of examining two restrictions for inelastic design of steel bridge girders in the current edition of the AASHTO LRFD bridge code (AASHTO 1998, and interims through 2001). The first restriction is that inelastic design involving the moment-rotation relationship of steel girders with a yield strength exceeding 50 ksi is prohibited. The second restriction is that the AASHTO LRFD inelastic design methods cannot be used on girders that do not meet the compactness requirements stated in the provisions. To determine whether or not these restrictions should be modified, examination of the pier moment-rotation behavior of HPS70W I-shape girders was undertaken through large-scale laboratory testing and finite element simulation.

The experimental and numerical responses agree well and thus validate the numerical model. These results also show that compact/noncompact and composite/noncomposite HPS70W I-girders have the strength and ductility suitable for the application of inelastic analysis and design. This research suggests that the two restrictions for inelastic design of steel bridge girders in the current AASHTO LRFD bridge code should be modified for such girders. This work also demonstrates that the proposed Improved Simplified Inelastic Design (ISID) procedures (Barth, Hartnagel, White, and Barker, 2001) are suitable for high performance steel, HPS70W, compact and noncompact I-girders.

TABLE OF CONTENTS

1. INTRODUCTION.....	1
1.1 Introduction.....	1
1.2 Purpose and Objectives	1
1.3 Significance of the Study.....	2
1.4 Report Organization.....	2
2. LABORATORY TESTS OF HPS70W I-GIRDERS.....	3
2.1 Background.....	3
2.1.1 AASHTO Requirements of Compact Section Slenderness, Bearing Stiffener, and Lateral Bracing Locations	3
2.1.2 Current AASHTO LRFD Moment-Inelastic Rotation Provision.....	5
2.1.3 Typical Moment-Rotation of Simply Supported Steel Girder.....	6
2.1.4 Correlation Between the Pier Moment Region & a Simple-Span Specimen ...	8
2.2 Large-Scale HPS70W Girder Tests.....	9
2.2.1 Compact/Noncompact Girder Dimensions	10
2.2.2 Testing Apparatus Design and Overhaul	12
2.2.3 Specimen Instrumentation and Measurement.....	16
2.2.4 Test Procedures.....	20
2.2.5 Experimental Study of Bracing Lengths for Specimen #4.....	27
2.3 Experimental Examining the Stress-Strain Relationship for HPS70W.....	27
2.3.1 Tensile Rests on Flange and Web Samples of HPS70W	27
2.3.2 Material Tested Data of HPS70W Plates: A Query for “Nominal Compact” Classification and Calculation for Plastic Moments.....	30
3. NUMERICAL MODELS FOR HPS70W I-GIRDERS.....	31
3.1 Introduction	31
3.2 Numerical Moment-Rotation of Noncomposite HPS70W Girders.....	32
3.2.1 Implementation of ABAQUS Finite Element Code	32
3.2.2 Material Inputs for Numerical Analyses of HPS70W Girders	37
3.2.3 Inputs of Initial Imperfections and Residual Stresses for Numerical Models	41
3.2.4 Numerical Studies of Bracing Lengths for Specimens #3 and #4.....	45
4. PIER MOMENT-ROTATION OF COMPACT AND NONCOMPACT HPS70W I-GIRDERS.....	49
4.1 Introduction.....	49
4.2 Inelastic Moment-Rotation Relationships of CSU’s HPS70W Noncomposite Specimens	55
4.3 Bracing Lengths: Numerical Effects for Specimens #3 and Experimental and Numerical Effects For Specimen #4.....	65
5. SUMMARY AND CONCLUSION.....	69
5.1 Introduction	69
5.2 Pier Moment-Rotation Behavior of HPSW I-Girders.....	69
5.2.1 Effect of Compact or Noncompact Steel Section	70
5.2.2 Effect of Bracing Length.....	70
5.2.3 Effect of Initial Residual Stress and Initial Geometric Imperfection	70
5.3 Summary and Conclusion	71

6. REFERENCES.....	73
7. NOTATION.....	75
8. APPENDIX.....	77

LIST OF TABLES

Table 2.2.1.1	CSU Compact Girder Dimensions	10
Table 2.2.1.2	CSU Noncompact Girder Dimensions	11
Table 2.2.2.1	CSU Testing Apparatus Summary	13
Table 3.2.1.1	Half-Length Numerical Model Properties.....	37
Table 3.2.2.1	HPS70W Material Inputs for Numerical Moment-Rotation Analyses.....	39
Table 3.2.3.1	Distribution of Initial Residual Stresses for Specimen #1	41
Table 3.2.3.2	Distribution of Initial Residual Stresses for Specimen #2	41
Table 3.2.3.3	Distribution of Initial Residual Stresses for Specimens #3 and #4.....	42
Table 4.2.1	Nominal Plastic Moment, M_p , and AASHTO Effective Moment, M_{pe}	62
Table 4.2.2	Actual Plastic Moment, M_p , and AASHTO Effective Moment, M_{pe}	62
Table 4.2.3	Summary of AASHTO Predicted Comparisons for CSU Girders	63
Table 4.2.4	Nominal ISID Design Moment, M_n , and Effective Moment, $M_{pe(30)}$	64
Table 4.2.5	Actual ISID Design Moment, M_n , and Effective Moment, $M_{pe(30)}$	64
Table 4.2.6	Summary of ISID Predicted Comparisons for CSU Girders.....	64

LIST OF FIGURES

Figure 2.1.2.1	AASHTO 6.10.10.2.4d	5
Figure 2.1.3.1	A Typical Moment-Rotation Curve for a Simple Span Girder with Adequate Lateral Bracing Provided.....	7
Figure 2.1.4.1	Correlation Between the Negative Moment Region Near a Pier in a Continuous Span Girder and the Experimental Test Girder.....	8
Figure 2.1.4.2	Plastic Rotation Analogy	9
Figure 2.2.2.1	Overall Testing Apparatus at CSU Structural Engineering Lab.....	12
Figure 2.2.2.2	LVDTs, Actuators, Distributor Beam, and the Load Frame Bracing	13
Figure 2.2.2.3	Load Bearing Point.....	14
Figure 2.2.2.4	Testing Apparatus and Bracing Cross-View Configuration.....	15
Figure 2.2.2.5	Testing Apparatus and Girder Bracing Longitudinal Configuration.....	15
Figure 2.2.2.6	Reaction Bracing and Supports.....	16
Figure 2.2.3.1	Specimen #1 - Instrumentation Locations	17
Figure 2.2.3.2	Specimen #2 - Instrumentation Locations	18
Figure 2.2.3.3	Specimen #3 - Instrumentation Locations	18
Figure 2.2.3.4	Specimen #4 - Instrumentation Locations	19
Figure 2.2.3.5	Left: Midspan Arrangement for Specimens #3 and #4 Right: Typical End Rotation Measurement Instrumentation.....	19
Figure 2.2.3.6	Midspan Arrangement for Specimen #1 and 2.....	20
Figure 2.2.4.1	States of Midspan Deformed Shape of Specimen #1.....	23
Figure 2.2.4.2	Final Deformed Shapes of Specimen #1.....	24
Figure 2.2.4.3	Final Deformed Shapes of Specimen #2.....	25
Figure 2.2.4.4	Above: Midspan Deformed Shape of Specimen #3 Below: Specimen #4 after First Tested.....	26
Figure 2.3.1.1	Flange Samples of HPS70W for Uniaxial Tensile Tests - Parallel to Rolling Direction.....	28
Figure 2.3.1.2	Flange Samples of HPS70W for Uniaxial Tensile Tests - Perpendicular to Rolling Direction.....	28

Figure 2.3.1.3	Web Samples of HPS70W for Uniaxial Tensile Tests - Parallel to Rolling Direction.....	29
Figure 2.3.1.4	Web Samples of HPS70W for Uniaxial Tensile Tests - Perpendicular to Rolling Direction.....	29
Figure 3.2.1.1	Initial and Deformed Shapes of FEM Model for CSU Specimen #1.....	33
Figure 3.2.1.2	Initial and Deformed Shapes of FEM Model for CSU Specimen #2.....	34
Figure 3.2.1.3	Initial and Deformed Shapes of FEM Model for CSU Specimen #3.....	35
Figure 3.2.1.4	Initial and Deformed Shapes of FEM Model for CSU Specimen #4.....	36
Figure 3.2.2.1	Statistical Data of the Yield Strength, Ultimate Strength, and Yield Ratio for HPS70 Plates.....	38
Figure 3.2.2.2	Experimental Engineering Stress-Strain Relationship for the Flanges as Material Inputs for Numerical Analyses of HPS70W Girders	40
Figure 3.2.2.3	Experimental Engineering Stress-Strain Relationship for the Web as Material Inputs for Numerical Analyses of HPS70W Girders	40
Figure 3.2.3.1	The First Four Eigenmodes of Buckling Analysis for Specimen #1.....	43
Figure 3.2.3.2	The First Four Eigenmodes of Buckling Analysis for Specimen #2.....	43
Figure 3.2.3.3	The First Four Eigenmodes of Buckling Analysis for Specimen #3.....	44
Figure 3.2.3.4	The First Four Eigenmodes of Buckling Analysis for Specimen #4.....	44
Figure 4.1.1	Linear Strain Distributions through Cross-Section and Elastic Neutral Axis for Specimen #1	50
Figure 4.1.2	Linear Strain Distributions through Cross-Section and Elastic Neutral Axis for Specimen #2.....	50
Figure 4.1.3	Linear Strain Distributions through Cross-Section and Elastic Neutral Axis for Specimen #3.....	51
Figure 4.1.4	Linear Strain Distributions through Cross-Section and Elastic Neutral Axis for Specimen #4.....	51
Figure 4.1.5	Specimen #1 - Numerical Moment-Total Rotation and Moment-Elastic Rotation at Different Locations Near the Supports	52
Figure 4.1.6	Specimen #2 - Numerical Moment-Total Rotation and Moment-Elastic Rotation at Different Locations Near the Supports	53

Figure 4.1.7	Effects of Residual Stresses and Initial Imperfection on Numerical Models of Specimen #1 and Specimen #2.....	54
Figure 4.2.1	Nominal and Actual Rotational Capacity, R, of Specimen #1	56
Figure 4.2.2	AASHTO Predicted Comparison for Specimen #1, Nominally and Actually ...	57
Figure 4.2.3	Nominal and Actual Rotational Capacity, R, of Specimen #2	58
Figure 4.2.4	AASHTO Predicted Comparison for Specimen #2, Nominally and Actually ...	59
Figure 4.2.5	AASHTO predicted comparison for Specimen #3, Nominally and Actually	60
Figure 4.2.6	AASHTO predicted comparison for Specimen #4, Nominally and Actually	61
Figure 4.3.1	Numerical Effects of Bracing Lengths on Moment-Rotation Relationship for Specimen #3.....	66
Figure 4.3.2	Experimental and Numerical Effects of Bracing Lengths on Moment-Rotation for Specimen #4.....	67

EXECUTIVE SUMMARY

Inelastic analysis and design offers the potential for significant cost savings since it accounts for the reserve strength inherent in continuous-span steel girder bridges. Inelastic procedures allow for the yielding of entire steel cross sections to occur at the interior supports and permit moment-redistribution from negative pier moments to positive moment regions. Since the moment-redistribution causes slight inelastic rotation at the pier regions, small permanent deflection, and some residual moments, the bridge is still serviceable. After an initial overload, deformations stabilize, the structure achieves shakedown, and future loads will be resisted elastically.

A project to study the pier moment-rotation behavior of compact and noncompact high performance steel HPS70W I-girders was conducted at Colorado State University in the context of examining two restrictions for inelastic design of steel bridge girders in the current edition of the AASHTO LRFD bridge code (AASHTO,1998 and interims through 2001). The first restriction is that inelastic design involving the moment-rotation relationship of steel girders with a yield strength exceeding 50 ksi is prohibited, although, bridge designers are currently allowed to go to plastic moment for I-girders having a yield strength of 70 ksi. The second restriction is that the AASHTO LRFD inelastic design methods cannot be used on girders that do not meet the compactness requirements stated in the provisions.

To determine whether or not these restrictions should be modified, examination of the pier moment-rotation behavior of HPS70W I-shape girders was undertaken through experimental testing and numerical modeling. Large-scale laboratory experiments were performed for noncomposite girders. Finite element models of the tested specimens were then analyzed based on the material inputs obtained from experimental examination of the stress-strain relationships for HPS70W. The inelastic moment-rotation behavior of HPS70W girders was determined both experimentally and numerically.

The experimental and numerical responses agree well and thus validate the numerical model. These results also show that compact/noncompact and composite/noncomposite HPS70W I-girders have the strength and ductility suitable for the application of inelastic analysis and design. This research suggests that the two restrictions for inelastic design of steel bridge girders in the current AASHTO LRFD bridge design specifications (AASHTO 1998, and interims through 2001) should be modified for such girders. This work also demonstrates that the proposed improved simplified inelastic design (ISID) procedures (Barth, Hartnagel, White, and Barker, 2001) are suitable for high performance steel, HPS70W, compact and noncompact I-girders.

1. INTRODUCTION

1.1 Introduction

Inelastic design of steel bridge girders offers the potential for significant cost savings because it accounts for the true strength of a bridge, which is often considerably above the strength predicted by elastic or pseudo-plastic procedures used in present bridge specifications (Hartnagel, 1997). On the other hand, the 1998 version of the Load and Resistance Factor Design (LRFD) specifications of the American Association of State Highway and Transportation Officials (AASHTO) forbid inelastic design procedures for steel plate girders having a specified minimum nominal yield stress of steel, F_y , exceeding 50 ksi. The 1998 version of AASHTO LRFD 2nd Edition also limited the nominal flexural strength, M_n , of steel plate girders having F_y exceeding 50 ksi to the yield moment capacity, M_y , rather than the plastic moment capacity, M_p (AASHTO 1998). Nonetheless, evidence from current research on high performance steel (HPS) initiated the consideration to account inelastic strength with the limitation of plastic moment capacity, M_p . Additionally, the interim 2001 specifications of AASHTO LRFD 2nd Edition now allow steel plate girders having $F_y \leq 70$ ksi to reach M_p (AASHTO interim 2001) provided certain restrictions are met. In an effort to determine whether or not bridge designers can take advantage of the inherent properties of HPS, this research will specially focus on I-shape plate girders fabricated from ASTM A709 HPS70W steel, a HPS with a nominal yield stress of 70 ksi.

In brief, high performance steel (HPS) contains less carbon than conventional steel, leading to an increase in its weldability and toughness. Additional alloying ingredients contribute to its superior weathering characteristics. A thermo-mechanical controlled process of essentially quenching and tempering provides the gain of additional strength. HPS weathering steel is suitable for use in the unpainted condition, and this gives designers the option to reduce painting and associated maintenance in many bridge locations.

1.2 Purpose and Objectives

The purpose of this research is to study the pier moment-rotation behavior of compact and noncompact I-shape bridge girders fabricated from high performance steel HPS70W. To accomplish the purpose, the research consists of two main objectives.

The first objective of this research is to compare experimental laboratory moment-rotation tests and corresponding numerical moment-rotation finite element analysis of HPS70W steel components to current AASHTO LRFD moment-rotation equations (AASHTO, 1998 and interims through 2001). The second objective is to compare the experimental and numerical results to a recently proposed improved simplified inelastic design (Barth, et al., 2001).

The tasks necessary to complete the objectives of the research are:

1. Experimental tasks: Four various length and size HPS70W I-shape steel girders are tested in the common simply supported configuration, which models upside down the interior support regions of continuous girders (see Chapter 2, Figure 2.1.4.1). The first two girders meet compact section slenderness requirements for flange and web elements as presented in AASHTO LRFD (AASHTO, 1998 and interims through 2001). The other two girders are samples of noncompact sections; specifically, the web is noncompact.

2. Numerical tasks: Establish finite element models corresponding to the four tested HPS70W I-shape steel girders.

3. Analysis and synthesis task: Compare the results obtained from experimental works and numerical works to determine the pier moment-rotation behavior of HPS70W I-shape steel girders. Compare the results to current AASHTO LRFD moment-rotation specifications and the proposed inelastic design provision to provide conclusions and suggestions.

1.3 Significance of the Study

Inelastic analysis and design procedures permit more economical I-shape girders to be used. Inelastic procedures allow for the yielding of entire steel cross sections to occur at interior supports of continuous span I-shape bridge girders. Plastic hinges that form at piers, however, must have adequate ductility so that the plastic hinges don't unload before the theoretical plastic strength of the bridge girder is reached. As a result, inelastic rotation at the piers permits moment-redistribution from negative pier moments to positive moment regions. Since the moment-redistribution causes slight inelastic rotation at the pier regions, small permanent deflection, and some residual moments, the bridge is still serviceable. After an initial overload, deformations stabilize, the structure achieves shakedown, and future loads will be resisted elastically.

However, according to AASHTO inelastic design procedures for the service limit state control of permanent deflection (AASHTO, 1998 and interims through 2001), the moment-rotation behavior of I-shape girders constructed of steel having F_y greater than 50 ksi has not been sufficiently documented to permit the use of inelastic analysis procedures for M_p . In other words, for I-shape girders having a specified minimum nominal yield stress of steel, F_y , of 70 ksi, bridge designers can allow cross sections to reach the plastic moment capacity, M_p , but they still cannot use inelastic analysis. To effectively determine whether or not the current restriction applies to bridge girders fabricated from HPS70W steel plates, it is necessary to clarify the pier moment-rotation behavior of HPS70W I-shape girders. Consequently, the pier moment-rotation behavior will document whether geometric failure or material failure occurs first in compact HPS girders.

1.4 Report Organization

This research report consists of five chapters. Chapter 1 provides a description of the purpose of the study and a rationale for its significance. Chapter 2 describes the laboratory tests for the four noncomposite compact/noncompact HPS70W girders. Chapter 3 details the finite element models corresponding to the HPS70W girders. In Chapter 4, experimental and numerical findings of moment-rotation of HPS70W will be synthesized to develop the moment-rotation behavior compared to current AASHTO LRFD moment-rotation specifications and the proposed inelastic design provision. Chapter 5 then summarizes the important results and presents conclusions of this research. In addition, References provides relevant publications and Notation defines the symbols used for the main terminologies in this research. Finally, Appendix presents the plastic moments of various sections for the analysis in this study.

2. LABORATORY TESTS OF HPS70W I-GIRDERS

2.1 Background

The purpose of this research is to study the pier moment-rotation behavior of compact and noncompact I-shape HPS bridge girders, examining two restrictions for inelastic design of steel bridge girders in the current edition of the AASHTO LRFD bridge design specifications. First, inelastic design involving the moment-rotation relationship of steel girders, with a minimum specified yield strength of steel, F_y , exceeding 50 ksi, is prohibited (AASHTO, 1998 and interims through 2001). Second, the available AASHTO LRFD inelastic design methods cannot be used on girders that do not meet the compactness requirements stated in the provisions.

2.1.1 AASHTO Requirements of Compact Section Slenderness, Bearing Stiffener, and Lateral Bracing Locations

First, as specified by AASHTO, the compact section requirements for the web and the flange, respectively, are:

$$\frac{2D_{cp}}{t_w} \leq 3.76 \sqrt{\frac{E}{F_{yc}}} \quad (\text{AASHTO 6.10.4.1.2})$$

$$\frac{b_f}{2t_f} \leq 0.382 \sqrt{\frac{E}{F_{yc}}} \quad (\text{AASHTO 6.10.4.1.3})$$

where:

- D_{cp} = depth of web in compression at plastic moment (in.),
- t_w = web thickness (in.),
- b_f = width of compression flange (in.),
- t_f = thickness of compression flange (in.),
- E = modulus of elasticity of steel, and
- F_{yc} = specified minimum yield strength of the compression flange.

Second, bearing stiffeners shall be placed on the webs of plate girders at all bearing locations and at all locations supporting concentrated loads, and the stiffeners shall extend the full depth of the web and, as closely as practical, to the outer edges of the flanges (AASHTO 6.10.8.2). AASHTO recommends the width, b_s (in.), of each projecting stiffener element shall satisfy:

$$b_t \leq 0.48t_p \sqrt{\frac{E}{F_{ys}}} \quad (\text{AASHTO 6.10.8.2.2})$$

where:

t_p = thickness of stiffener (in.),

F_{ys} = yield strength of stiffener (ksi).

Third, lateral bracing along the compression flange prevents lateral torsional buckling and thus ensures that a girder meeting compact section requirements can reach its inherent plastic moment capacity. In three-point loading, the midspan (at the load point) is the most critical region of a girder for lateral torsional buckling. As a result, lateral bracing is first provided at the midspan of the test girders, and the compression flange bracing from the load point to the next compression flange brace is checked against the maximum unbraced length permitted by AASHTO. The maximum unbraced length, L_b , for compact section is:

$$L_b \leq \left(0.124 - 0.0759 \left(\frac{M_l}{M_p} \right) \right) \left(\frac{r_y E}{F_{yc}} \right) \quad (\text{AASHTO 6.10.4.1.7})$$

where:

L_b = unbraced length (in.),

r_y = radius of gyration about the weak bending axis (in.),

M_l = lower factored moment at either end of the unbraced length (kip-in),

M_p = plastic moment (kip-in),

F_{yc} = compression flange yield strength (ksi), and

E = modulus of elasticity (ksi).

In addition, the maximum unbraced length, L_b , for noncompact section is:

$$L_b \leq L_p = 1.76 r_t \sqrt{\frac{E}{F_{yc}}} \quad (\text{AASHTO 6.10.4.1.8})$$

where:

L_b = unbraced length (in.),

L_p = maximum unbraced length (in.),

r_t = radius of gyration about the weak bending axis of the area of the compression flange plus 1/3 area of the web in compression (in.),

F_{yc} = compression flange yield strength (ksi), and

E = modulus of elasticity (ksi).

2.1.2 Current AASHTO LRFD Moment-Inelastic Rotation Provision

Figure 2.1.2.1 shows the current AASHTO LRFD moment-rotation provision, which plots the normalized nominal plastic moment versus plastic rotation.

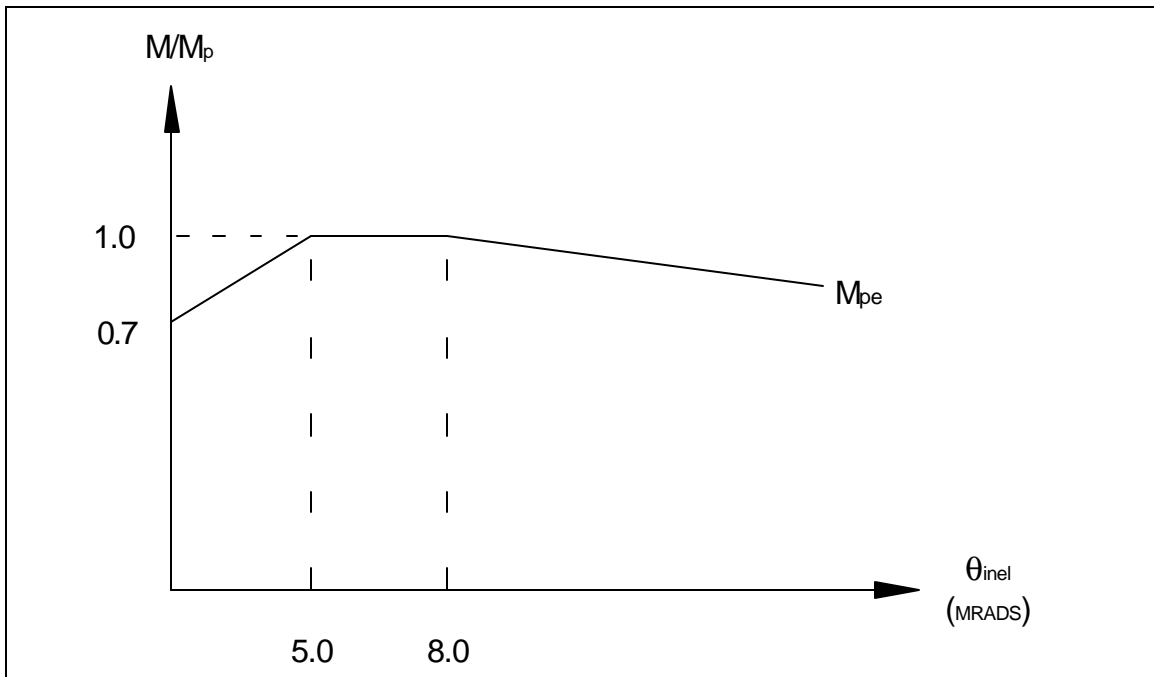


Figure 2.1.2.1 AASHTO 6.10.10.2.4d

where:

θ_{inel} = total inelastic rotation = sum of end inelastic rotations, $\theta_{inel-left}$ and $\theta_{inel-right}$

M_p = plastic moment,

M_{pe} = effective plastic moment (a common value of plastic rotation, θ_p , where M_{pe} occurs is $\theta_p = 0.063$ radian (Schilling and Morcos 1988)), and from AASHTO 6.10.10.1.2d, Strength limit state (AASHTO 1998, and interims through 2001),

$M_{pe} = R_f M_{pf} + R_w M_{pw}$ to account for local buckling during plastic rotation,

M_{pf} = flange plastic moment capacity component,

M_{pw} = web plastic moment capacity component,

$$R_f = \text{flange local buckling reduction factor} = \frac{0.0845E(2t_f / b_f)^2}{F_{yf}} \leq 1.0 ,$$

$$R_w = \text{web local buckling reduction factor} = \frac{1.32E(t_w / D_{cp})^2}{F_{yw}} \leq 1.0 ,$$

E = modulus of elasticity of steel,

t_f = flange thickness,

b_f = flange width,

F_{yf} = nominal yield stress of steel in flange,

t_w = web thickness,

D_{cp} = depth of web in compression, taken at the plastic moment, and

F_{yw} = nominal yield stress of steel in web.

2.1.3 Typical Moment-Rotation of Simply Supported Steel Girder

In inelastic analysis, a member's ability to resist rotation is characterized by its moment-rotation relationship. Figure 2.1.3.1 presents a typical moment-rotation relationship for a simply supported steel girder. One common measure of the ductility of a girder is the rotation capacity, R, defined as:

$$R = \frac{\theta_u - \theta_p}{\theta_p}$$

where:

θ_p = the hypothetical total (or one end) rotation when M_p is reached, assuming the girder remains completely elastic up to M_p, and

θ_u = the total (or one end) rotation at which the moment capacity returns to M_p after exceeding M_p and deforming past θ_p.

The expected rotation capacity, R, is three for a compact girder (AISC LRFD specification, 2nd edition, page 6-39, footnote [c] (American Institute of Steel Construction, 1998)). However, for bridges it is now thought that the maximum rotation necessary for redistribution of moments is 30 mrad = 0.030 radian (Schilling 1986).

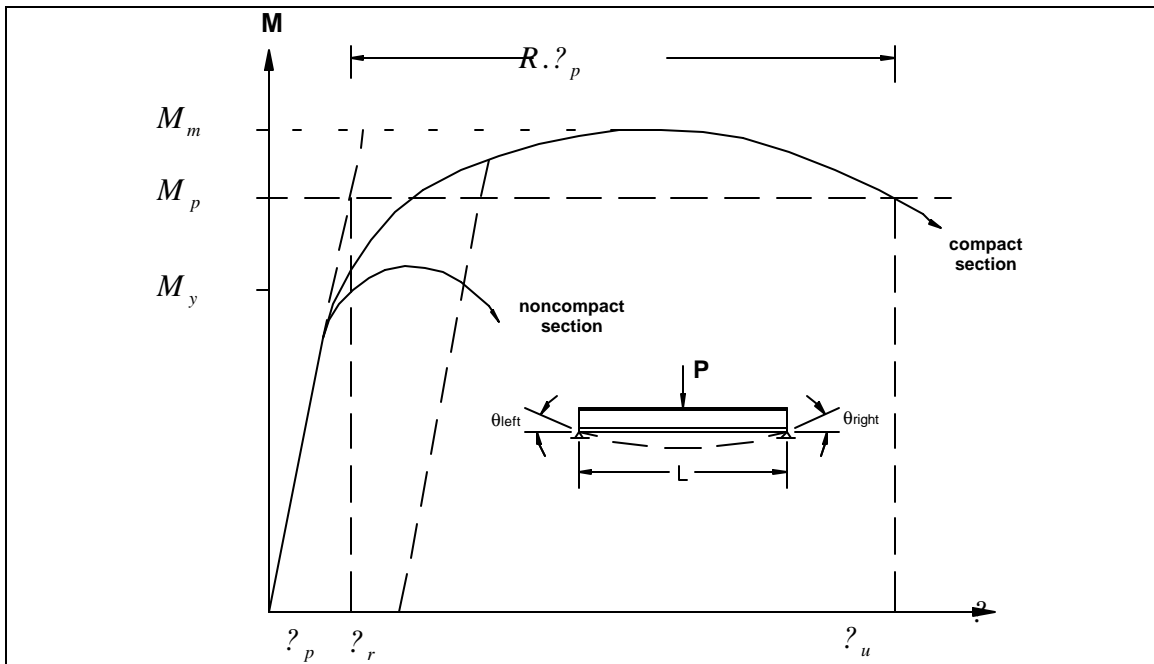


Figure 2.1.3.1 A Typical Moment-Rotation Curve for a Simple Span Girder with Adequate Lateral Bracing Provided

The moment-rotation behavior is affected by a number of factors. The spread of yielding throughout the cross section and along the length of the member, the initial pattern of residual stresses, and the girder proportions (ratio of the flange area to web area) mainly govern the shape of the ascending portion. The spacing of the compression flange bracing, the compression flange slenderness, the web slenderness, and initial imperfection (out-of-flatness) primarily affect the shape of the descending portion. Additionally, the behavior of a simply supported member under a distributed load is similar to that under a concentrated load, but the inelastic rotation is spread over a longer yield region (Hartnagel, 1997).

As the loading increases in Figure 2.1.3.1, yielding starts below the yield moment, M_y , due to initial residual stresses. Plastic rotation caused by this yielding thus adds to the theoretical elastic rotation to produce a total actual rotation. As the loading continues to increase, the moment M approaches a maximum value, M_m , which may be larger or smaller than the plastic moment, M_p . For compact sections, M_m typically exceeds M_p because of strain hardening, and the moment-rotation curve remains above M_p over a significant range of rotation. For noncompact sections, M_m usually remains below M_p throughout the loading and may or may not reach M_y .

Additionally, the slope of the descending portion of the curve depends on not only the spacing of lateral supports for the compression flange but also the slenderness of the flange and the web. Compact and noncompact width-to-thickness ratios of the flange and the web are limited to prevent local buckling before the material reaches its yield strength. While local buckling is causing major distortions of the cross section and/or lateral buckling is causing large permanent lateral deflections, the descending curve continues indefinitely (Hartnagel, 1997).

2.1.4 Correlation Between the Pier Moment Region and a Simple-Span Specimen

Figure 2.1.4.1 illustrates the correlation between the negative moment region near a pier in a continuous span girder and a simple-span experimental specimen loaded in negative bending by a concentrated load at midspan, in which the midspan load simulates the pier reaction and the simple supports simulate the adjacent inflection points. For the simply supported span, the total girder rotation, composed of elastic and inelastic components, is equal to the sum of the end rotations, θ_{left} , and θ_{right} . For a prismatic member, the theoretical total elastic rotation, θ_e , is equal to:

$$\theta_e = \frac{ML}{2EI} = \frac{PL^2}{8EI}$$

where:

P = midspan load,

M = midspan moment of simply supported span, $M = \frac{PL}{4}$,

L = span length,

I = moment of inertia, and

E = modulus of elasticity.

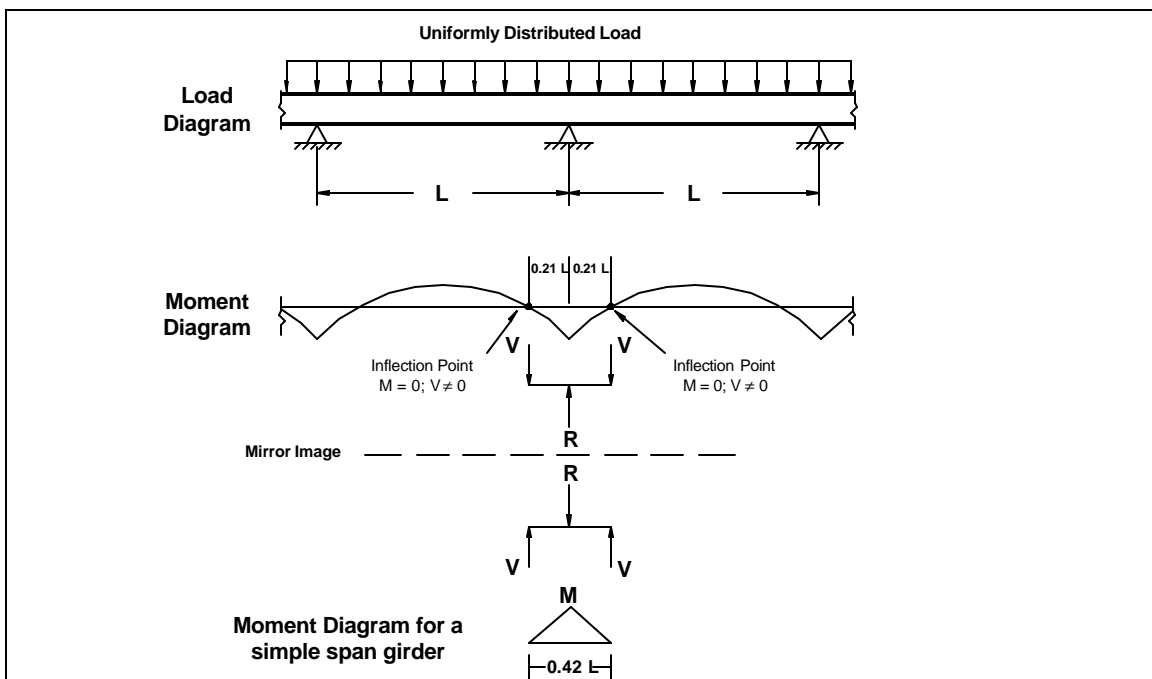


Figure 2.1.4.1 Correlation Between the Negative Moment Region Near a Pier in a Continuous Span Girder and the Experimental Test Girder

While elastic rotation occurs over the entire length of the simply supported span, inelastic rotation intensively appears in a finite yield region at midspan and is calculated by subtracting the calculated elastic portion from the measured total rotation. Since the unloading portion follows a path with the same slope as the elastic loading portion, the plastic rotation caused by a given load is equal to the permanent rotation that remains after the load has fully been removed (see Figure 2.1.3.1). No additional plastic rotation occurs as long as no higher load is applied again.

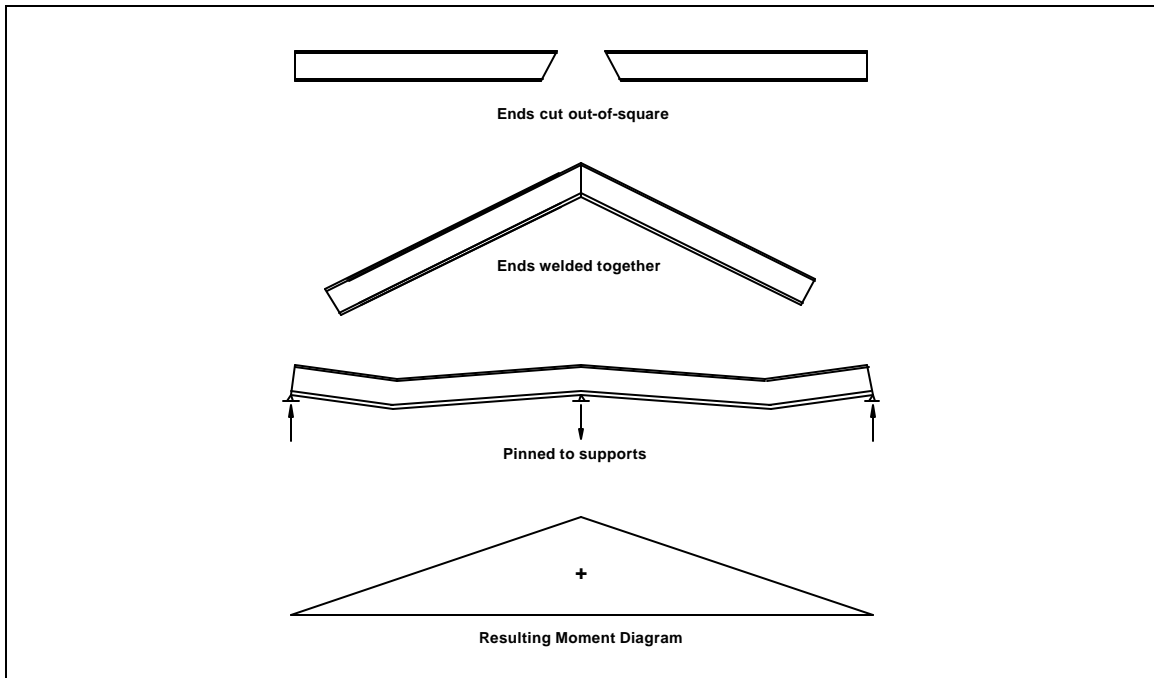


Figure 2.1.4.2 Plastic Rotation Analogy

Moreover, although inelastic rotation actually occurs within a finite yield length, it is usually assumed to occur at a single cross section (infinitesimal length) for calculation simplicity in inelastic analysis and design procedures. Hence, the simply supported member is assumed to respond elastically over its entire length and plastically at a single, angular discontinuity (see Figure 2.1.4.2). The angular discontinuity is equivalent to cutting the member into two halves slightly off-square (more cut off in tensile yielding zone) and then welding the cut ends together. Thus, the inelastic rotation from yielding has the same effect on subsequent structural behavior as an angular discontinuity that can be built in to the member (Hartnagel, 1997). The resulting positive moment at the interior support region, which only occurs when the member is held down on the pier (usually by dead load), is useful in bridge design, since it reduces the overstressed negative moments and slightly increases the positive under-stressed composite moment regions.

2.2 Large-Scale HPS70W Girder Tests

To achieve the pier moment-rotation behavior of high performance steel HPS70W I-shape girders, a program of both experimental and numerical works was conducted. For the experimental works, large-scale laboratory simple-span testing was first performed. The testing consisted of four experiments of noncomposite compact/noncompact sections of HPS70W I-shape girders fabricated by Zimmerman Metals, Inc., Denver, Colorado. The test girder dimensions were constrained by the actuator loading capacity, about 200 kips, available at Colorado State University (CSU), and plate thickness sizes donated from Bethlehem Lukens Plate, a division of Bethlehem Steel Corporation, Burns Harbor, Indiana.

Second, experimental examination of the stress-strain relationships for HPS70W is necessary for the material inputs of numerical analyses. The laboratory experiments will follow ASTM E-8, Standard Tests Methods for Tension Testing of Metallic Materials, published by the American Society for Testing and Materials (ASTM).

2.2.1 Compact/Noncompact Girder Dimensions

Table 2.2.1.1 CSU Compact Girder Dimensions		
Property	Specimen #1 (nominal compact)	Specimen #2 (nominal compact)
Test span, L (ft)	19.5	22
Web depth inside flanges, D (in.)	16	19
Web thickness, t_w (in.)	1/4	1/4
Compression flange width, b_{fc} (in.)	9	9
Tension flange width, b_{ft} (in.)	10	9
Flange thickness, t_f (in.)	3/4	3/4
Ratio of web depth in compression, D_{cp}/D , nominal [avg. of tested values]	0.594 [0.612]	0.5 [0.5]
Nominal flange slenderness, $b_f/2t_f$	6.0	6.0
Web slenderness, $2D_{cp}/t_w$, nominal [avg.]	76.0 [78.3]	76.0 [76.0]
a_r , nominal [average of tested values]	0.352 [0.363]	0.352 [0.352]

Table 2.2.1.2 CSU Noncompact Girder Dimensions		
Property	Specimen #3 (noncompact)	Specimen #4 (noncompact)
Test span, L (ft)	27.5	31.5
Web depth inside flanges, D (in.)	21	25
Web thickness, t_w (in.)	1/4	1/4
Compression flange width, b_{fc} (in.)	10	11
Tension flange width, b_{ft} (in.)	11	11
Flange thickness, t_f (in.)	3/4	3/4
Ratio of web depth in compression, D_{cp}/D , nominal [avg. of tested values]	0.571 [0.585]	0.5 [0.5]
Nominal flange slenderness, $b_f/2t_f$	6.67	7.33
Web slenderness, $2D_{cp}/t_w$, nominal [avg.]	96.0 [98.3]	100.0 [100.0]
a_r , nominal [average of tested values]	0.400 [0.410]	0.379 [0.379]

where:

D_{cp} = depth of web in compression, taken at the plastic moment (in.), and

a_r = ratio of web compression area to flange compression area, taken at the plastic moment.

In proportion to AASHTO specifications (AASHTO, 1998 and interims through 2001), Table 2.2.1.1 presents the dimensions of the two “nominal” compact girders, Specimens #1 and #2 (see Section 3.2.3 for “nominal/actual” considerations). Specimen #1 (span of 19.5 ft) had a larger lower flange, which lowered the elastic neutral axis to put more girder web into compression ($D_{cp}/D = 0.6$). This was to account for the concrete deck and rebars near interior supports in composite girders. However, Specimen #2 was a symmetric I-girder ($D_{cp}/D = 0.5$) with larger cross-section and span of 22 ft.

In Tables 2.2.1.1 and 2.2.1.2, the nominal or [average of tested values] values are based on the nominal yielding strength, $F_{yf} = F_{yw} = 70.0$ ksi for all the flanges and web, or the average material tested data, $F_{yf} = 83.35$ ksi for the flanges and $F_{yw} = 69.83$ ksi for the web, respectively. Table 2.2.1.2 displays the dimensions of the two noncompact girders. In proportion to AASHTO specifications, Specimens #3 and #4 were designed with compact flanges and a noncompact web. Specimen #3 (span of 27.5 ft) had a larger lower flange, which lowered the elastic neutral axis to put more girder web into compression ($D_{cp}/D = 0.6$), to account for the concrete deck and rebars near interior supports in composite girders. On the other hand, Specimen #4 was a symmetric I-girder ($D_{cp}/D = 0.5$) with larger cross-section and span of 31.5 ft.

2.2.2 Testing Apparatus Design and Overhaul

The four non-composite girders were tested in the conventional simply supported configuration. The overhaul and strengthening of a pre-existing test apparatus consisted of joining and reinforcing two separate load frames, each supporting a 100-kip capacity actuator for sufficiently applying a midspan, concentrated force and establishing the lateral bracing system, whose unbraced length are specified by AASHTO 6.10.4.1.7 (AASHTO, 1998 and interims through 2001). In addition, a linear variable displacement transducer (LVDT) was connected to each actuator to allow displacement-control actuator movement that ultimately permitted a thorough, careful examination of post-peak behavior. Figure 2.2.1.1 shows a photograph of the CSU overall final testing apparatus. Predominately a testing facility for timber structures, testing steel at CSU Structural Engineering Lab initially required the overhaul and strengthening of a pre-existing test apparatus. Four components are utilized for the final design of the entire steel testing apparatus (see Table 2.2.2.1): (1) a stiffened distributor beam linking two 100-kip capacity actuators, (2) interchangeable column posts for adjustment of the loading level, (3) compression-flange lateral bracing system, and (4) girder reaction supports (Griffeth, 2001).



Figure 2.2.2.1 Overall Testing Apparatus at CSU Structural Engineering Lab

Table 2.2.2.1 CSU Testing Apparatus Summary	
Description and Specification	AISC Member Size
Distributor Beam. ASTM A572, Grade 50.	W10x68
Vertical Column Lateral Bracing and Support System. ASTM A572, Grade 50.	W8x40
Back-to-Back Angles for Lateral Bracing. ASTM A36, Grade 36.	L3x3x1/2
Various Length Column Posts. ASTM A500, Grade B.	6x6 structural tubing, 1/2" thick
Various Plate Sizes and Thickness. ASTM A36, Grade 36.	-----
High Strength Bolts. ASTM A325 (Type 1)	-----



Figure 2.2.2.2 LVDTs, Actuators, Distributor Beam, and the Load Frame Bracing

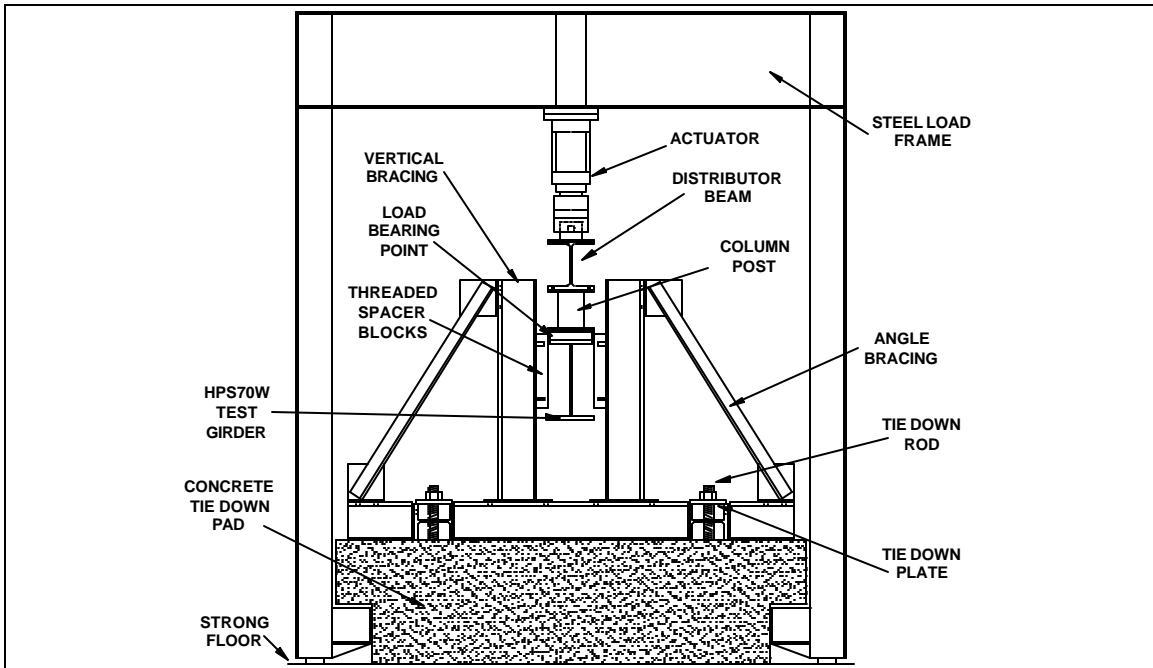
At first, a linear variable displacement transducer (LVDT) was mounted on an aluminum plate and connected to each actuator, allowing displacement-control actuator movement as opposed to load-control actuator movement (see Figure 2.2.2.2). This renovation ultimately permitted a thorough, careful examination of post-peak behavior.

Additionally, loading the test girders demands the use of two 100-kip capacity actuators in conjunction for sufficiently applying a midspan, concentrated force corresponding to the plastic moment capacity of the stiffest girder. As a result, two separate load frames, each supporting an actuator, were joined and

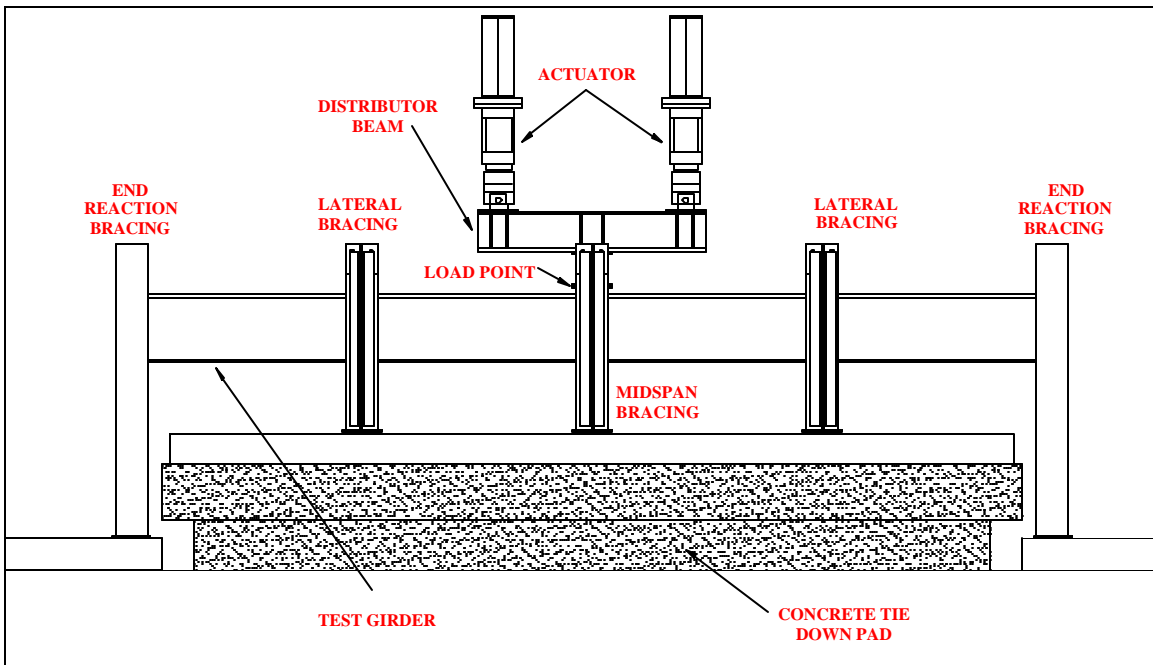
reinforced with eight bolted bracing angles. In addition, a stiffened distributor beam is employed to link the fixed-height actuators, which are spaced about 5 ft. apart. Furthermore, the actuator maximum vertical travel distance of 6 in. inherently requires manufacture of various length interchangeable column posts, which are added as needed to provide the vertical travel distance beyond 6 in., to ultimately examine the post-peak behavior of the girders. In detail, the column posts are bolted to the bottom of the distributor beam and comprised of 1/2 in. thick square structural tubing welded to end plates. For load bearing, a 3 in. diameter half-round is connected to the bottom end plate of the column post (see Figure 2.2.2.3). The CSU experimental testing facility resembles a universal testing machine. The girder reactions are resisted by the concrete floor (see Figures 2.2.2.4 and 2.2.2.5). The compressive actuator uplift force is counterbalanced by a system of two parallel connecting frames made of wide flange steel girders, which pull up against a massive 46-kip concrete pad bolted down to the strong floor. The length of the concrete tie down pad is shorter than the test girder lengths, so the reaction loads of the girder are directly on the strong floor.



Figure 2.2.2.3 Load Bearing Point



**Figure 2.2.2.4 Testing Apparatus and Bracing Cross-View Configuration
(Beam reaction supports omitted for clarity)**



**Figure 2.2.2.5 Testing Apparatus and Girder Bracing Longitudinal Configuration
(Load frame columns omitted for clarity)**

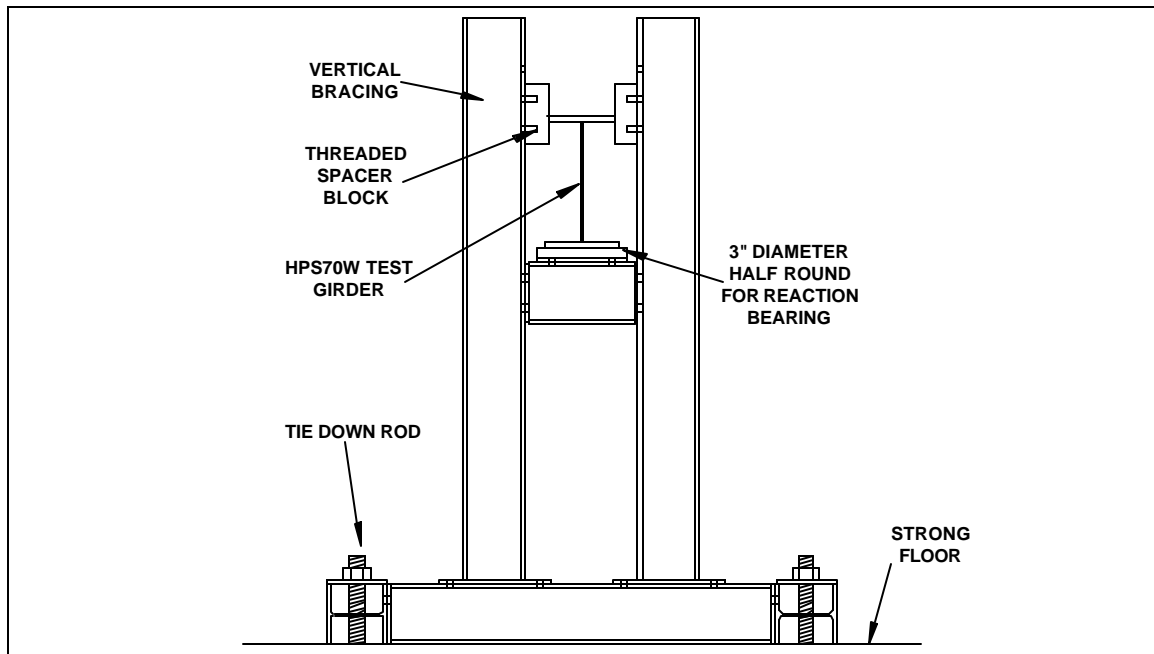


Figure 2.2.2.6 Reaction Bracing and Supports

Moreover, slip-critical bolted connections are provided for both lateral bracing and reaction supports. These types of connections prevent movement or slip, which would have an unfavorable effect on the test results, and also promise a changeable test setup to be compatible with a broad range of possible future experiments. In addition, the lateral bracing, whose unbraced length are specified by AASHTO 6.10.4.1.7 (see Section 2.1.1), consists of vertical, wide flange columns top-braced by double angles, and thin threaded spacer blocks were greased and bolted to the vertical columns to allow for smooth vertical movement of the test specimen within the bracing (see Figure 2.2.2.4). The height of the reaction supports must assure enough clearance to allow for sufficient midspan deflection and rotation of the deepest test girder (see Figure 2.2.2.6). Finally, the member sizes of the vertical column bracing and the lateral bracing were determined based on the maximum lateral force located at midspan, which was conservatively anticipated to be 10% of the compression flange force. The entire system was modeled in the SAP2000 structural analysis computer program, in which case it exhibited minimal, acceptable displacements and deformations.

2.2.3 Specimen Instrumentation and Measurement

For the laboratory testing of the four non-composite HPS70W girders, electrical instrumentation employed were: (1) master-slave MTS 407 controllers with linear variable displacement transducers (LVDTs) to operate hydraulic actuators in a displacement-control manner, (2) load cells in actuators to measure loads, (3) string-potentiometers attached to the underside of the girders to obtain deflections directly and rotations indirectly, and (4) quarter-bridge-configuration strain gages (completed bridge inside the Hewlett Packard (HP) Data Acquisition and Control Unit) to measure strains. For the two noncompact girders, a deflection dial gage was also employed to measure midspan deflection of the bottom flange.

A data acquisition system, which consists of HP 3852A Data Acquisition and Control Unit operated by LabVIEW 5.0 installed on a personal computer, reads electronic signals from the LVDTs, load cells, strain gages, and string-potentiometers (string-pots) through electronic channels. For each channel, the data acquisition system receives 20 data points per reading and averages them to obtain one value per

reading. In addition, the total applied midspan load was determined as the summation of actuator load cell forces, which were obtained from electronic readings through MTS 407 controllers (a master and a slave) connected to the data acquisition system. Since load cells were not located at the two end reactions, the support reactions are assumed to be each equal to one half of the applied load.

Figures 2.2.3.1, 2.2.3.2, 2.2.3.3, and 2.2.3.4 present the instrumentation locations of Specimen #1, #2, #3, and #4, respectively. At midspan, ten strain gages on each girder measured longitudinal strains at two cross sections, five gages each respectively 8 in. north and south of midspan. The strain gages were calibrated at $1000 \mu\epsilon$ strain with a shunt resistor. In addition, string-pots were attached to the underside of each girder to directly measure the vertical deflections at midspan. For the two noncompact girders, Specimens #3 and #4, a deflection dial gage was also employed to measure midspan deflection of the bottom flange (see Figure 2.2.3.5). For the two compact girders, Specimens #1 and #2, two additional string-pots were attached to an aluminum cantilever bar glued to the web at north and south near midspan to check the very small point rotations around the neutral axis (see Figure 2.2.3.6).

At the support regions, four to eight additional string-pots, spaced at known distances, were attached to the under and/or top side of each girder to indirectly obtain two near-end rotations that were averaged over 12 in. (see Figure 2.2.3.5). One or two string-pots were also attached to the underside of each girder to directly measure the vertical deflection(s) at intermediate point(s) in span.

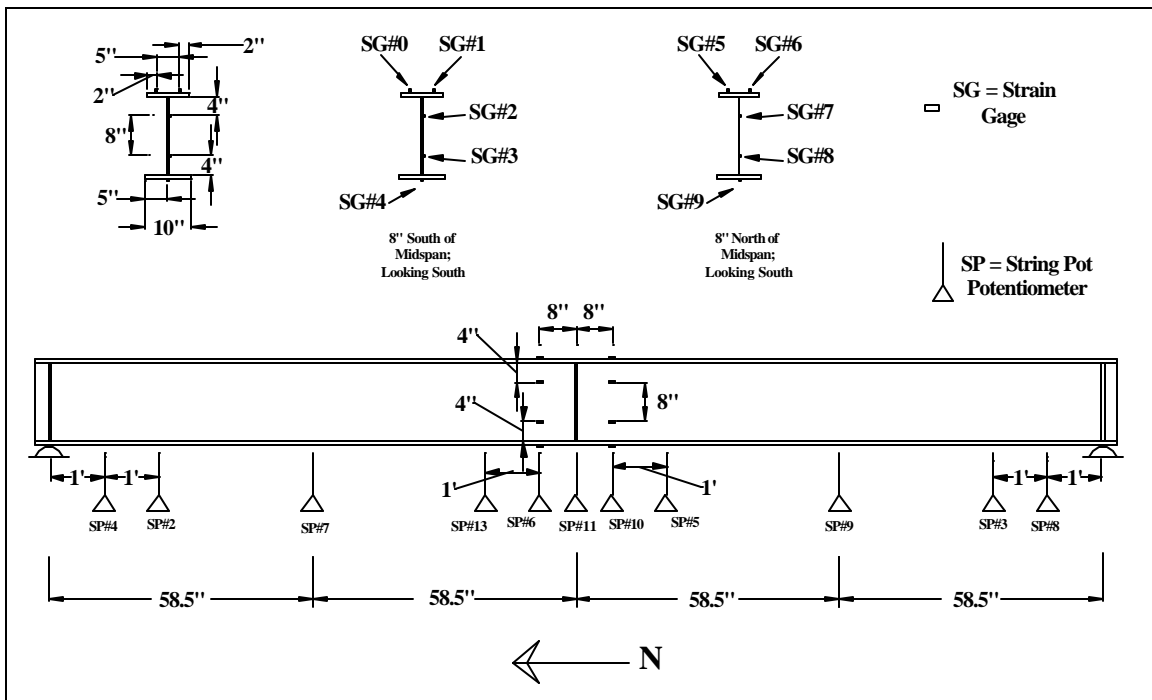


Figure 2.2.3.1 Specimen #1 - Instrumentation Locations

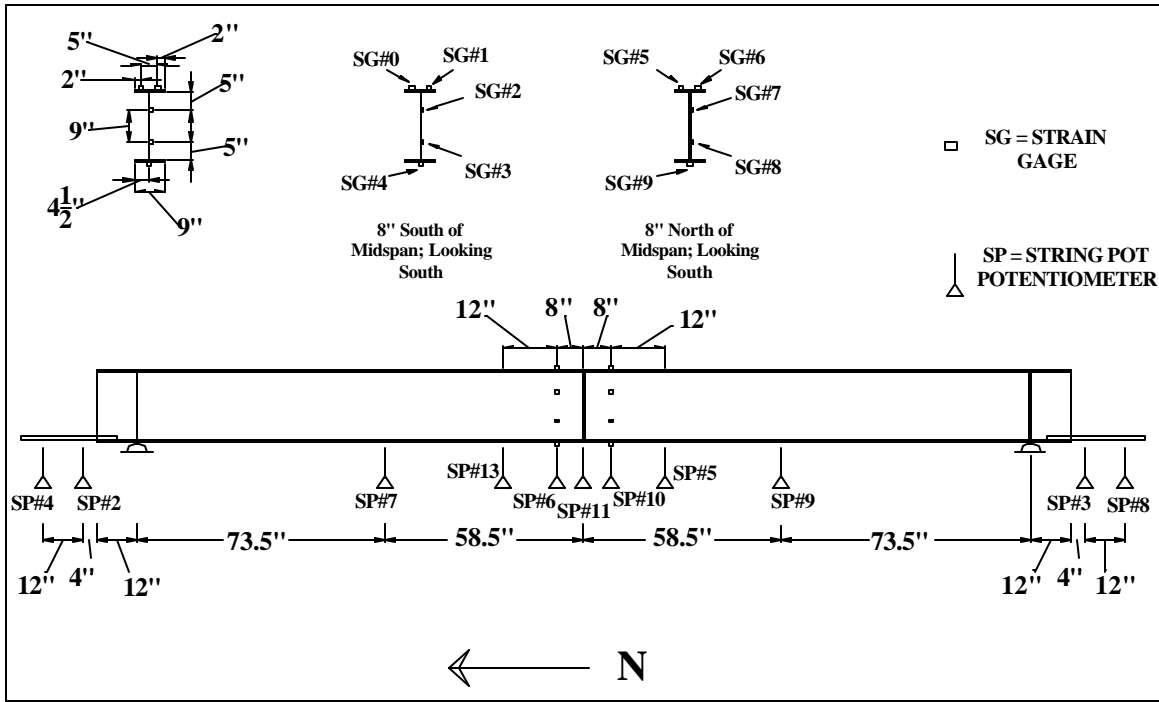


Figure 2.2.3.2 Specimen #2 - Instrumentation Locations

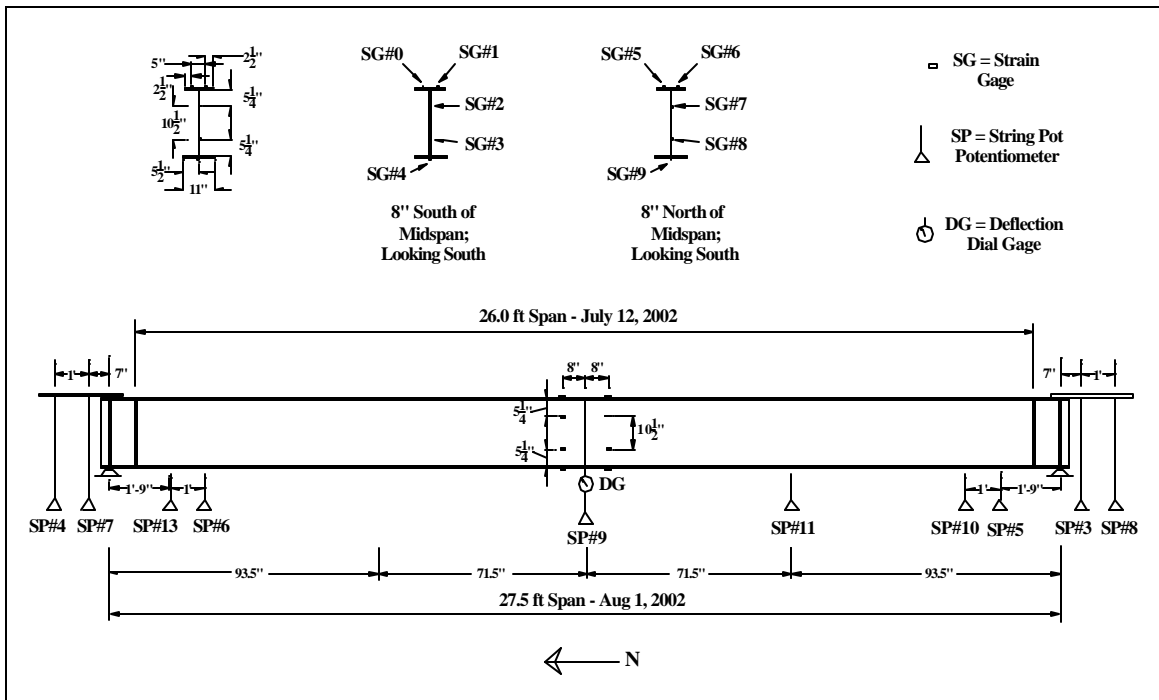


Figure 2.2.3.3 Specimen #3 - Instrumentation Locations

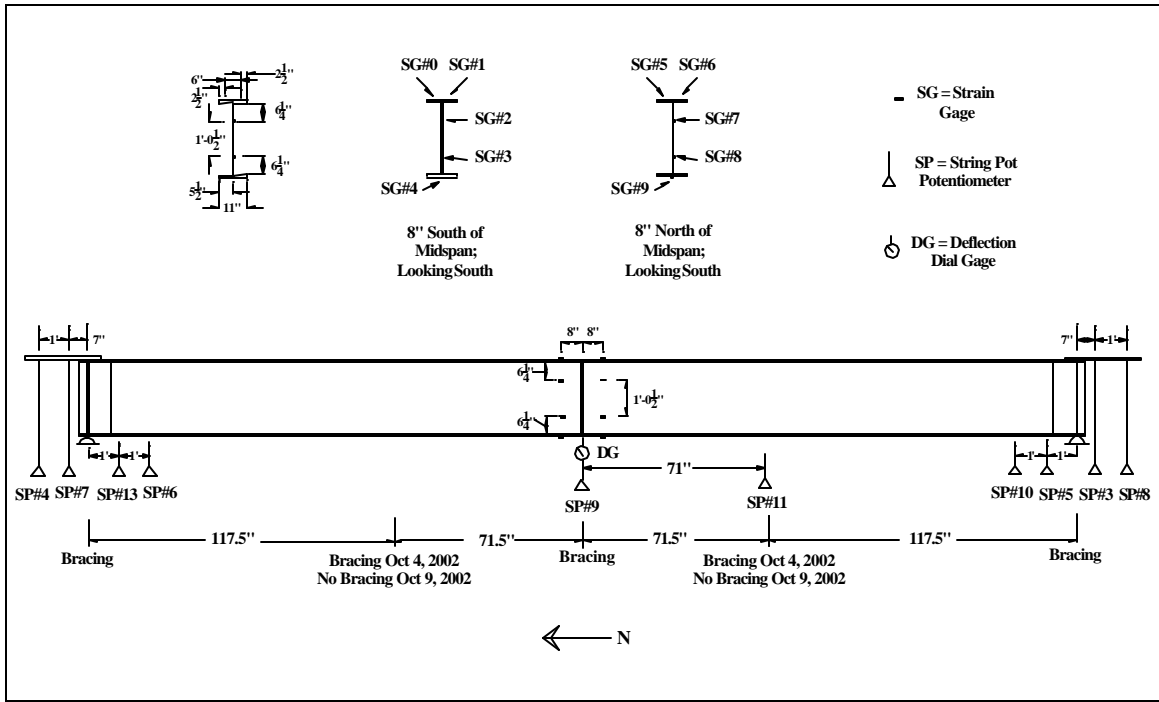


Figure 2.2.3.4 Specimen #4 - Instrumentation Locations

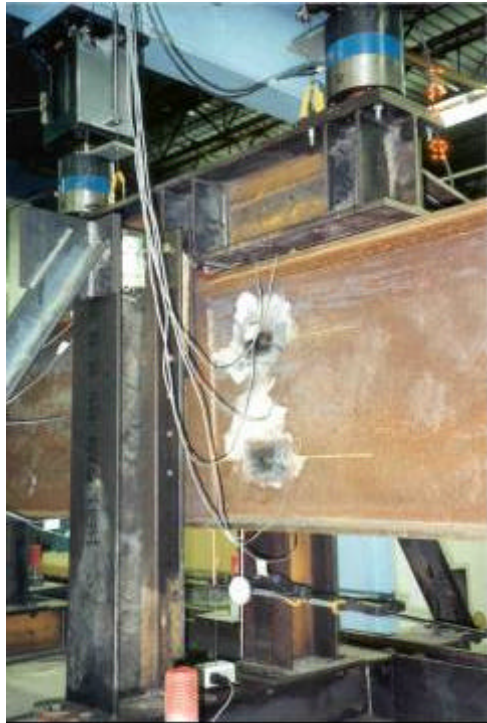


Figure 2.2.3.5 Left: Midspan Arrangement for Specimens #3 and #4
Right: Typical End Rotation Measurement Instrumentation



Figure 2.2.3.6 Midspan Arrangement for Specimens #1 and #2

2.2.4 Test Procedures

Under displacement control, the girders were tested in a simply supported configuration and deflected vertically downward. First, the test for Specimen #1 was performed on February 1, 2001. Specimen #1 was deflected vertically downward to 1.85 in. at a rate of 4 in./hr., and the load was removed at the same displacement rate. Each time the testing was paused at various displacement and load intervals the computer data acquisition system acquired LVDT, load cell, strain gage, and string-pot readings. Then, the load was totally removed. A new displacement rate of 8 in./hr. was applied until the specimen was deflected vertically downward 4.38 in. During this period, incremental data readings were taken, and the load was again removed at 8 in./hr. At this time, after the load was totally removed, a longer column post was installed, since the girder's permanent midspan vertical displacement was approximately 2.2 in. Thereafter, at a reloading rate of 10 in./hr., a maximum load of 196.5 kips (maximum moment of 957.9 ft-kips) was reached at a midspan deflection of 4.44 in. ("total rotation" of 0.0899 rad measured near the supports as shown in Figure 2.2.3.1). When a significant change in load resistance and large scale local deformations were observed, at which Specimen #1 was deflected downward totally 7.04 in. ("total rotation" of 0.1332 rad) corresponding to a total load of 170 kips (moment of 828.9 ft-kips), the load was removed. Finally, Specimen #1 bounced back due to the elastic recovery to a permanent midspan deflection of 5.24 in. ("total rotation" of 0.0937 rad at near supports) corresponding to zero load and moment. There were 119 total readings for Specimen #1.

Second, Specimen #2 was tested on February 15, 2001. It was deflected vertically downward to 2.11 in. at a rate of 3 in./hr., and then the load was totally removed at 6 in./hr. During this period, the testing was halted at various displacement and load intervals for the computer data acquisition system to acquire LVDT, load cell, strain gage, and string-pot readings. Then, the reloading progressed at a new displacement rate of 6 in./hr. A maximum load of 203.9 kips (maximum moment of 1121.6 ft-kips) was

reached at a midspan downward deflection of 3.60 in. (“total rotation” of 0.0594 rad measured near the supports as shown in Figure 2.2.3.2). When the specimen was deflected vertically downward 4.93 in., the load was removed at 10 in./hr. As before, periodic data readings were taken. After the load was totally removed this time, a longer column post was utilized, since the girder’s permanent midspan vertical deflection was approximately 2.82 in. Thereafter, a reloading rate of 10 in./hr. was applied. When a significant change in load resistance and large scale local deformations were observed, at which Specimen #2 was deflected downward totally 6.81 in. (“total rotation” of 0.1076 rad) corresponding to a total load of 155.2 kips (moment of 853.5 ft-kips), the load was removed. Finally, Specimen #2 bounced back to a permanent midspan deflection of about 4.94 in. (“total rotation” of 0.0593 rad at near supports) corresponding to zero load and moment. There were 145 total readings for Specimen #2.

Third, test for Specimen #3 was first performed on July 12, 2001 with its original span of 26.0 ft (see Figure 2.2.3.3). Initially, Specimen #3 was deflected vertically downward to 0.846 in. at a rate of 4 in./hr., and then the load was removed at 4 in./hr. Again, the testing was halted at various displacement and load intervals for taking periodic data. After the load was totally removed, the displacement rate was increased to 6 in./hr. for reloading. With yielding on the compression flange and web in compression (strain gages #0, #1, #2, #5, and #6) at a total load of 192.4 kips (moment of 1250.9 ft-kips), the specimen was deflected vertically downward 2.545 in. (“total rotation” of 0.0411 rad measured inside and near the supports). The total load then reached and was maintained exceeding the nominally available load capacity of 200 kips. Suddenly, the hydraulic pump shut down because of over-temperature when the total load was about 209.1 kips (moment of 1359.2 ft-kips). From a vertical deflection of 2.904 in. (“total rotation” of 0.0465 rad) at this stage, the specimen bounced back to a deflection of 0.428 in. (“total rotation” of 0.0054 rad) at a corresponding load of 3.5 kips (moment of 22.6 ft-kips) due to elastic recovery. Afterward, the reloading was continued for a rate of 10 in./hr. As before, periodic data readings were taken until hydraulic pump shut down again because of over-temperature at a total load of 215.2 kips (moment of 1398.8 ft-kips) corresponding to a vertical deflection of 3.131 in. (“total rotation” of 0.0508 rad). From that stage, the specimen bounced back to a permanent deflection of 0.507 in. (permanent “total rotation” of 0.0057 rad) at zero load and moment. There were 111 total readings for Specimen #3 on the July 12-test.

Thereafter, the span of Specimen #3 was increased to 27.5 ft in order to have a larger available moment with the same available load. Test for Specimen #3 was continued with the longer span on August 1, 2001 (see Figure 2.2.3.3) at a rate of 10 in./hr. North-web buckled to West at a total load of 208.5 kips (moment of 1433.4 ft-kips). At a maximum total load of 208.6 kips (moment of 1434.4 ft-kips) in the yielding plateau stage, Specimen #3 was deflected vertically 3.609 in. beyond the permanent deflection of 0.507 in. After the load was totally removed at 10 in./hr., a longer column post was utilized as the girder’s permanent midspan vertical deflection totally increased to 1.00 in. Then, at a reloading rate of 20 in./hr. until a significant flange buckle was noticed at a maximum load of 209.8 kips (moment of 1442.4 ft-kips), Specimen #3 was deflected downward totally 4.07 in. (“total rotation” of 0.0619 rad). When the distributor beam connecting the two actuators was considerably uneven, the load was removed for safety. At that unloading starting point, Specimen #3 was deflected downward totally 4.56 in. (“total rotation” of 0.0623 rad) corresponding to a total load of 202.9 kips (moment of 1395.2 ft-kips). Finally, Specimen #3 bounced back to a final permanent midspan deflection of 1.58 in. (“total rotation” of 0.0215 rad inside and near supports) corresponding to an approximate zero load and moment. There were 60 total readings for Specimen #3 on the August 1-test.

Fourth, Specimen #4 was experimentally tested with two variations of lateral compression-flange bracing. Test on Specimen #4 was first performed on October 4, 2001 with bracing at midspan load point, end reactions, and in between middle and end satisfying AASHTO specifications (AASHTO, 1998 and interims through 2001) for both compact and noncompact section (see Figure 2.2.3.4 and calculations in Section 3.2.4). At a loading rate of 6 in./hr. and unloading rate of 10 in./hr., the testing was halted at

various displacement and load intervals for taking periodic data. With yielding on the compression flange at a total load of 204.6 kips (moment of 1610.8 ft-kips), the specimen was deflected downward 3.14 in. (“total rotation” of 0.0438 rad measured inside and near the supports). The midspan deflection then increased to 3.40 in. (“total rotation” of 0.0465 rad) at a maximum load of 215.2 kips (moment of 1694.8 ft-kips). The specimen was unloaded when the midspan deflection was 3.41 in. (“total rotation” of 0.0466 rad) at a total load of 214.9 kips (moment of 1692.7 ft-kips). When the load was totally removed, the permanent midspan deflection was 0.39 in. corresponding to a permanent “total rotation” of 0.0045 rad. There were 39 total readings for Specimen #4 on the October 4 test.

Finally, test on Specimen #4 was continued on October 9, 2001, with bracing only at midspan and at supports, for which the unbraced length dissatisfied AASHTO specifications (see Figure 2.2.3.4 and calculations in Section 3.2.4). A loading rate of 6 in./hr. and unloading rate of 10 in./hr. were applied. At a total load of 164.2 kips (moment of 1292.7 ft-kips), the specimen’s North side displaced to West slightly. At a maximum load of 215.9 kips (moment of 1700.2 ft-kips), the midspan deflection increased to 3.08 in. beyond the permanent deflection of 0.39 in. (“total rotation” of 0.0433 rad in addition to the permanent “total rotation” of 0.0045 rad). The specimen was unloaded when the midspan deflection totally reached 3.51 in. (“total rotation” of 0.0479 rad) at a total load of 215.2 kips (moment of 1694.5 ft-kips). When the load was totally removed, the final permanent midspan deflection was 0.46 in. (final permanent “total rotation” of 0.0048 rad inside and near supports). There were 37 total readings for Specimen #4 on the October 9 test.

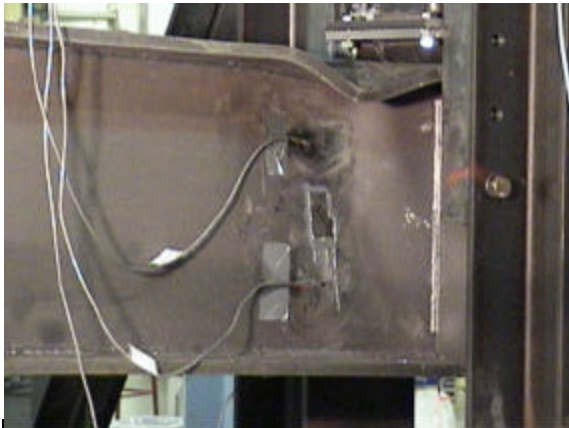
Results of the large-scale laboratory testing for the four noncomposite HPS70W specimens are presented with plots of moment-rotation relationships in Section 4.2. In addition, Figures 2.2.4.1 and 2.2.4.2 below present the states of midspan deformed shapes and final deformed shapes of Specimen #1, respectively. Figure 2.2.4.3 displays final deformed shapes of Specimen #2 while Figure 2.2.4.4 show the midspan deformed shape of Specimen #3 and a photo of Specimen #4 after its October 4 test.



Local web buckle. This is just below the local flange buckle that is depicted in each of the other three photos.



Beginning of a local flange buckle .



This is the same flange and web local buckle at an advanced state.



This is the beam after unloading. Note that the loading half round is lifted off the beam. The beam was simply supported and loaded in the middle.

Figure 2.2.4.1 States of Midspan Deformed Shape of Specimen #1 (February 1, 2001)



Figure 2.2.4.2 Final Deformed Shapes of Specimen #1 (February 1, 2001)

**Above: Local web and flange buckle at midspan
Below: Lateral torsional buckle of compression flange**



Figure 2.2.4.4 Above: Midspan Deformed Shape of Specimen #3 (August 1, 2001)
Below: Specimen #4 after first tested (October 4, 2001)

2.2.5 Experimental Study of Bracing Lengths for Specimen #4

The effects of lateral bracing lengths on moment-rotation behavior of Specimen #4, a noncompact girder, were studied from the response of the specimen with lateral compression-flange bracing classified as either satisfying or dissatisfying the AASHTO requirements (AASHTO, 1998 and interims through 2001) categories. In three-point loading, the midspan (at the load point) is the most critical region of a girder for lateral torsional buckling. As a result, lateral bracing is first assigned at the midspan of the test girders, and the compression flange bracing from the load point to the next compression flange brace is checked against the maximum unbraced length permitted by AASHTO. Specimen #4 was experimentally tested with two variations of lateral compression-flange bracing (see Sections 2.1.1 and 3.2.4):

- (1) bracing at midspan, 71.5 in. North and South from midspan (unbraced length, L_b , satisfies AASHTO specifications (AASHTO, 1998 and interims through 2001) for compact section (at 98 in) and noncompact section (at 107.1 in)), and at supports, and
- (2) bracing only at midspan and at supports (L_b does not satisfy AASHTO specifications).

The corresponding numerical model of Specimen #4 was analyzed with two bracing configurations as experiments. The effects of the various unbraced lengths on the inelastic moment-rotation relationship for Specimen #4 resulted from the two numerical models satisfying or dissatisfying the AASHTO specifications of lateral compression-flange bracing are presented in Section 4.3.

2.3 Experimental Examining the Stress-Strain Relationship for HPS70W

2.3.1 Tensile Tests on Flange and Web Samples of HPS70W

Experimental examination of the stress-strain relationships for HPS70W is necessary for the material inputs of numerical analyses. Beside the inputs of residual stresses and imperfection, a few parametrical variations in the material stress-strain relationship can result in changes in pier moment-rotation response of the numerical models of HPS70W I-shape girders. In previous studies, different authors used different typical options of proper material inputs for numerical models of HPS70W girders (Barth and White 1998; White, Barth, and Bobb 1998; Zubeck 2000). In addition, there were various values for the modulus of elasticity of the flange steel and web steel, E_{flange} and E_{web} , in Appendices B1 and B2 of the Yakel, Mans, and Azizinamini's (1999) report.

Hence, to decide proper material inputs for numerical models of HPS70W girders at CSU, tensile tests on a number of flange and web samples were performed to determine the values of the modulus of elasticity, E , and the stress-strain relationships of HPS70W. The photos of the samples, parallel and perpendicular to the rolling direction, for the uniaxial tensile tests are displayed in Figures 2.3.1.1, 2.3.1.2, 2.3.1.3, and 2.3.1.4. The laboratory experiments followed ASTM E-8, Standard Tests Methods for Tension Testing of Metallic Materials, published by the American Society for Testing and Materials (ASTM). The results of

the uniaxial tensile tests for flange and web samples as material inputs for numerical models are presented in Section 3.2.2.



Figure 2.3.1.1 Flange Samples of HPS70W for Uniaxial Tensile Tests - Parallel to Rolling Direction



Figure 2.3.1.2 Flange Samples of HPS70W for Uniaxial Tensile Tests - Perpendicular to Rolling Direction



Figure 2.3.1.3 Web samples of HPS70W for Uniaxial Tensile Tests - Parallel to Rolling Direction



Figure 2.3.1.4 Web Samples of HPS70W for Uniaxial Tensile Tests - Perpendicular to Rolling Direction

2.3.2 Material Tested Data of HPS70W Plates: A Query for
 “Nominal Compact”
 Classification and Calculation for Plastic Moments

HPS70W Specimens #1 and Specimen #2 at Colorado State University (CSU) were classified as compact girders, nominally. The classification at CSU was based on the two compact section requirements AASHTO 6.10.4.1.2 and AASHTO 6.10.4.1.3 for web and flange, respectively (AASHTO, 1998 and interims through 2001). Particularly for the web, the limit value of $\frac{2D_{cp}}{t_w} \leq 3.76 \sqrt{\frac{E}{F_{yc}}}$, as 76.5 for CSU,

was calculated by substituting the conventional modulus of elasticity of steel, $E = 29,000$ ksi, and the specified minimum yield strength of the compression flange, $F_{yc} = 70$ ksi for HPS70W, nominally.

However, the limit value, $3.76 \sqrt{\frac{E}{F_{yc}}}$, becomes 71.5 when substituting $F_{yc} = 83.35$ ksi and $E = 30,113$

ksi, averaged from material tested data. At this stage, the web slenderness ratio, $\frac{2D_{cp}}{t_w}$, as 76.0, nominally [or 78.3, actually], for Specimen #1 and 76.0 for Specimen #2, is greater the limit value of 71.5. As a result, both HPS70W “nominal” compact girders at CSU would be questioned to be classified as noncompact.

Tables 2.2.1.1 and 2.2.1.2 (see Section 2.2.1) present the dimensions of CSU’s HPS70W girders, Specimens #1 to #4. Based on the dimensions and the nominal yielding strength, $F_{yf} = F_{yw} = 70.0$ ksi for all the flanges and web, or the average material tested data, $F_{yf} = 83.35$ ksi for the flanges and $F_{yw} = 69.83$ ksi for the web, the plastic moments, M_p , for Specimens #1, #2, #3, and #4 are calculated in the Appendix (see Appendix A.1).

3. NUMERICAL MODELS FOR HPS70W I-GIRDERS

3.1 Introduction

In general, the physical attributes and behavior phenomena affecting the strength and stability of a structure are defined (Zubeck, 2000) below:

Geometric Nonlinearity

- P- Δ effect – effect of axial force acting through displacements associated with member chord rotation.
- P- δ effect – effect of axial force acting through displacements associated with member curvature.
- Wagner effect – effect of bending moment and axial forces acting through displacements associated with member twisting.
- Curvature shortening – effect of curvature on longitudinal displacements at member ends.
- Sway shorting – effect of large chord rotation on longitudinal displacements at member ends.
- Lateral torsional buckling.
- Local buckling and local distortion.
- Interaction of local and member instability.

Material Nonlinearity

- Strain hardening.
- Elastic unloading.
- Yielding – concentrated or spread yielding.
- Multi-dimensional plasticity effect.
- Influence of loading sequence on path dependent plasticity.
- Cyclic plasticity effect – Bauschinger, cyclic hardening, elastic shakedown.
- Strain-aging.

Physical Attributes

- Initial geometric imperfections – out-of-plumpness, out-of-straightness, cross-sectional distortion, and connection eccentricities.
- Initial residual stresses.
- Positive and negative member end restraint.
- Cross-section symmetry/nonsymmetry.
- Prismatic/nonprismatic member profile.
- Location of stiffeners and bracing.
- Composite interconnection with concrete slabs.

The finite element method of analysis cannot be extended to encompass all the aspects listed above, and not all of these aspects apply to bridges. However, the attributes of geometric nonlinearity, material nonlinearity, initial geometric imperfection, and initial residual stresses will be used in the numerical moment-rotation analysis following to compare with the experimental results in order to achieve the pier moment-rotation behavior of high performance steel HPS70W I-shape girders.

3.2 Numerical Moment-Rotation of Non-Composite HPS70W Girders

3.2.1 Implementation of ABAQUS Finite Element Code

The numerical moment-rotation analyses of HPS70W noncomposite girders at CSU are performed using ABAQUS finite element code with nonlinear solutions. ABAQUS buckling analysis, post-peak analysis procedures, modified Rik's method for load and displacement control, nonlinear option, and accounting for initial imperfections and residual stresses will be employed for all ABAQUS finite element models (Hibbitt, Karlsson & Sorensen, Inc., 1999).

For the half-length models of the noncomposite girders, the S4R elements, an ABAQUS 4-node, thick shell element with 6 degrees of freedom per node, are employed densely spaced at the midspan and gradually decreased spacing to the end support. Sixteen shell elements are assigned across each flange and 16 elements through the web to provide for economical convergence and input for residual stress distribution as in previous studies (see Section 3.2.3). In addition, the number, which must be odd, of integration points through thickness of a shell section is chosen as 5 (default), 15, and 11 for 0.25 inch-web, 0.75 inch-flange, and 0.50 inch-bearing stiffener, respectively.

Figures 3.2.1.1, 3.2.1.2, 3.2.1.3, and 3.2.1.4 illustrate the FEM meshes in initial and deformed shapes of Specimens #1, #2, #3, and #4, respectively. For the half-length numerical model of each specimen, Table 3.2.1.1 presents the total numbers of elements, nodes, and variables are utilized in an ABAQUS nonlinear analysis and the time consumed for a numerical analysis.

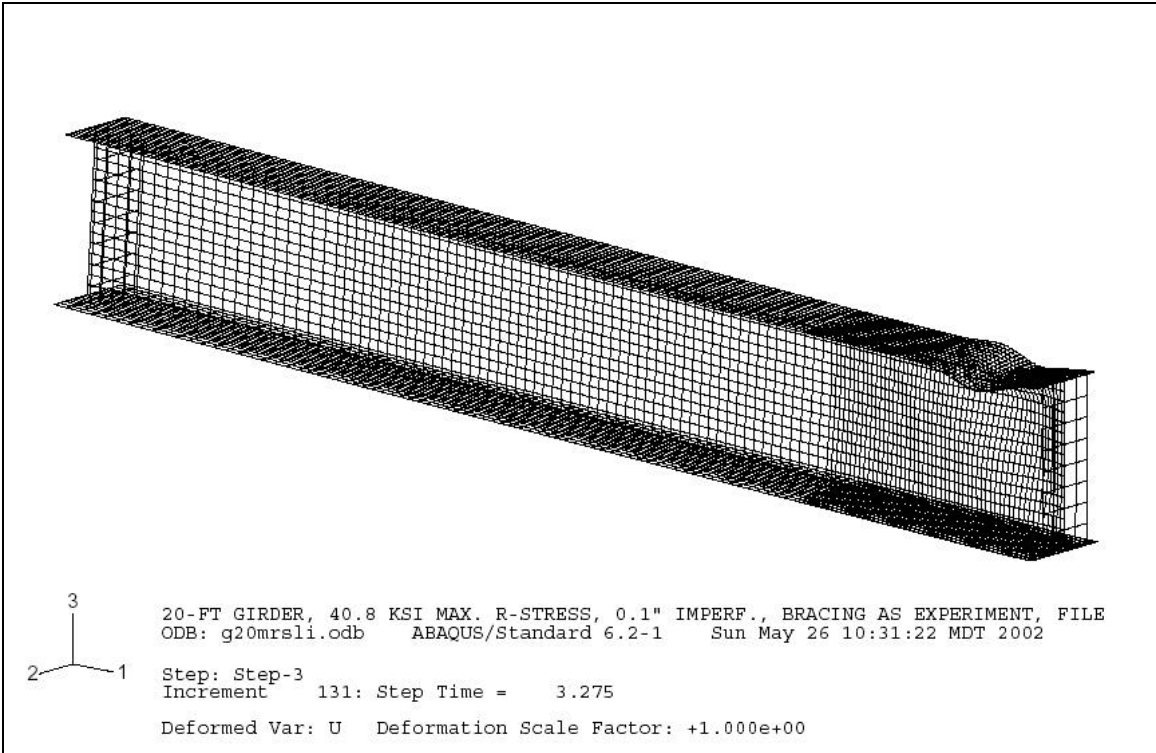
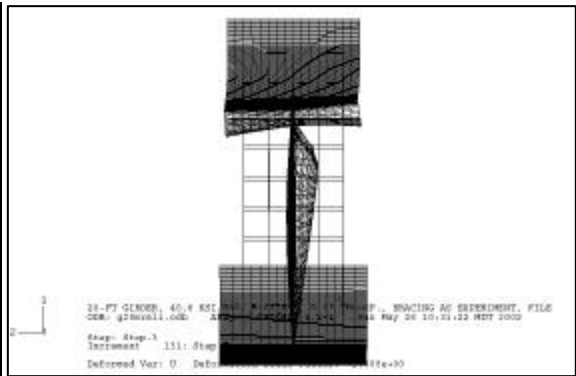
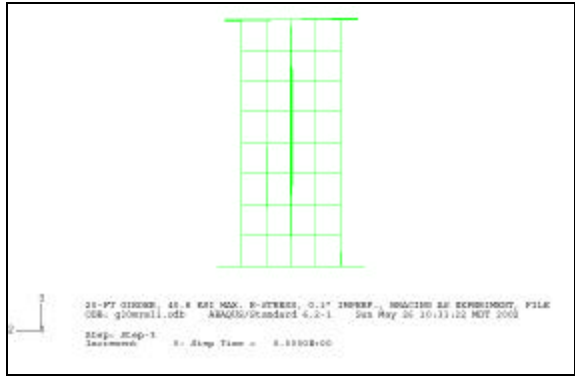
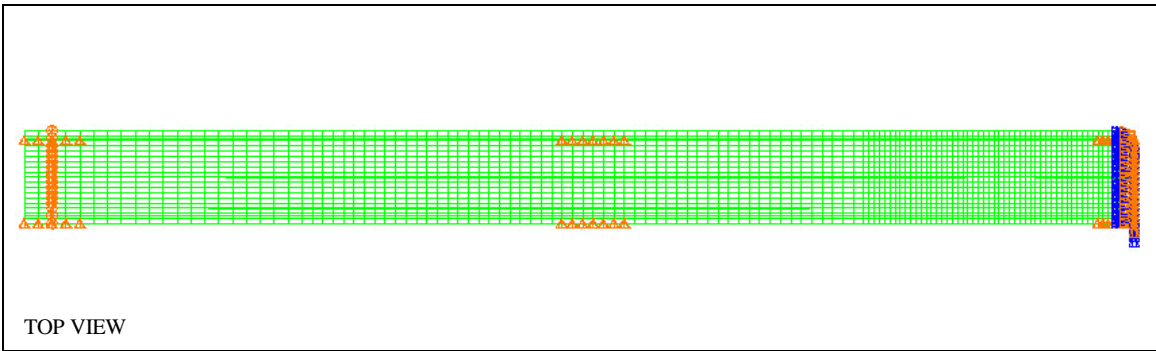


Figure 3.2.1.1 Initial and Deformed Shapes of FEM Model for CSU Specimen #1

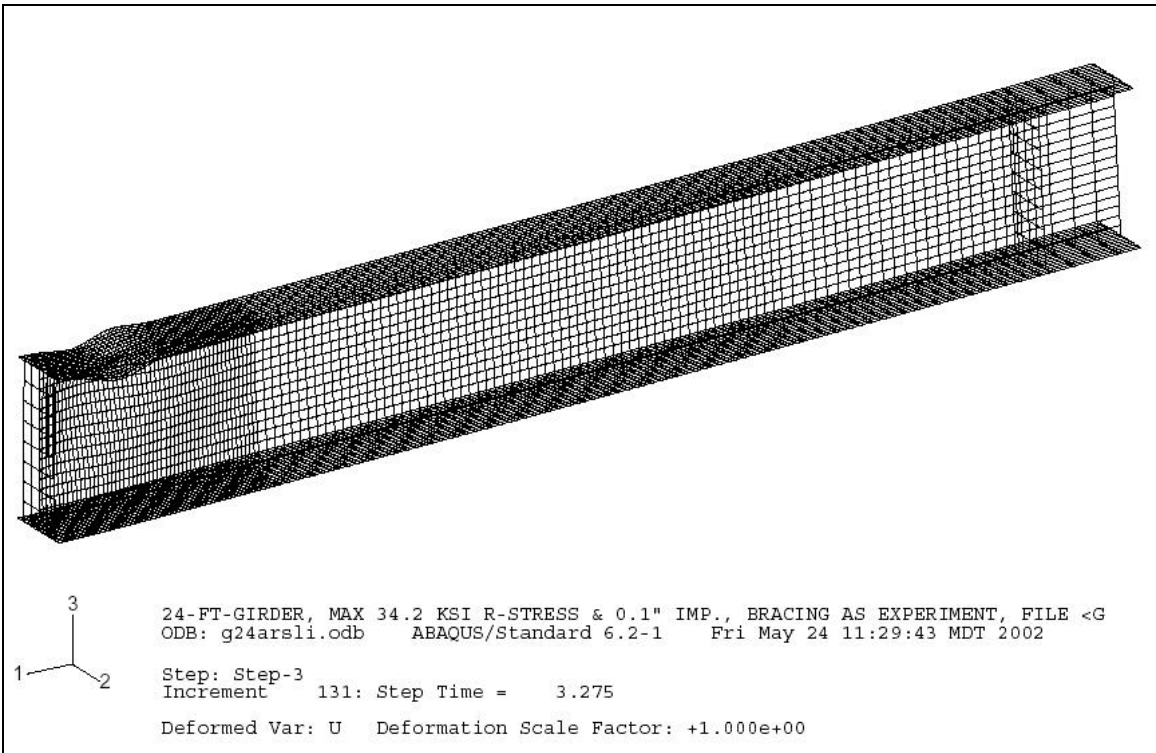
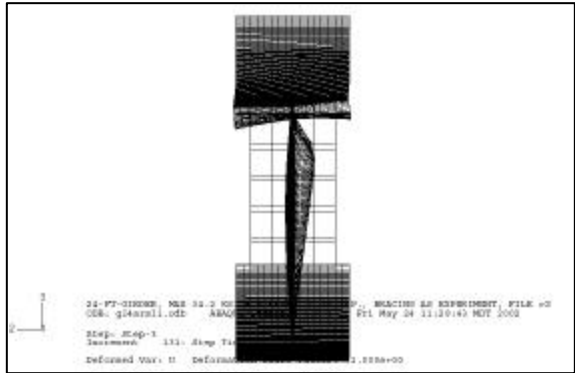
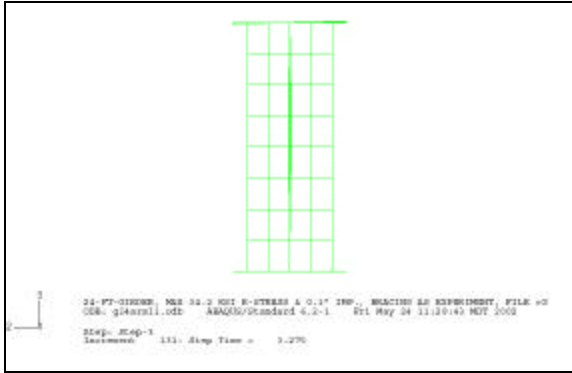
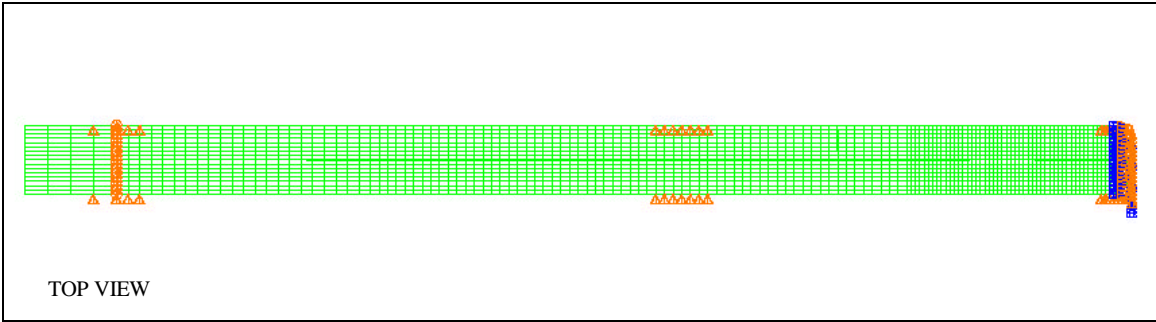


Figure 3.2.1.2 Initial and Deformed Shapes of FEM Model for CSU Specimen #2

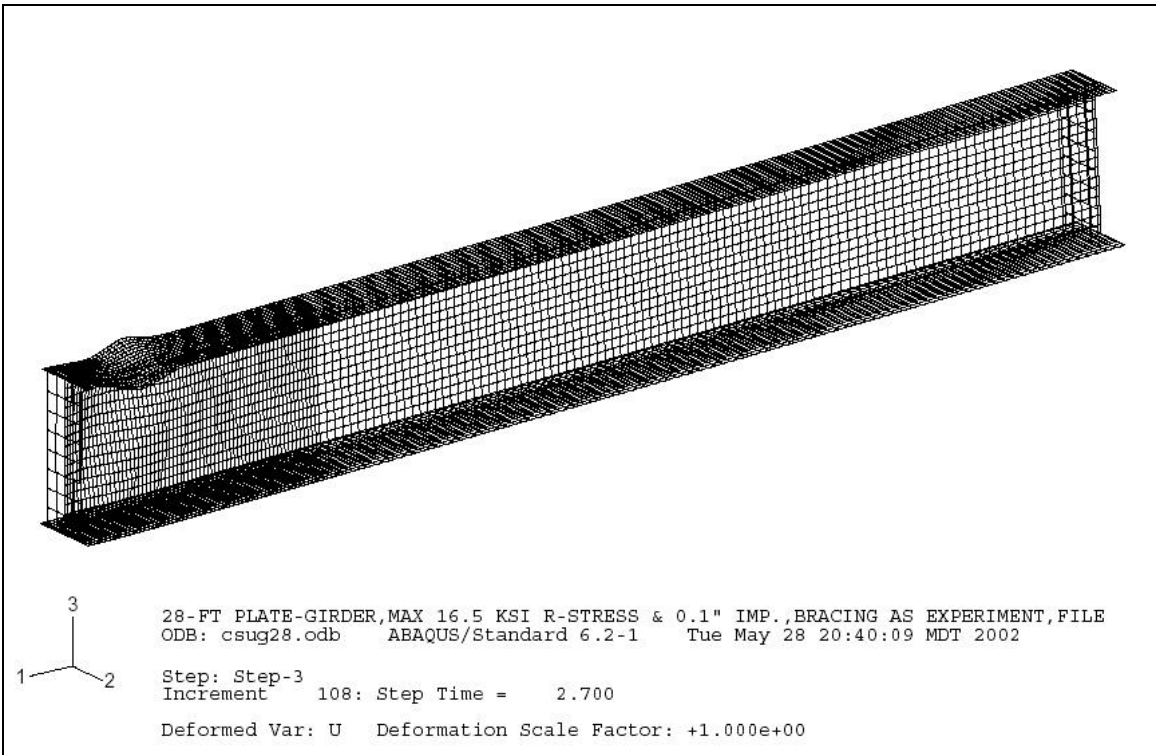
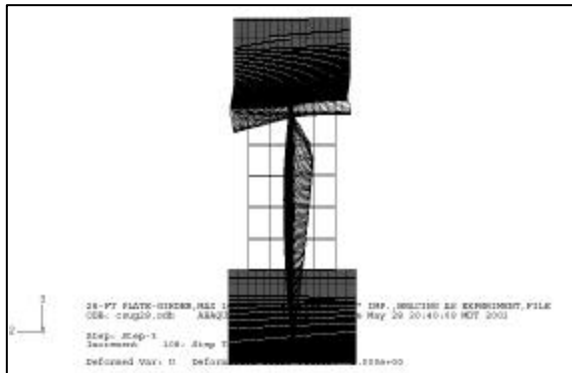
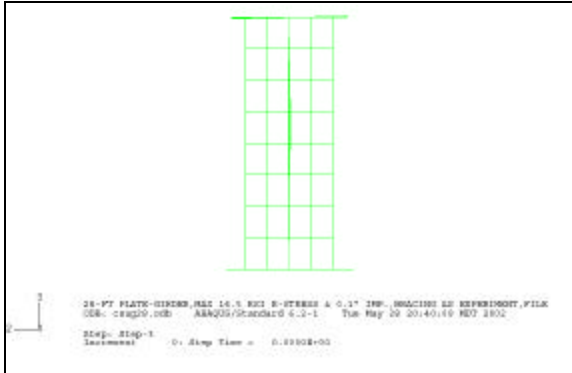
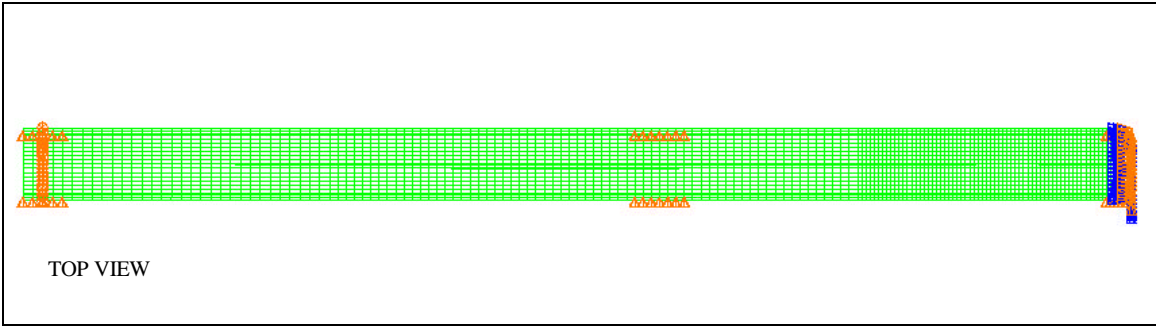


Figure 3.2.1.3 Initial and Deformed Shapes of FEM Model for CSU Specimen #3

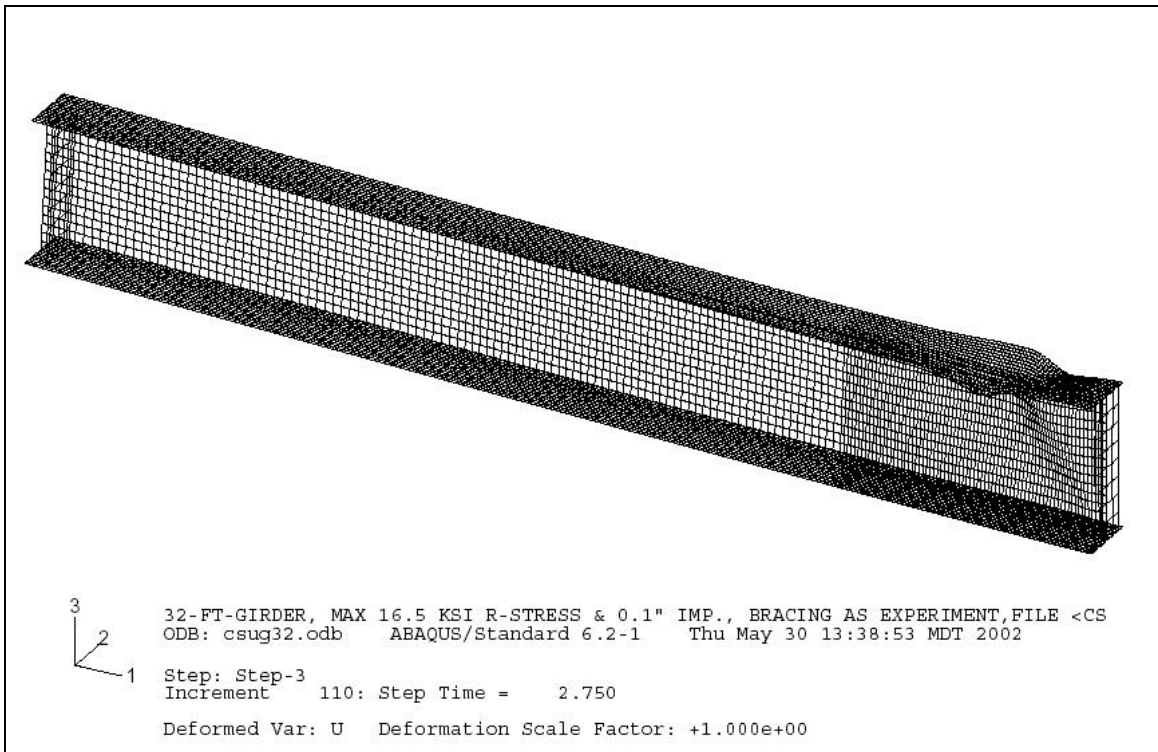
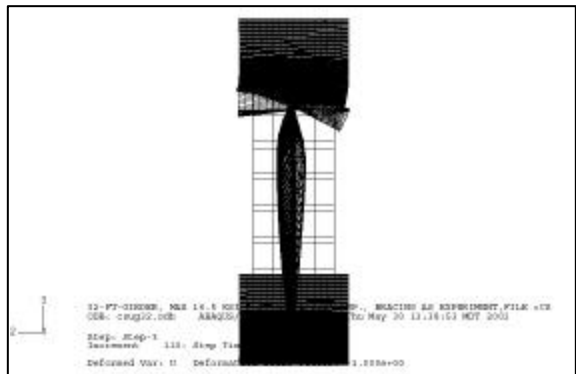
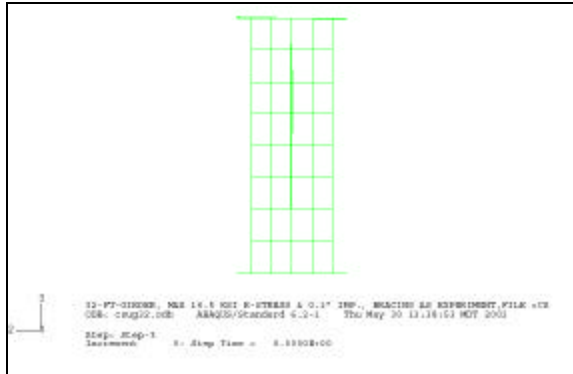
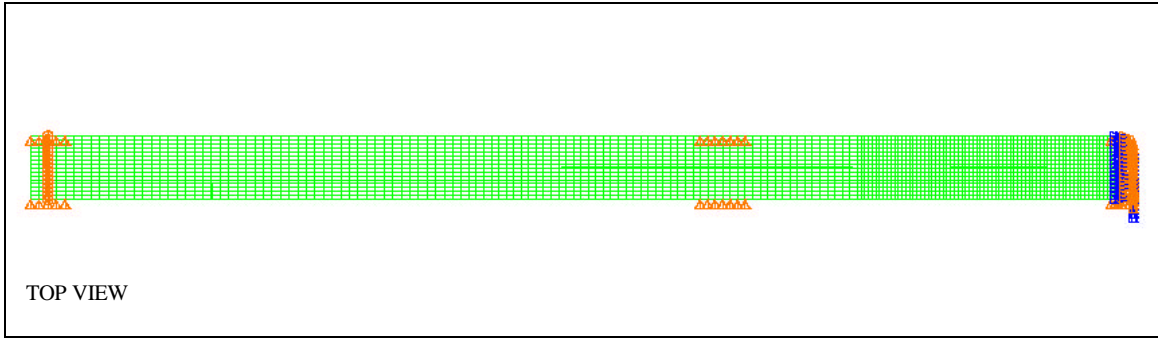


Figure 3.2.1.4 Initial and Deformed Shapes of FEM Model for CSU Specimen #4

Property	Model for Specimen #1	Model for Specimen #2	Model for Specimen #3	Model for Specimen #4
Number of elements	6112	6784	7792	8560
Number of nodes	6279	6965	7994	8778
Number of variables	37674	41790	47964	52668
Time consumed	24 hours	34 hours	38 hours	38 hours

3.2.2 Materials Inputs for Numerical Models

The moment-rotation behavior, obtained from numerical models, of HPS70W I-shape girders at intermediate support regions is complex. Beside the inputs of residual stresses and imperfection, several parametrical variations in the material stress-strain relationship can result in changes in moment-rotation response of the numerical models. In previous studies, different authors used different typical options of material inputs for numerical models of HPS70W girders. For instance, the ratio of yield strains, ϵ_{st}/ϵ_y , was employed as 10 (White, Barth, and Bobb, 1998), or 6.4 (Barth and White, 1998), or 5.5 (Zubeck, 2000). In addition, a “yield plateau slope” was applied as 100 ksi preceding a first strain-hardening slope, $E_{st} = 800$ ksi (or 400 ksi), (White, Barth, and Bobb, 1998), or another “yield plateau slope” could be chosen as 136.9 ksi corresponding to a first strain-hardening slope, $E_{st} = 364.1$ ksi, that was followed by a second and a third strain-hardening slope of 197.2 ksi and 81.5 ksi, respectively (Zubeck, 2000). Furthermore, there were various values for the modulus of elasticity of the flange steel and web steel, E_{flange} and E_{web} , in Appendices B1 and B2 of the Yakel, Mans, and Azizinamini’s report (1999).

In addition, according to “High Performance Steels for Bridges: HPS70W - A Technical Overview” by Bethlehem Lukens Plate, (Bethlehem Lukens Plate 1999), the average value of the yield strength, F_y , and the yield ratio, $YR = F_y/F_u$, is approximately 82 ksi and 0.86, respectively. Figure 3.2.2.1 below displays statistical data for 240 plates of HPS70W in thickness ranging from 0.5 to 3.1 in.

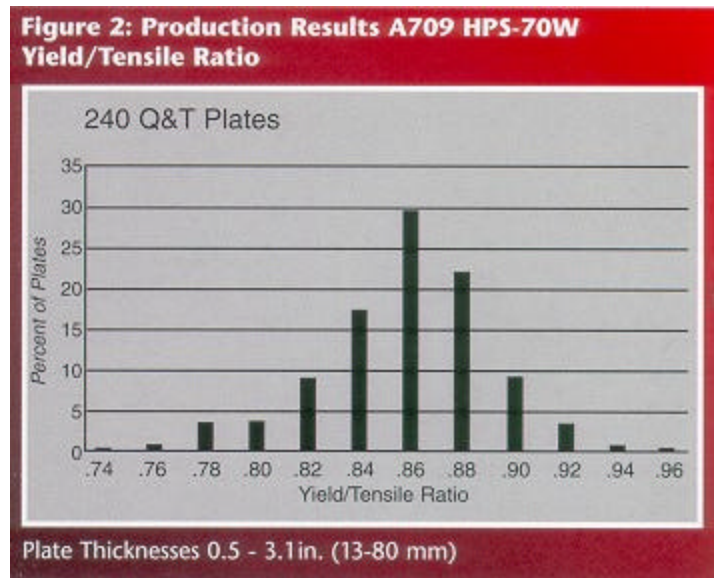
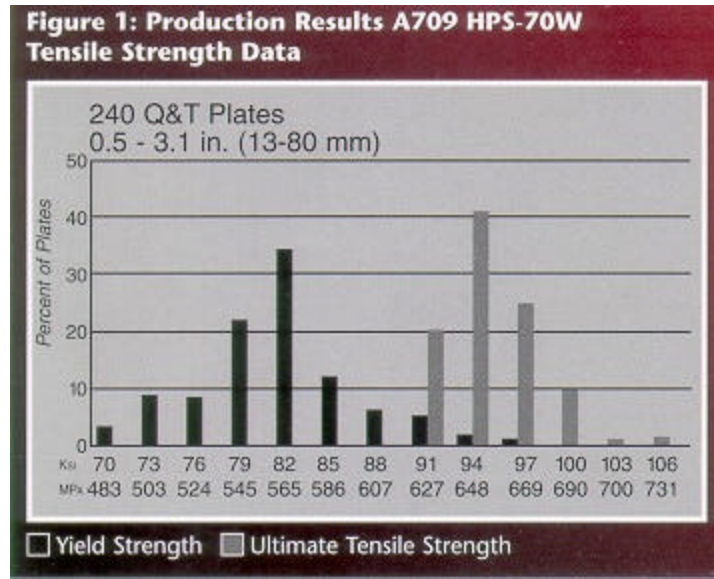


Figure 3.2.2.1 Statistical Data of the Yield Strength, Ultimate Strength, and Yield Ratio for HPS70 Plates.
 (Source: Bethlehem Lukens Plate 1999, 008-HPS-70W Brochure, Figures 1 and 2)

Hence, to decide proper material inputs for numerical models of HPS70W girders at CSU, tensile tests on a number of flange coupons and web coupons (see Section 2.3.1) were performed to determine the values of the modulus of elasticity, E , and the stress-strain relationships of HPS70W, which are displayed in Figures 3.2.2.2 and 3.2.2.3. For the moment-rotation analyses, the CSU numerical outcomes are thus calculated from the combination of the material inputs in Table 3.2.2.1 below and the artificial inputs of initial imperfection and residual stresses as discussed in Section 3.2.3 following.

Table 3.2.2.1 HPS70W Material Inputs for Numerical Moment-Rotation Analyses		
Material properties	HPS70W flanges	HPS70W web
Modulus of elasticity, E	30,113.1 ksi	23,354.3 ksi
2 nd slope approaching the 0.2% offset yield strength	NA	6,500 ksi
Yield plateau slope	4.4 ksi	No yield plateau
Yield strength, F_y	83.35 ksi	69.83 ksi (0.2% offset F_y)
Ratio of yield strains, e_{st}/e_y	6.4	NA
1 st strain-hardening slope, E_{st}	290 ksi	1,200 ksi
2 nd strain-hardening slope	110 ksi	450 ksi
3 rd strain-hardening slope	NA	140 ksi
Ultimate strength, F_u (flat plateau)	93.82 ksi	103.5 ksi
Yield ratio, $YR = F_y/F_u$	0.89	0.67
Poisson's ratio, ?	0.3	0.3

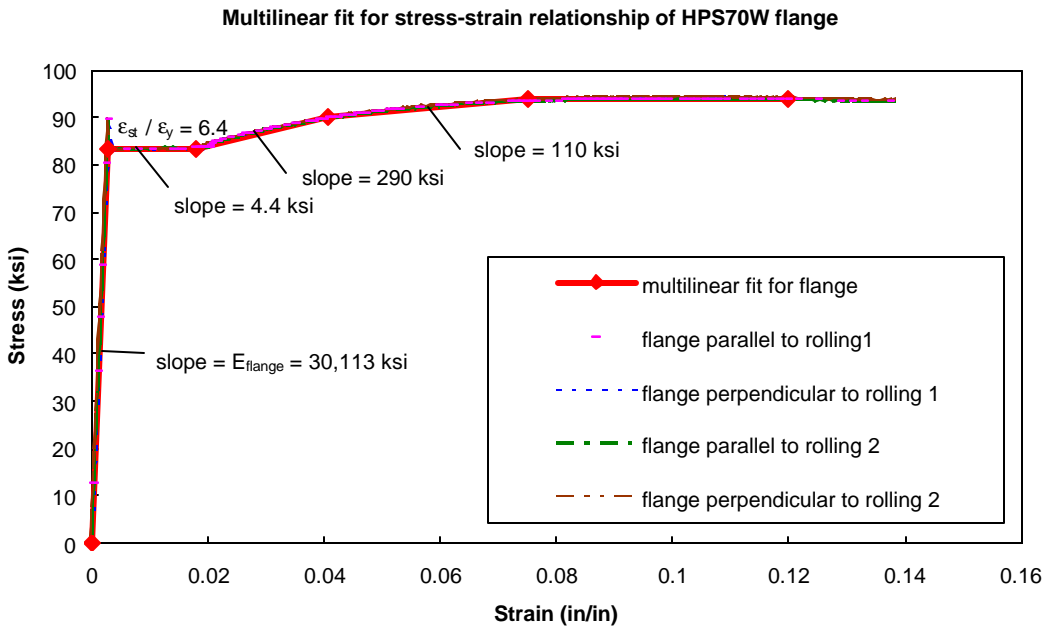


Figure 3.2.2.2 Experimental Engineering Stress-Strain Relationship for the Flanges as Material Inputs for Numerical Analyses of HPS70W Girders

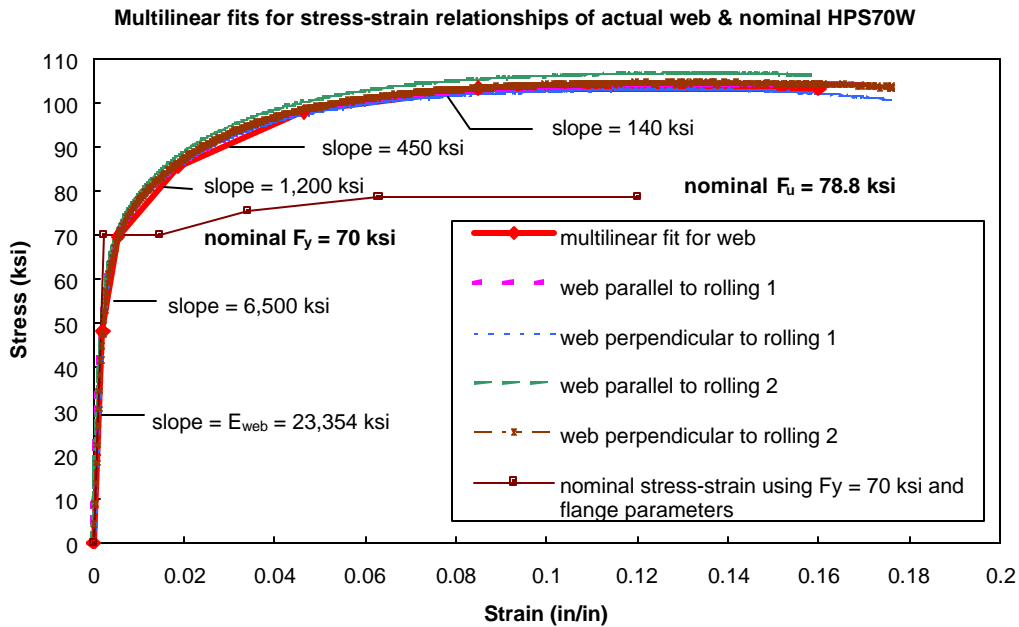


Figure 3.2.2.3 Experimental Engineering Stress-Strain Relationship for the Web as Material Inputs for Numerical Analyses of HPS70W Girders

3.2.3 Inputs of Initial Imperfections and Residual Stresses for Numerical Models

In this research, the residual stresses are introduced as a constant value over each element. Following the values suggested previously (Yakel, Mans, and Azizinamini 1999; Zubeck 2000), the maximum positive residual stress is assigned as $+\frac{0.98}{2} F_{yf} = \frac{0.98}{2} (83.35 \text{ ksi}) \approx +40.8 \text{ ksi}$ (the peak value is divided by two for going from ramp distribution to block distribution), and the maximum negative residual stress is applied as $-\frac{0.98}{3} F_{yf} = -\frac{0.98}{3} (83.35 \text{ ksi}) \approx -27.2 \text{ ksi}$ for the flanges of Specimen #1. For the web of Specimen #1, the maximum positive residual stress is employed again as +40.8 ksi for the elements at the flange-web connectivity while the constant negative residual stress is specified as $-\frac{0.98}{9} F_{yw} = -\frac{0.98}{9} (69.83 \text{ ksi}) \approx -7.6 \text{ ksi}$ (see Table 3.2.3.1). In addition, to account for the tendency of a deeper web to have lower residual stresses at the web-flange junction, the piecewise residual stress distributions for the flanges and the web were adjusted to apply to Specimens #2, #3, and #4. Based on $F_{yw} = 69.83 \text{ ksi}$, Table 3.2.3.2 presents the distribution of initial residual stresses for Specimen #2 (web depth of 19 in.) with a maximum positive residual stress of +34.2 ksi and maximum negative residual stress of -22.8 ksi, which are lower in magnitude than those of Specimen #1 (web depth of 16 in.). Furthermore, if the maximum residual stress of +16.5 ksi for welded shape according to AISC LRFD design (AISC 1998) is applied, the residual stress distributions over web and flanges are proportioned from the maximum value of +40.8 ksi to the corresponding peak of +16.5 ksi. Table 3.2.3.3 presents the distribution of initial residual stresses for Specimen #3 (web depth of 21 in.) and Specimen #4 (web depth of 25 in.).

Table 3.2.3.1 Distribution of Initial Residual Stresses for Specimen #1									
Residual stresses (ksi) in Specimen #1 (nonsymmetric)									
Element	1	2	3	4	5	6	7	8	9 to 16
Upper flange	+40.8	+13.6	-27.2	-27.2	-27.2	-27.2	+13.6	+40.8	symmetric of 1 to 8
Web	+40.8	+4.8	-7.6	-7.6	-7.6	-7.6	-7.6	-7.6	
Lower flange	+28.2	+9.4	-27.2	-27.2	-27.2	-27.2	+13.6	+40.8	

Table 3.2.3.2 Distribution of Initial Residual Stresses for Specimen#2									
Residual stresses (ksi) in Specimen #2 (symmetric)									
Element	1	2	3	4	5	6	7	8	9 to 16
Flanges	+34.2	+11.4	-22.8	-22.8	-22.8	-22.8	+11.4	+34.2	symmetric

Web	+34.2	+11.4	-7.6	-7.6	-7.6	-7.6	-7.6	-7.6	of 1 to 8
Table 3.2.3.3 Distribution of Initial Residual Stresses for Specimens #3 and #4									
Residual stresses (ksi) in Specimen #3 (nonsymmetric)									
Element	1	2	3	4	5	6	7	8	9 to 16
Upper flange	+16.5	+5.5	-11.0	-11.0	-11.0	-11.0	+5.5	+16.5	symmetric of 1 to 8
Web	+16.5	+1.9	-3.1	-3.1	-3.1	-3.1	-3.1	-3.1	
Lower flange	+11.8	+3.9	-11.0	-11.0	-11.0	-11.0	+5.5	+16.5	
Residual stresses (ksi) in Specimen #4 (symmetric)									
Element	1	2	3	4	5	6	7	8	9 to 16
Flanges	+16.5	+5.5	-11.0	-11.0	-11.0	-11.0	+5.5	+16.5	symmetric of 1 to 8
Web	+16.5	+1.9	-3.1	-3.1	-3.1	-3.1	-3.1	-3.1	

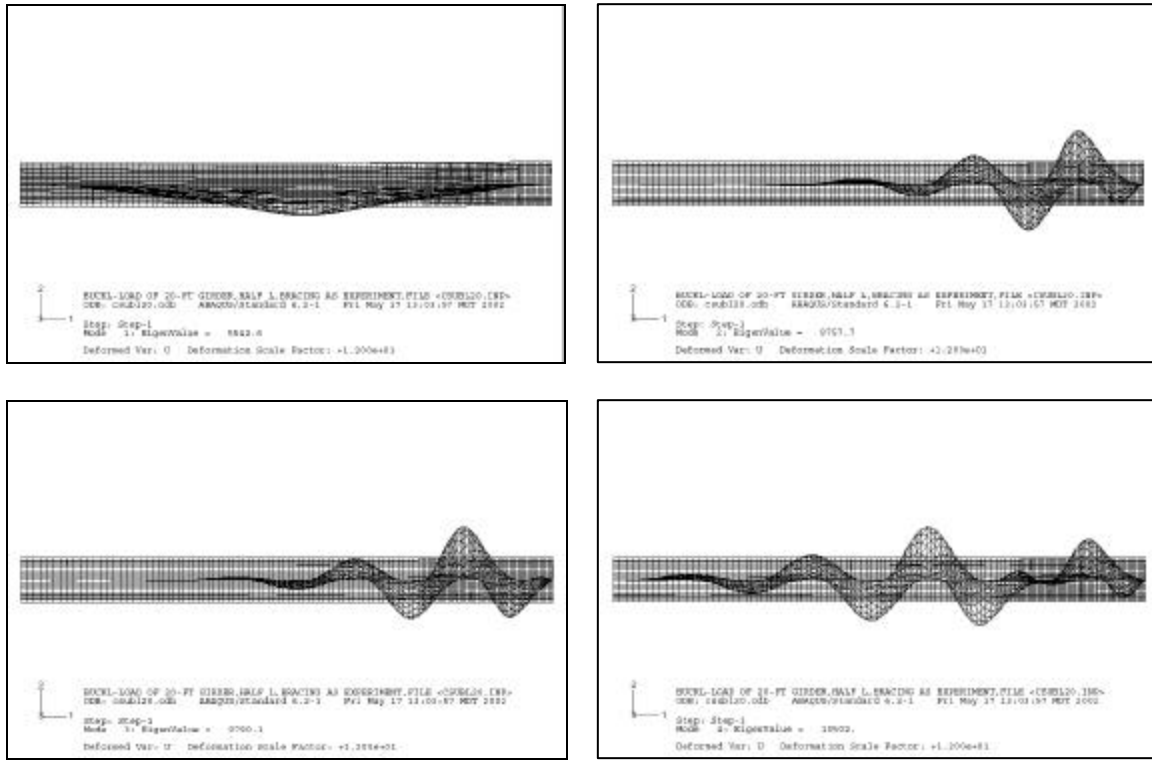


Figure 3.2.3.1 The First Four Eigenmodes of Buckling Analysis for Specimen #1

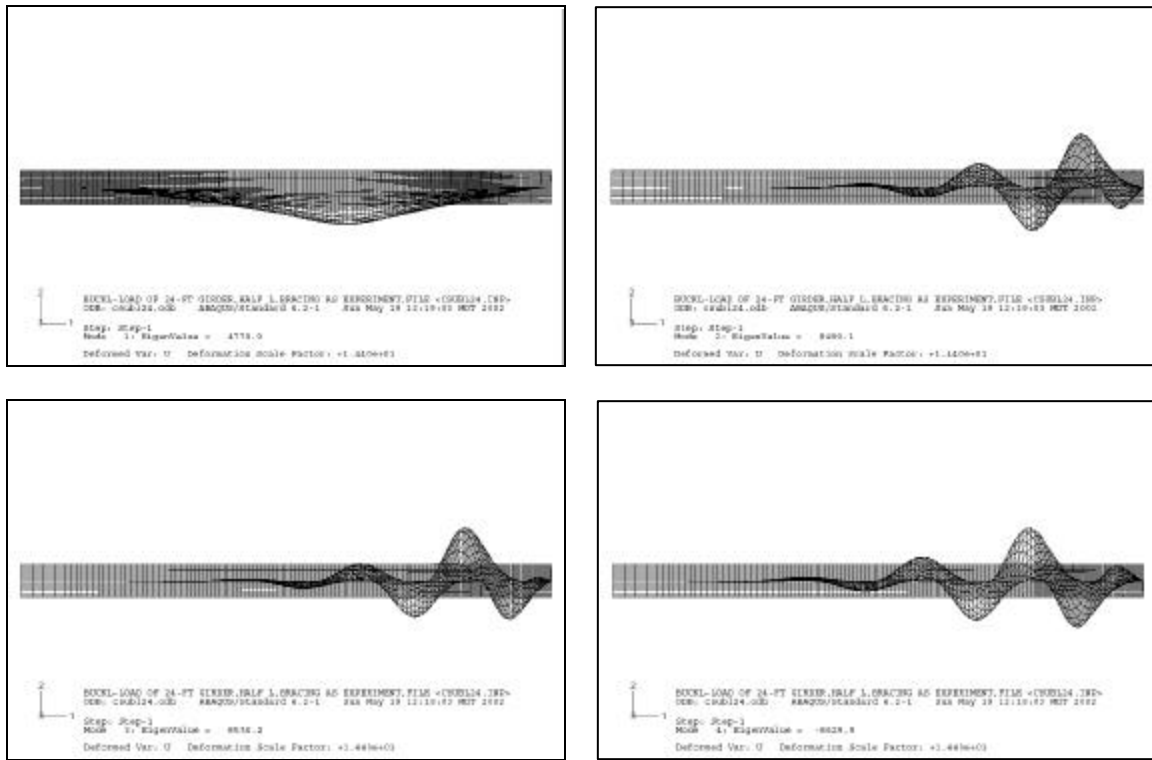


Figure 3.2.3.2 The First Four Eigenmodes of Buckling Analysis for Specimen #2

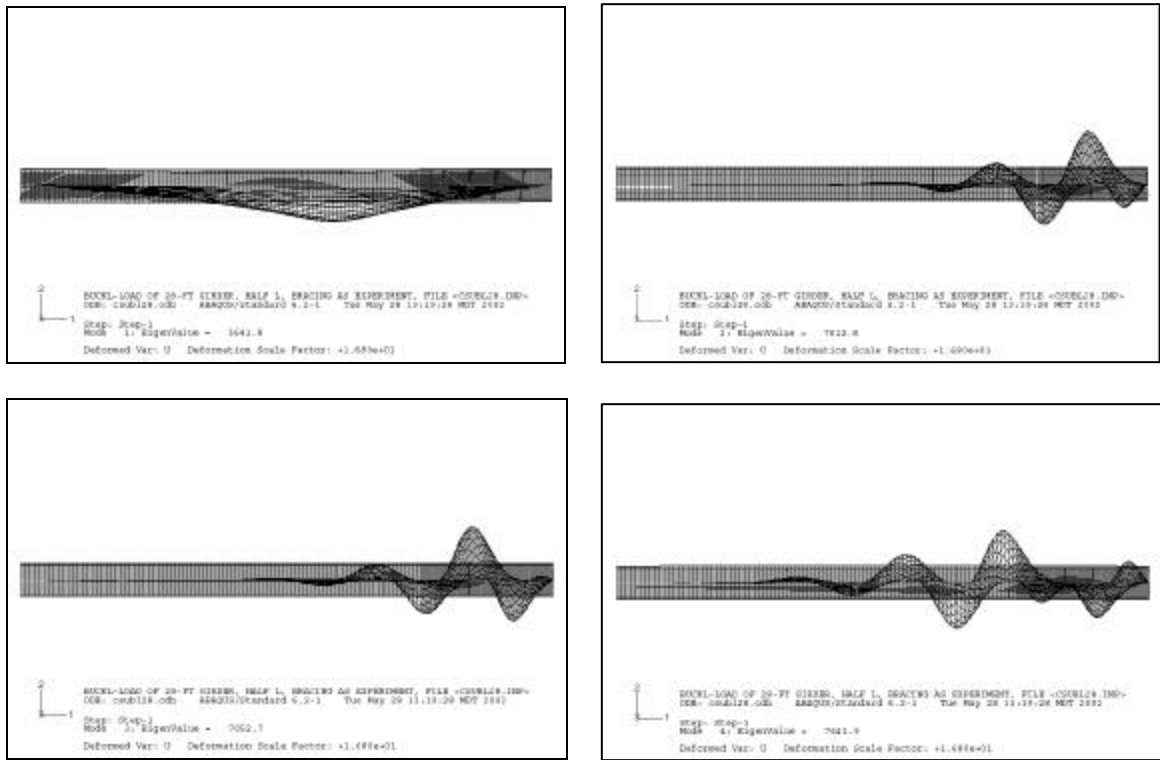


Figure 3.2.3.3 The First Four Eigenmodes of Buckling Analysis for Specimen #3

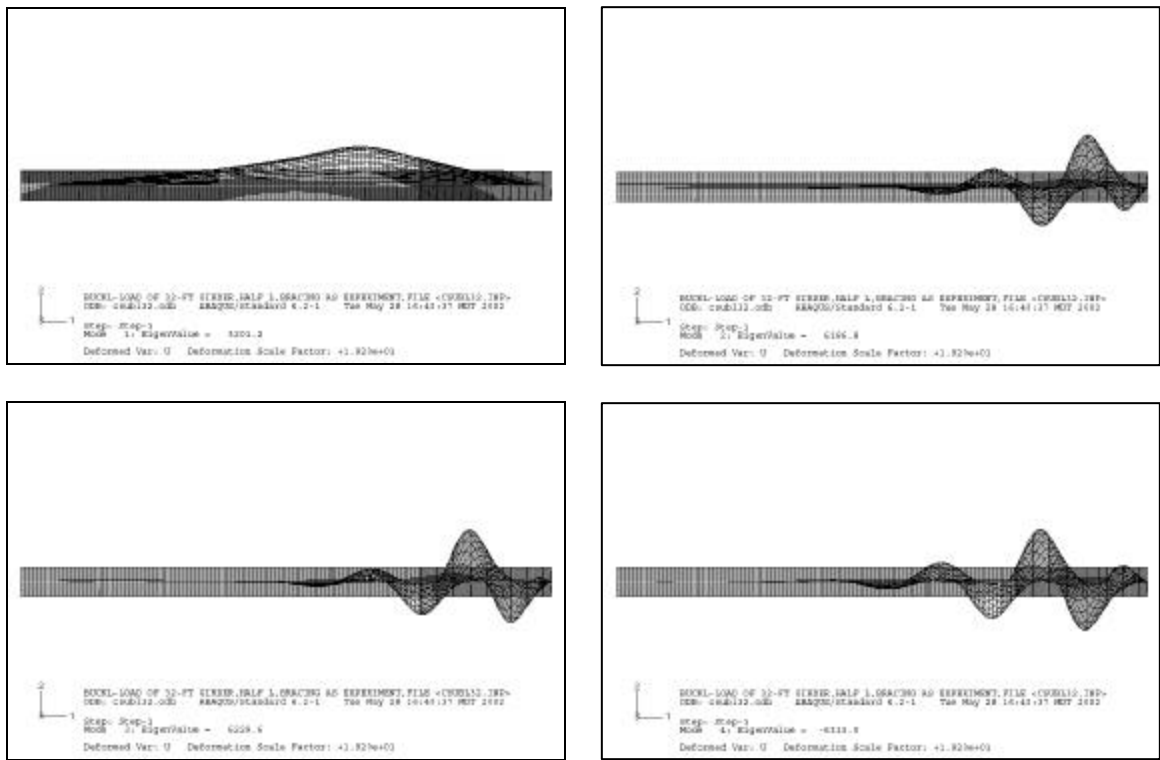


Figure 3.2.3.4 The First Four Eigenmodes of Buckling Analysis for Specimen #4

The imperfection input for numerical analyses was modeled similarly to the method of Yakel, Mans, and Azizinamini (1999), in which the resulting first-eigenvector from the buckling analysis was scaled down such that the maximum displacement was 0.1 inch, and these scaled displacements were superimposed on the original geometry thus generating a distorted mesh. However, in this research, an arbitrary combination of eigenvectors, which are weighted descending from the first-eigenvector down to the fourth (as noted in ABAQUS post-peak analysis procedures (Hibbitt, Karlsson & Sorensen, Inc., 1999)), can be scaled down such that the maximum combined displacement is from 0.1 to 0.2 inch and then applied as an initial imperfection. Figures 3.2.3.1, 3.2.3.2, 3.2.3.3, and 3.2.3.4 in the previous pages present the first four eigenmodes of the buckling analyses for Specimens #1, #2, #3, and #4, respectively.

3.2.4 Numerical Studies of Bracing Lengths for Specimens #3 and #4

Lateral bracing along the compression flange prevents lateral torsional buckling, and thus ensures that a girder meeting compact section requirements can reach its inherent plastic moment capacity. The effects of lateral bracing lengths on pier moment-rotation behavior of CSU's HPS70W Ishape noncompact girders, Specimen #3 and Specimen #4, were studied from the response of the specimens with lateral compression-flange bracing classified as either satisfying or dissatisfying the AASHTO requirements (AASHTO, 1998 and interims through 2001) categories.

In three-point loading, the midspan (at the load point) is the most critical region of a girder for lateral torsional buckling. As a result, lateral bracing is first assigned at the midspan of the test girders, and the compression flange bracing from the load point to the next compression flange brace is checked against the maximum unbraced length permitted by AASHTO (see Section 2.1.1):

- Specimen #3 (half span $L/2 = 330 \text{ in} / 2 = 165 \text{ in}$, triangular moment diagram):

If AASHTO 6.10.4.1.7 specification is applied for compact section, the maximum unbraced length, L_p , is:

$$L_p = \left(0.124 - 0.0759 \left(\frac{M_l}{M_p} \right) \right) \left(\frac{r_y E}{F_{yc}} \right) = \left\{ 0.124 - 0.0759 \left(\frac{(165 \text{ in} - L_p)}{165 \text{ in}} M_p \right) \right\} \left(\frac{(2.634 \text{ in})(29000 \text{ ksi})}{70 \text{ ksi}} \right)$$

$$\underline{L_p = 105.4 \text{ in}}$$

If AASHTO 6.10.4.1.8 specification is applied for noncompact section, the maximum unbraced length, L_p , is:

$$L_p = 1.76 r_t \sqrt{\frac{E}{F_{yc}}} = 1.76 (2.727 \text{ in}) \sqrt{\frac{29000 \text{ ksi}}{70 \text{ ksi}}} = \underline{97.7 \text{ in}}$$

- Specimen #4 (half span $L/2 = 378 \text{ in} / 2 = 189 \text{ in}$, triangular moment diagram):

If AASHTO 6.10.4.1.7 specification is applied for compact section, the maximum unbraced length, L_p , is:

$$L_p = \left(0.124 - 0.0759 \left(\frac{M_l}{M_p} \right) \right) \left(\frac{r_y E}{F_{yc}} \right) = \left\{ 0.124 - 0.0759 \left(\frac{\left(\frac{189 \text{ in} - L_p}{189 \text{ in}} \right) M_p}{M_p} \right) \right\} \left(\frac{(2.705 \text{ in})(29000 \text{ ksi})}{70 \text{ ksi}} \right)$$

$$\underline{L_p = 98.0 \text{ in}}$$

If AASHTO 6.10.4.1.8 specification is applied for noncompact section, the maximum unbraced length, L_p , is:

$$L_p = 1.76 r_t \sqrt{\frac{E}{F_{yc}}} = 1.76 (2.992 \text{ in}) \sqrt{\frac{29000 \text{ ksi}}{70 \text{ ksi}}} = \underline{107.1 \text{ in}}$$

Specimen #3 was experimentally tested with lateral compression-flange bracing configuration at midspan, 71.5 in. North and South from midspan, and at supports, which satisfies the AASHTO specifications (AASHTO, 1998 and interims through 2001) for both categories of compact and noncompact sections. Numerically, the finite element model for Specimen #3 was analyzed with four variations of lateral compression-flange bracing:

- (1) bracing at midspan, 71.5 in. North and South from midspan, and at supports as experiment (unbraced length, L_b , satisfies AASHTO specifications for both compact and noncompact sections),
- (2) bracing at midspan, 97.75 in. North and South from midspan (at limited unbraced length for noncompact section from AASHTO 6.10.4.1.8 specification), and at supports,
- (3) bracing at midspan, 105.25 in. North and South from midspan (at limited unbraced length for compact section from AASHTO 6.10.4.1.7 specification), and at supports, and
- (4) bracing only at midspan and at supports (L_b does not satisfy AASHTO specifications).

The effects of the various unbraced lengths on the inelastic moment-rotation relationship for Specimen #3 resulted from the four numerical models either satisfying or dissatisfying the AASHTO specifications of lateral compression-flange bracing are presented in Section 4.3.

The numerical model of Specimen #4 was analyzed with two corresponding bracing configurations as experiments (see Section 2.2.5):

- (1) bracing at midspan, 71.5 in. North and South from midspan (unbraced length, L_b , satisfies AASHTO specifications (AASHTO, 1998 and interims through 2001) for compact section (at 98 in) and noncompact section (at 107.1 in)), and at supports, and
- (2) bracing only at midspan and at supports (L_b does not satisfy AASHTO specifications).

The effects of the various unbraced lengths on the inelastic moment-rotation relationship for Specimen #4 resulted from the two numerical models either satisfying or dissatisfying the AASHTO specifications of lateral compression-flange bracing are presented in Section 4.3.

4. PIER MOMENT-ROTATION BEHAVIOR OF HPS70W I-GIRDERS

4.1 Introduction

The pier moment-rotation behavior of HPS70W I-shape girders was synthetically developed from the experimental and numerical responses of specimens classified as either compact or noncompact. In addition, the effects of lateral bracing lengths on pier moment-rotation behavior of CSU's HPS70W I-shape noncompact girders, Specimen #3 and Specimen #4, were studied from the response of the specimens with lateral compression-flange bracing classified as either satisfying or dissatisfying the AASHTO requirements (AASHTO, 1998 and interims through 2001).

Before detailing the experimental moment-rotation results, linear strain distribution was first checked against the elastic neutral axis for each of the noncomposite HPS70W specimens, Specimens #1 to #4. Second, the similarity and difference between some numerical moment-total rotations and corresponding moment-inelastic rotations were noticed. Third, the effects of residual stresses and initial imperfection on numerical models were verified.

Figure 4.1.1 illustrates the linear strain measurements, which vary with loads, through the I-section and the corresponding locations of the elastic neutral axis by intercepting the best-fit lines of linear strain distributions with the vertical axis of the web for Specimen #1. The elastic neutral axis, which is supposed to be at the centroid of the cross section as 8.406 in. from bottom of the lower flange, is shifted upward a little bit, about 0.2 in. to 0.5 in. Similarly, the linear strain distributions through the I-section and the corresponding locations of the elastic neutral axis for Specimens #2, #3, and #4 are demonstrated in Figures 4.1.2, 4.1.3, and 4.1.4, respectively. The locations of the elastic neutral axis, which are 10.25 in., 10.862 in., and 13.25 in. from bottom of the lower flange for Specimens #2, #3, and #4, respectively, are all shifted a little bit from the I-section's centroids upward into the compression zone about 0.2 in. to 0.5 in., which are tolerated.

Figures 4.1.5 and 4.1.6 display the experimental curves and a number of numerical moment-total rotation and moment-inelastic rotation relationships at different locations for the 19.5 ft-span girder (Specimen #1) and the 22 ft-span girder (Specimen #2), respectively. At different locations near the supports as shown in Figures 4.1.5 and 4.1.6 for Specimens #1 and #2, the moment-inelastic rotation relationships are numerically almost identical although the moment-total rotation relationships are different. In the figures, the ascending (elastic) portion of the moment-rotation curves shows that the experimental girders are little bit stiffer than the numerical models. The reason was attributed to the actual modulus of elasticity, E , of HPS70W that is somewhat greater than the numerical inputs for E as in Chapter 3.

Figure 4.1.7 illustrates the effects of initial residual stresses and imperfections on the numerical outcomes of the 19.5 ft-span girder (Specimen #1) and the 22 ft-span girder (Specimen #2). The results agree with previous studies of Yakel, Mans, and Azizinamini (1999) and Zubeck (2000). The effect of residual stresses in the moment-rotation diagram was "rounding off" the curve as the girder yields even though the magnitude of residual stresses has no effect on the ultimate moment capacity. In addition, larger imperfection introduced into the model made the post-plateau portion of the moment-rotation curve descend with steeper slopes although the influence was not significant.

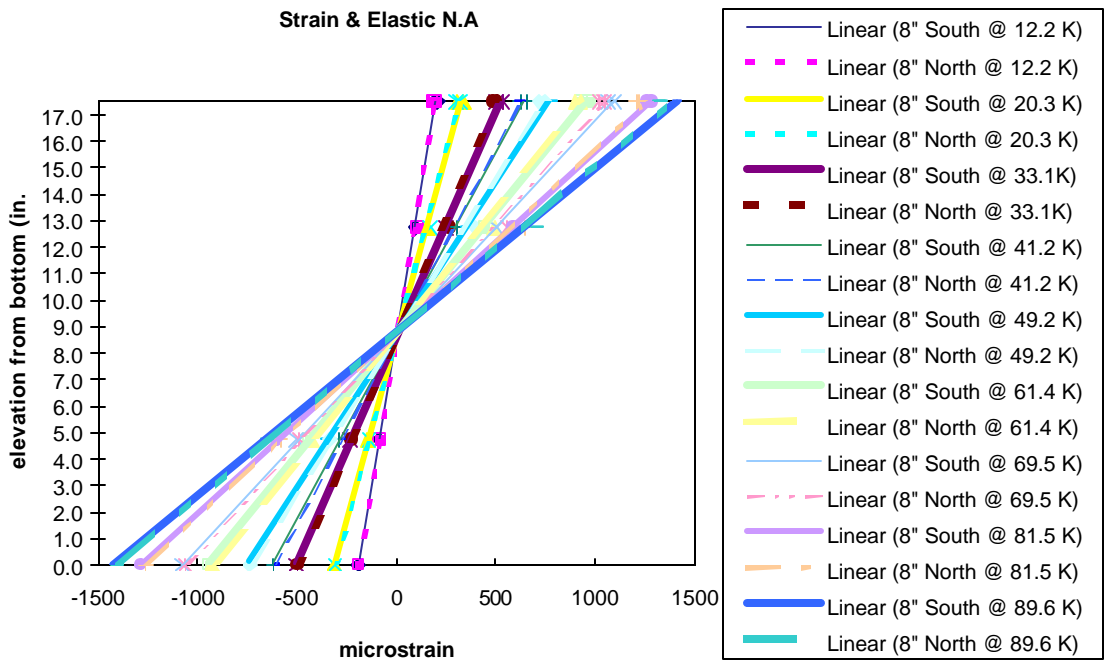


Figure 4.1.1 Linear Strain Distributions Through Cross-Section and Elastic Neutral Axis for Specimen #1

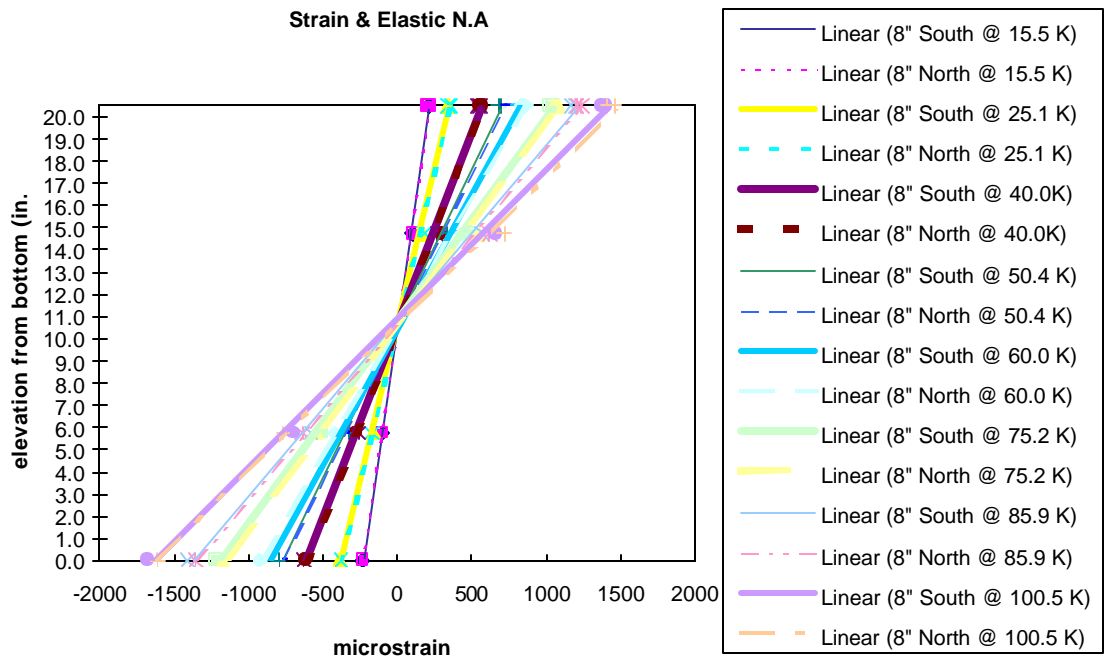


Figure 4.1.2 Linear Strain Distributions Through Cross-Section and Elastic Neutral Axis for Specimen #2

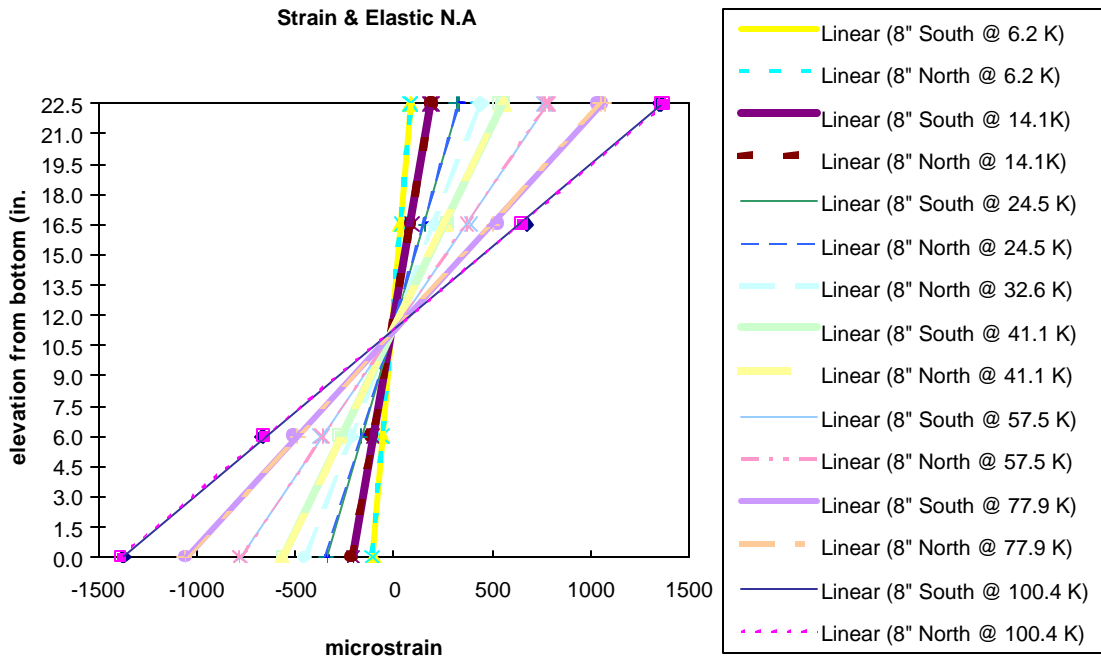


Figure 4.1.3 Linear Strain Distributions Through Cross-Section and Elastic Neutral Axis for Specimen #3

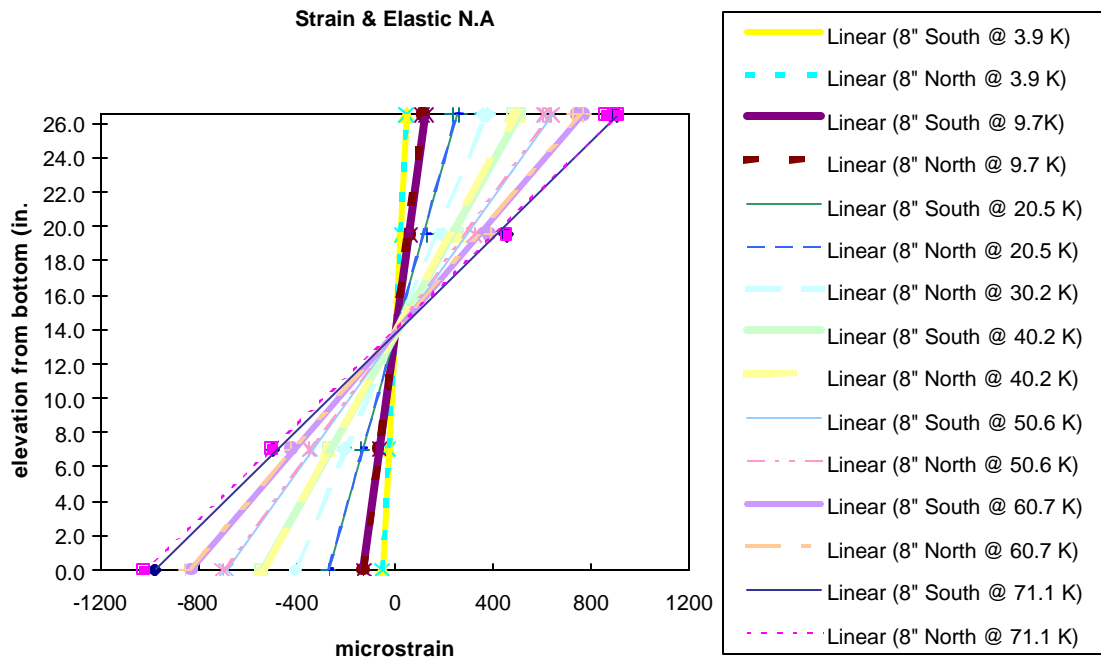
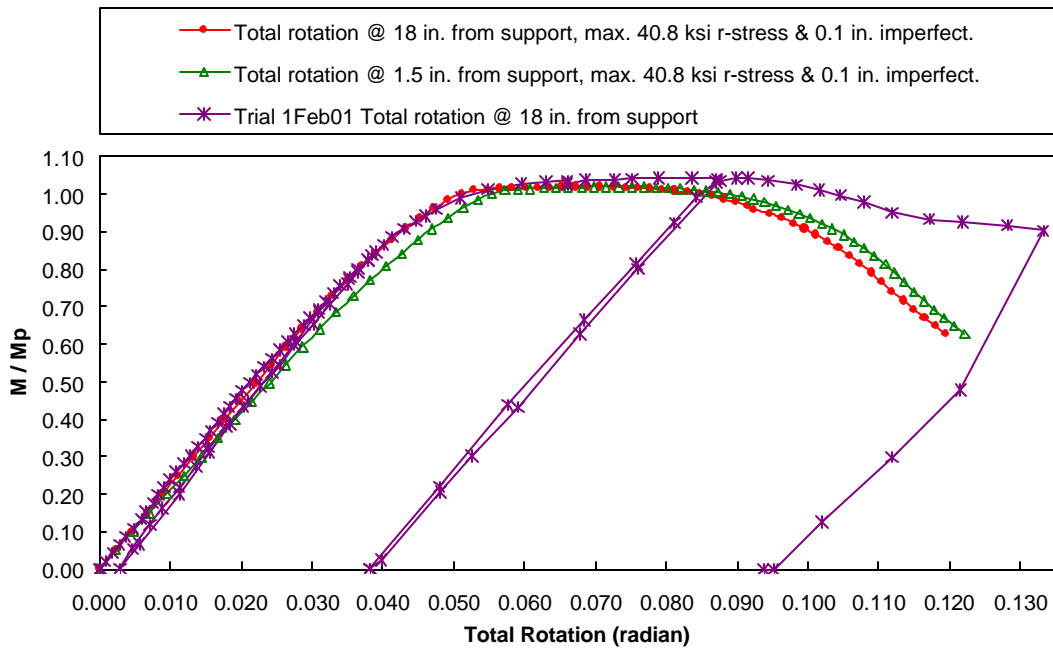


Figure 4.1.4 Linear Strain Distributions Through Cross-Section and Elastic Neutral Axis for Specimen #4

**Specimen #1 - 19.5 ft-span HPS70W girder
Normalized Moment vs. Total Rotation**



**Specimen #1 - 19.5 ft-span HPS70W girder
Normalized Moment vs. Inelastic Rotation**

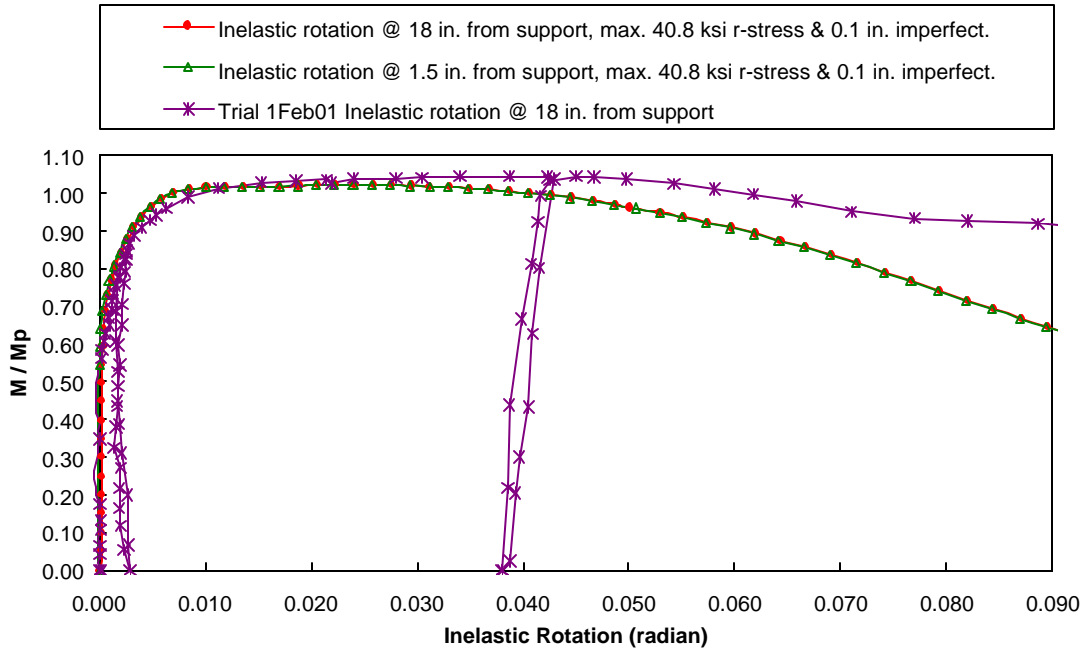
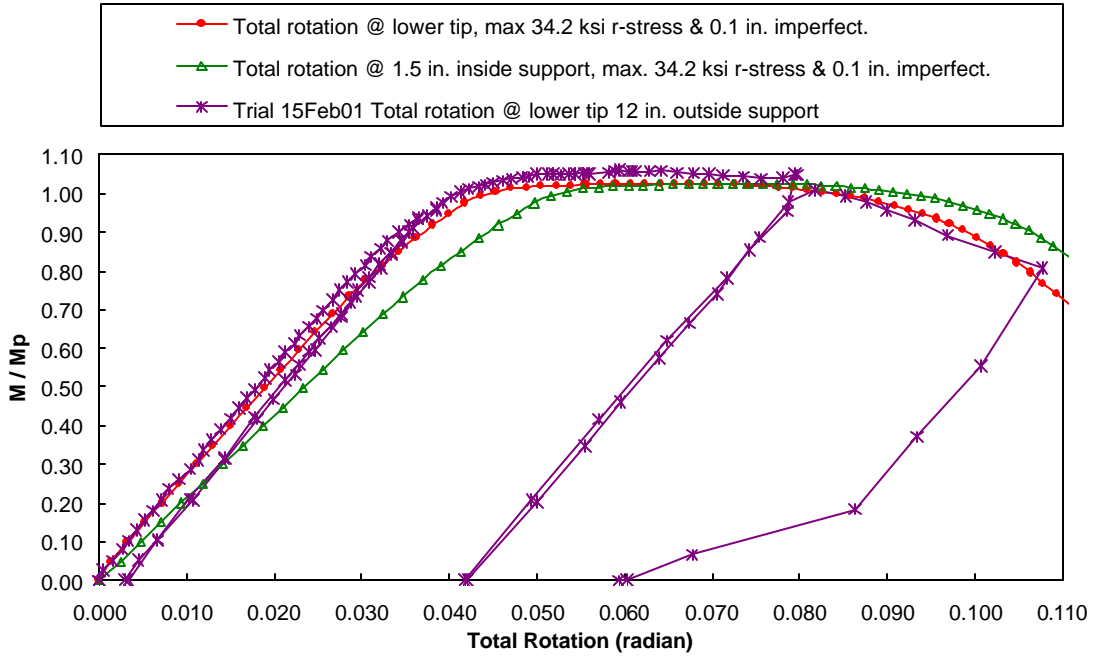


Figure 4.1.5 Specimen #1 - Numerical Moment-Total Rotation and Moment Inelastic Rotation at Different Linear the Supports

**Specimen #2 - 22 ft-span HPS70W girder
Normalized Moment vs. Total Rotation**



**Specimen #2 - 22 ft-span HPS70W girder
Normalized Moment vs. Inelastic Rotation**

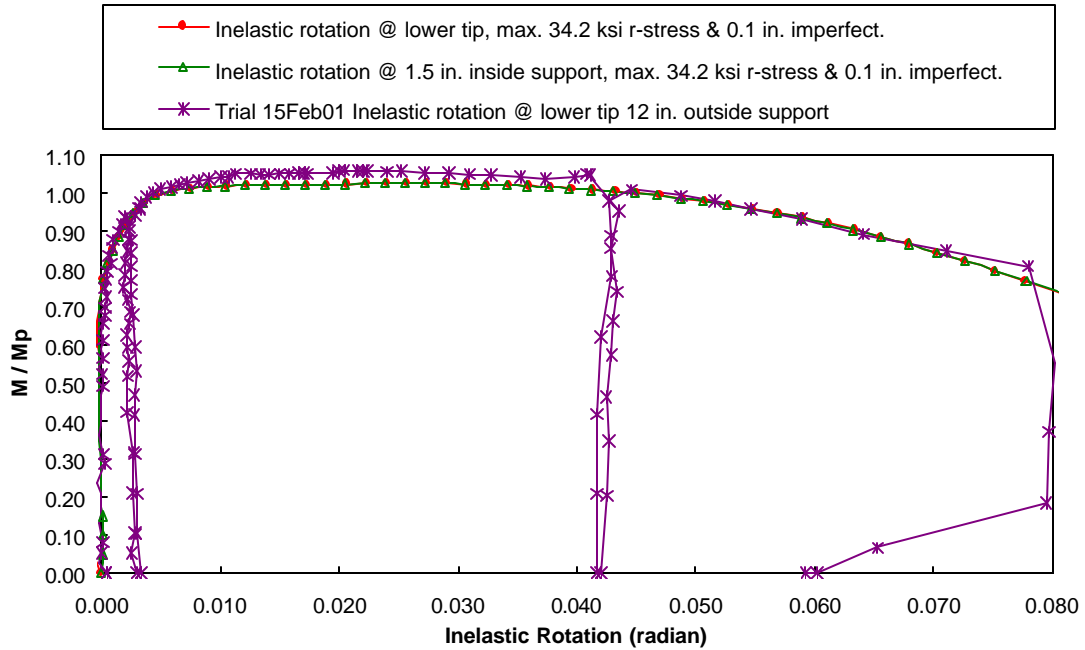
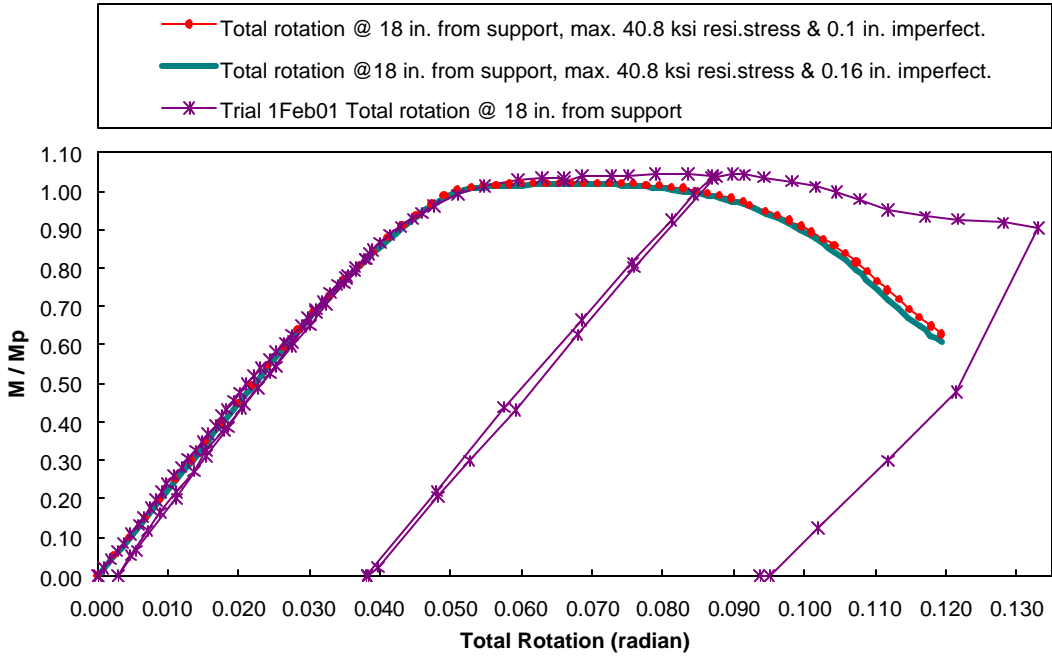


Figure 4.1.6 Specimen #2 - Numerical Moment-Total Rotation and Moment Inelastic Rotation at Different Locations Near the Supports

**Specimen #1 - Normalized Moment vs. Total Rotation
Effects of Initial Imperfection**



**Specimen #2 - Normalized Moment vs. Total Rotation
Effects of Residual Stresses**

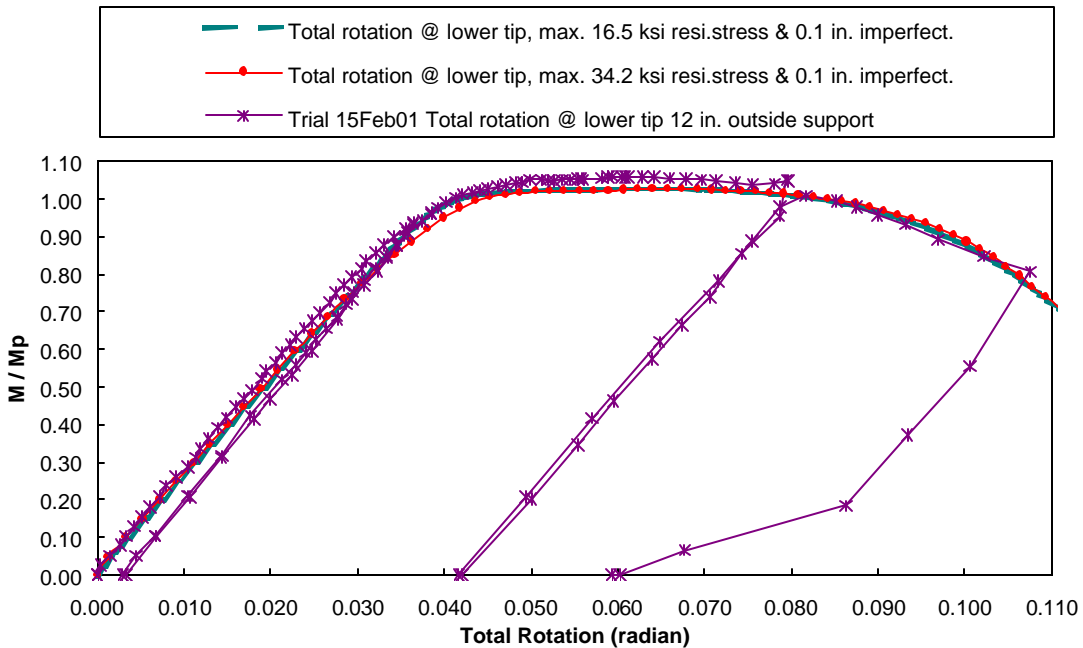


Figure 4.1.7 Effects of Residual Stresses and Initial Imperfection on Numerical Models of Specimen #1 (above) and Specimen #2 (below)

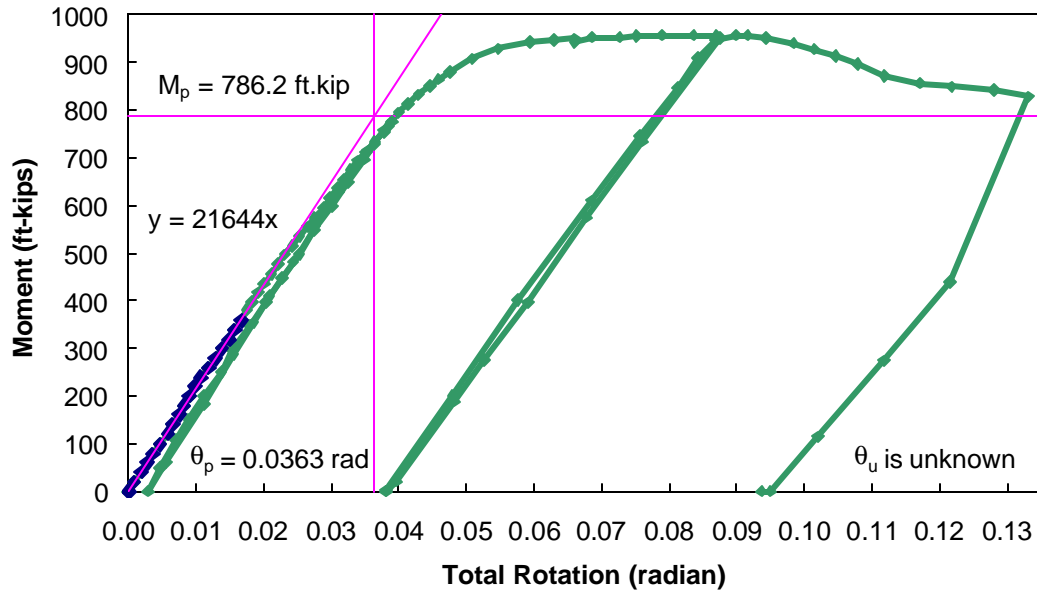
4. 2 Inelastic Moment-Rotation Relationships of the CSU's HPS70W Noncomposite Specimens

The pier moment-rotation behavior of HPS70W I-shape girders was synthetically developed from the response of specimens classified in compact/noncompact categories. For the CSU “nominal compact/noncompact” noncomposite HPS70W girders, the experimental results obtained from girder testing and the numerical results acquired from ABAQUS analyses are very similar. For each of the four CSU's HPS70W girders, the comparisons with AASHTO specifications (AASHTO, 1998 and interims through 2001) consist of a division for “nominal compact/noncompact,” in which the nominal yield stress, $F_y = 70$ ksi, is applied in the AASHTO specifications, and another portion for “actual noncompact” (see Section 2.3.2), in which average tested yield strengths, $F_{yw} = 69.83$ ksi for the web and $F_{yf} = 83.35$ ksi for the flanges, are utilized in the predicting equations.

In detail, Figures 4.2.1 and 4.2.2 display the moment-rotation capacity, R , and the AASHTO predicted comparisons (6.10.10.2.4d (for M/M_p) & 6.10.10.1.2d (for M_{pe})) in both portions of “nominal compact” and “actual noncompact” for Specimen #1. Likewise, the comparisons for Specimen #2 are presented in Figures 4.2.3 and 4.2.4. Similar to the results of Yakel, Mans, and Azizinamini (1999), both girders here do not exhibit the anticipated rotational capacity of three as for compact girders (AISC LRFD specification, 2nd edition 1998). However, the rotation capacity, R , of Specimen #1 can be seen probably greater than three, nominally, while using actual yield strengths it is estimated as 1.44. Besides, Specimen #2 exhibits its inelastic rotational ductility, R , of 2.29, nominally, and 1.34 actual values. The results of inelastic moment-rotation relationship for both compact girders, Specimen #1 and Specimen #2, exceed the current AASHTO specifications (AASHTO interim 2001) and the proposed improved simplified inelastic design predictions (Barth, Hartnagel, White, and Barker, 2001), nominally and actual values. Their moment-rotation responses developed a moment resistance greater than their plastic moment capacities until their inelastic rotations approximately reached 40 mrad and 44 mrad, respectively. These values are much greater than the maximum rotation of 30 mrad now thought necessary for redistribution of moments in bridges (Schilling 1986; Barth, Hartnagel, White, and Barker, 2001).

Figure 4.2.5 displays the AASHTO predicted comparison (6.10.10.2.4d (for M/M_p) & 6.10.10.1.2d (for M_{pe})) for Specimen #3 in both portions of “nominal noncompact,” in which the nominal yield stress, $F_y = 70$ ksi, is applied in the AASHTO specifications, and “actual noncompact,” in which average tested yield strengths, $F_{yw} = 69.83$ ksi for the web and $F_{yf} = 83.35$ ksi for the flanges, are utilized in the predicting equations. The comparisons for Specimen #4 are presented in Figure 4.2.6.

Specimen #1 - "Nominal compact"
Experimental Moment vs. Total Rotation and Rotation Capacity



Specimen #1 - "Actual noncompact"
Experimental Moment vs. Total Rotation and Rotation Capacity

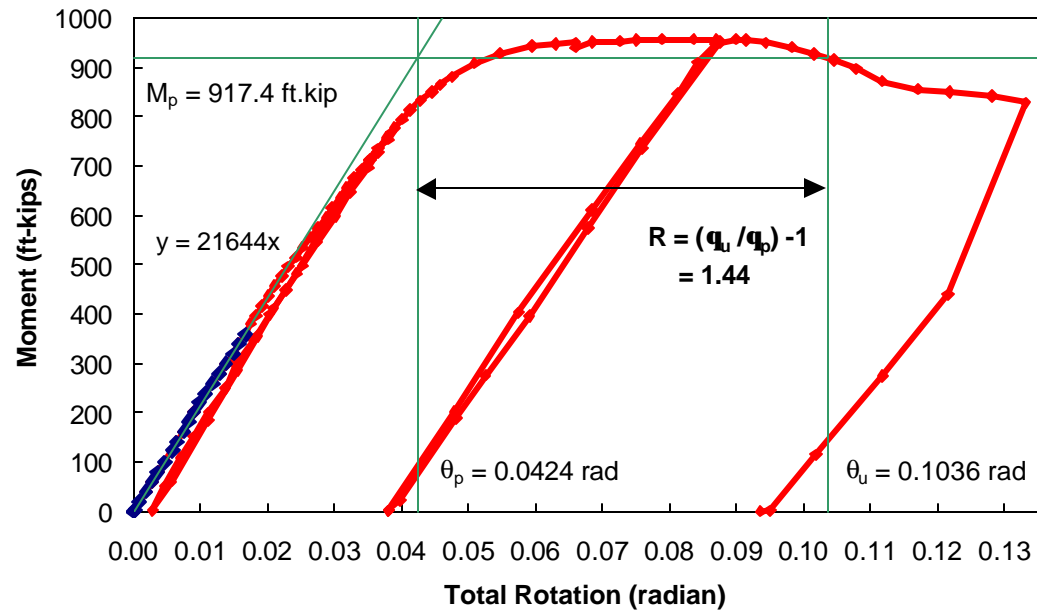


Figure 4.2.1 Nominal and Actual Rotational Capacity, R, of Specimen #1

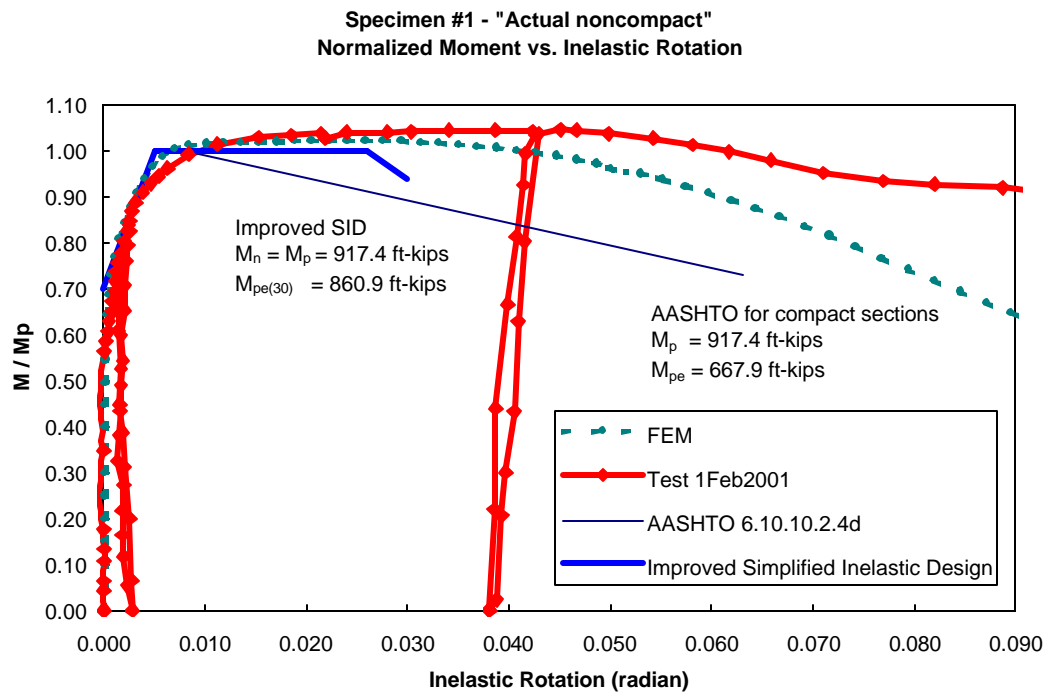
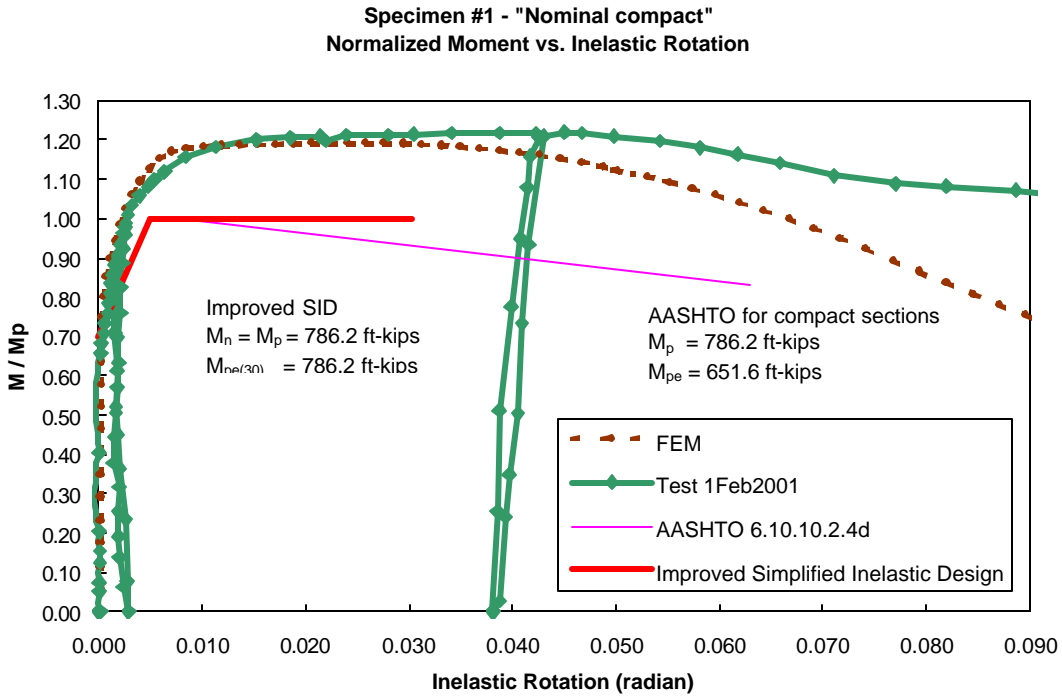
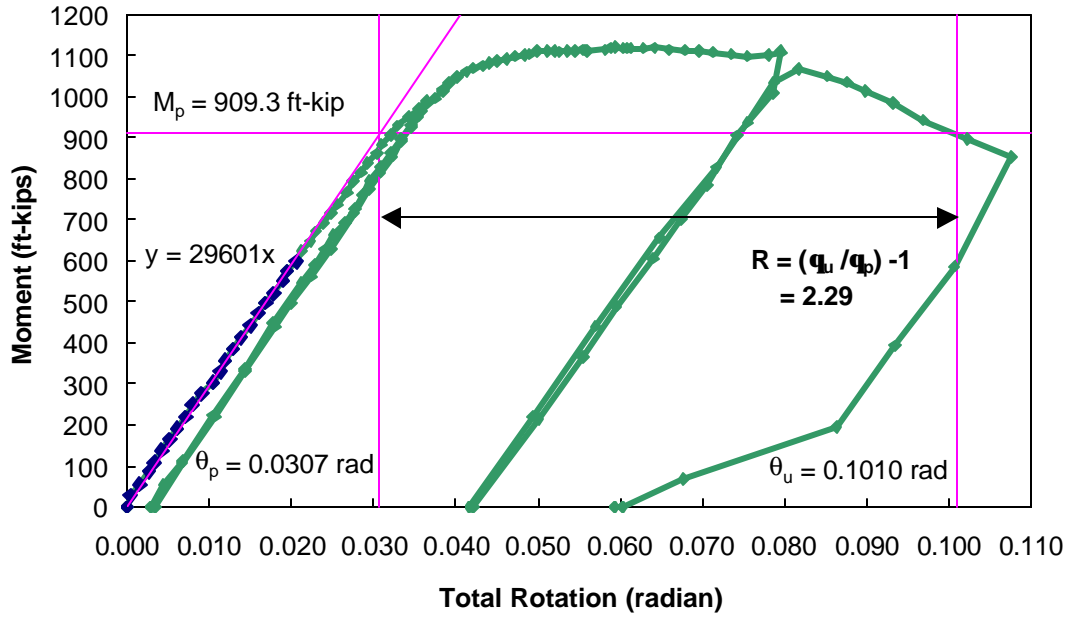


Figure 4.2.2 AASHTO Predicted Comparison for Specimen #1, Nominally (above) and Actually (below)

Specimen #2 - "Nominal compact"
Experimental Moment vs. Total Rotation and Rotation Capacity



Specimen #2 - "Actual noncompact"
Experimental Moment vs. Total Rotation and Rotation Capacity

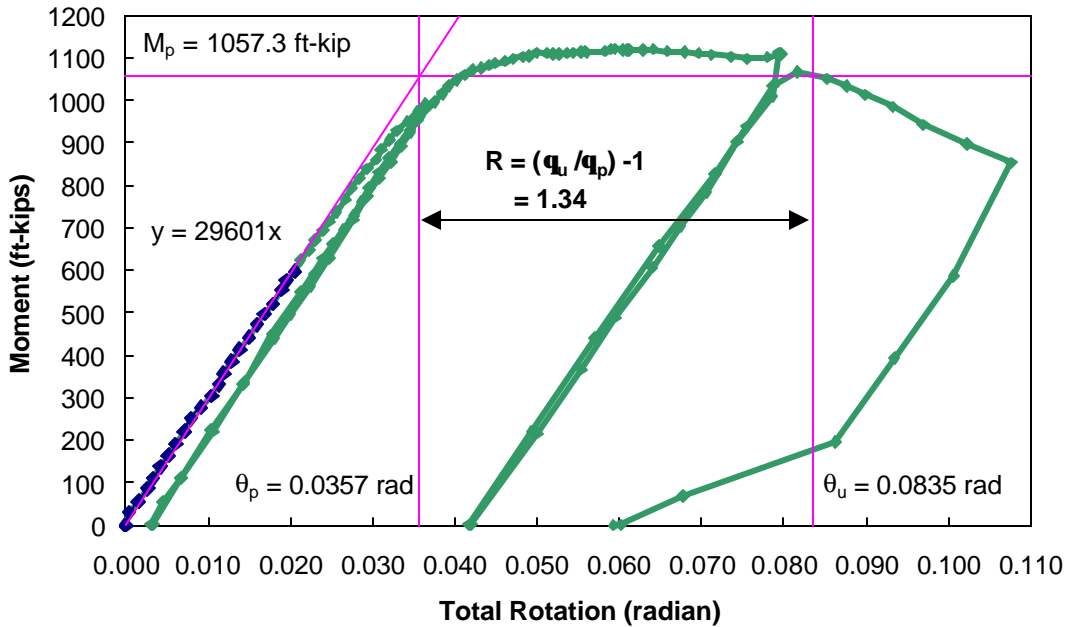


Figure 4.2.3 Nominal and Actual Rotational Capacity, R , of Specimen #2

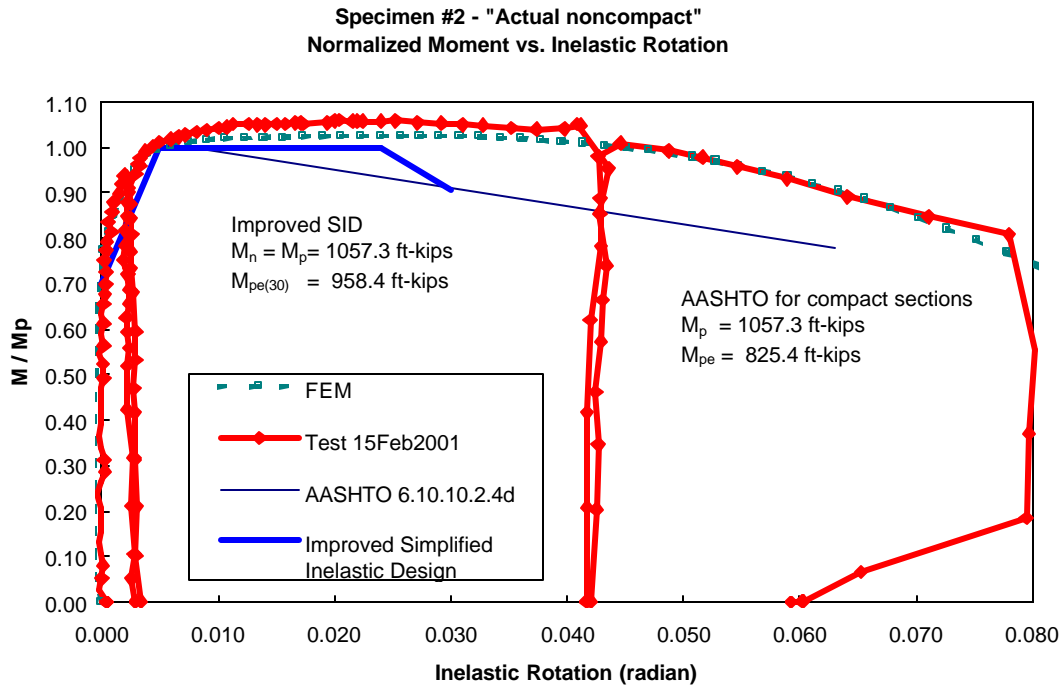
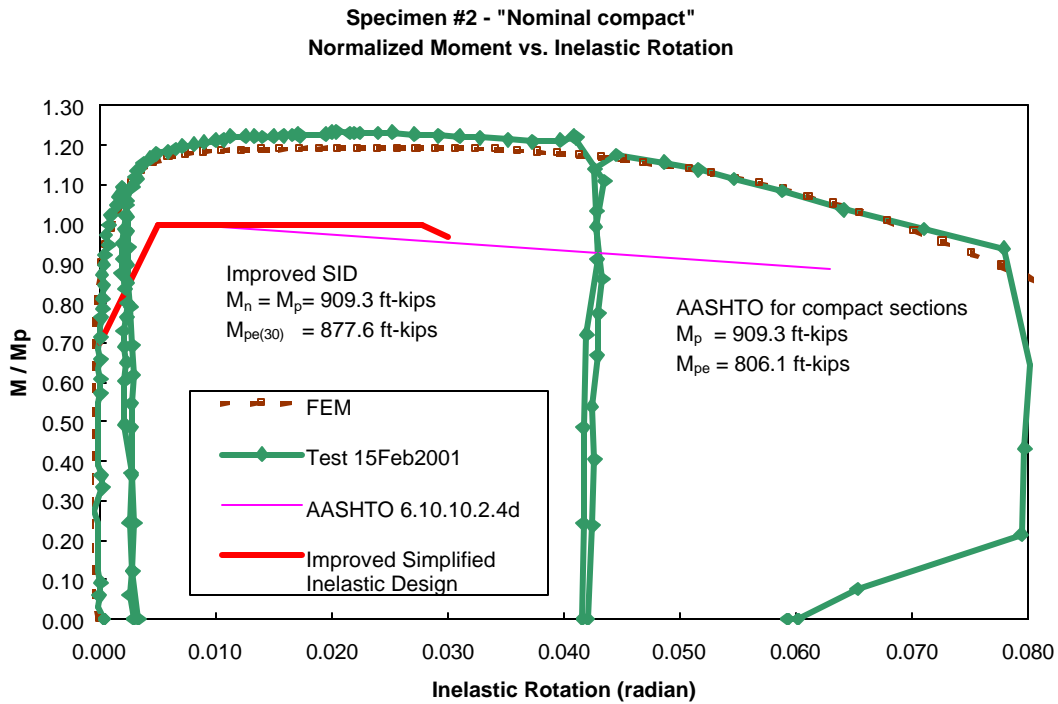


Figure 4.2.4 AASHTO Predicted Comparison for Specimen #2, Nominally (above) and Actually (below)

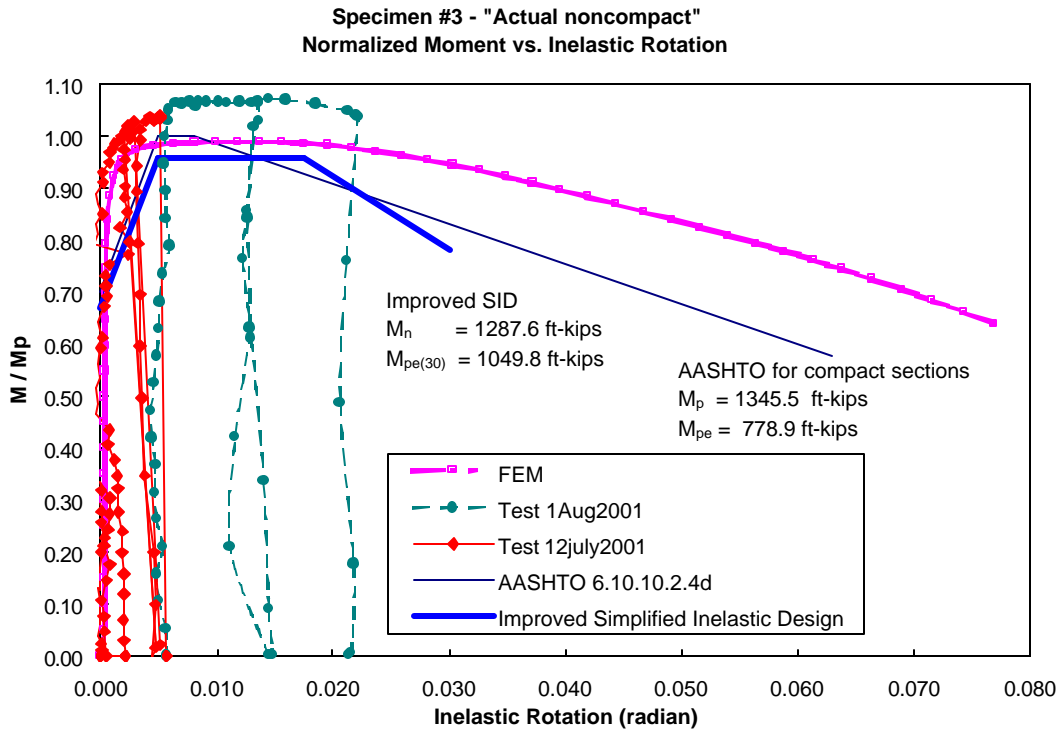
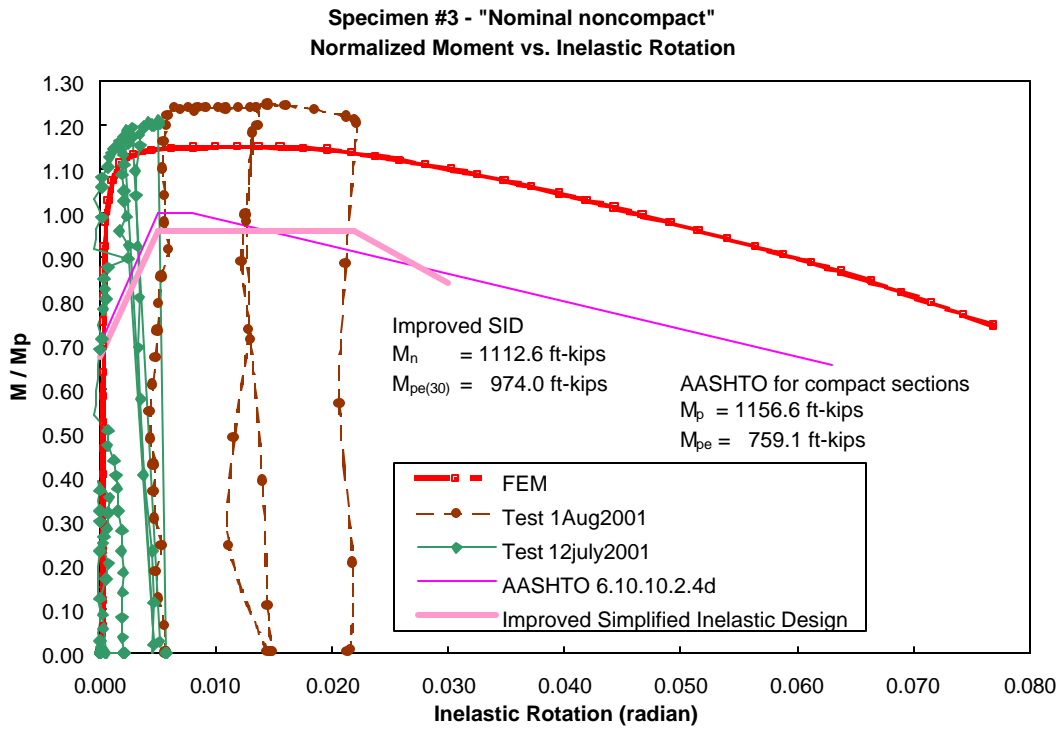
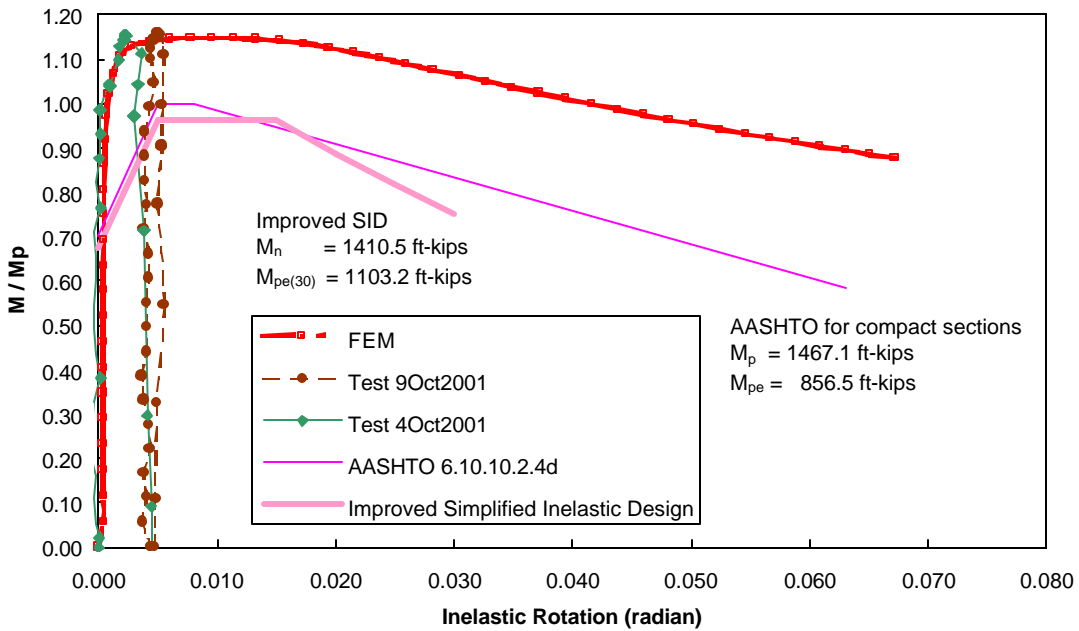


Figure 4.2.5 AASHTO Predicted Comparison for Specimen #3, Nominally (above) and Actually (below)

Specimen #4 - "Nominal noncompact"
Normalized Moment vs. Inelastic Rotation



Specimen #4 - "Actual noncompact"
Normalized Moment vs. Inelastic Rotation

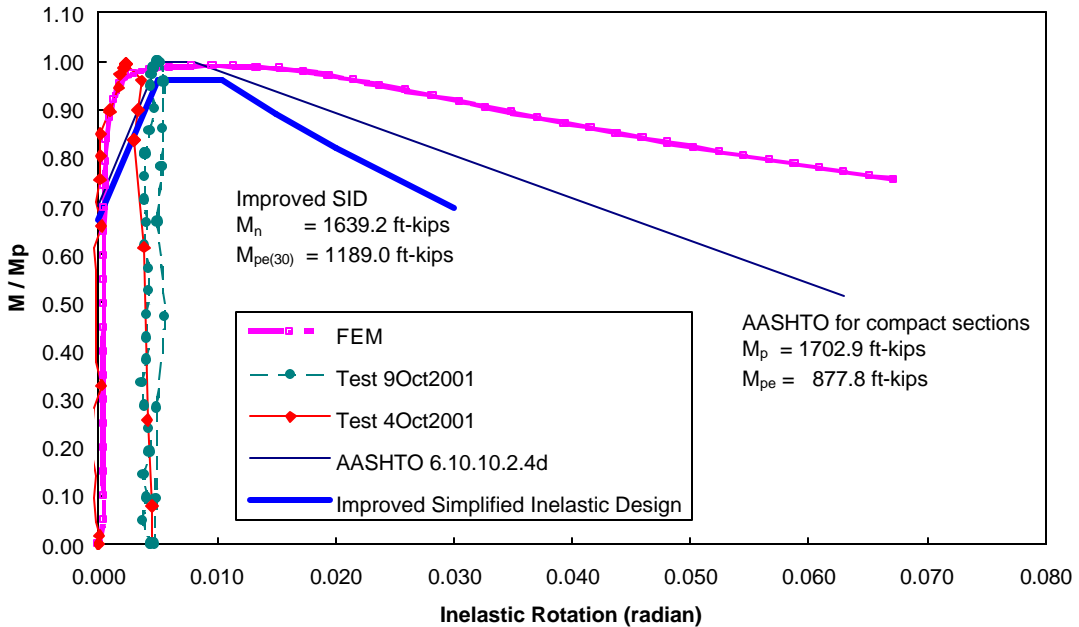


Figure 4.2.6 AASHTO Predicted Comparison for Specimen #4, Nominally (above) and Actually (below)

Nominally, the experimental and numerical results of inelastic moment-rotation relationship for both noncompact specimens, Specimens #3 and #4, exceed the current AASHTO specifications and the proposed improved simplified inelastic design predictions. Actually, the experimental inelastic moment-rotation curves for both specimens still exceed plastic moments, M_p . However, both numerical inelastic moment-rotation curves of the noncompact specimens do not reach the plastic moment, M_p , although they exceed the proposed design moment, M_n , and the proposed effective moment, $M_{pe(30)}$.

In summary, the differences in the plastic moments, M_p , and effective moments, M_{pe} , specified by AASHTO 6.10.10.1.2d (AASHTO interim, 2001) between the nominal and the average of the tested yield stresses are listed in Tables 4.2.1 and 4.2.2. Table 4.2.3 summarizes the AASHTO predicted comparisons for the four CSU girders. Additionally, the differences in the design moments, M_n , and the predicted effective moments, $M_{pe(30)}$, suggested at 30 mrad by the proposed Improved Simplified Inelastic Design (ISID) (Barth, Hartnagel, White, and Barker, 2001) between the nominal and the average of the tested yield stresses are listed in Tables 4.2.4 and 4.2.5. Table 4.2.6 summarizes the proposed ISID predicted comparisons for the four CSU girders.

Table 4.2.1 Nominal Plastic Moment, M_p , and AASHTO Effective Moment, M_{pe}

Specimen #	Nominal M_p (ft-kip)	F_{ye} Comp. Flange (ksi)	F_{ye} Tension Flange (ksi)	F_{ye} Web (ksi)	M_{pe} (ft-kip) (@ 63 mrad on plot)
1	786.2	68.07	55.14	26.51	651.6
2	909.3	68.07	68.07	26.51	806.1
3	1156.6	55.14	45.57	16.61	759.1
4	1467.1	45.57	45.57	15.31	856.5

Table 4.2.2 Actual Plastic Moment, M_p , and AASHTO Effective Moment, M_{pe}

Specimen #	Actual M_p (ft-kip)	F_{ye} Comp. Flange (ksi)	F_{ye} Tension Flange (ksi)	F_{ye} Web (ksi)	M_{pe} (ft-kip) (@ 63 mrad on plot)
1	917.4	70.68	57.25	20.10	667.9
2	1057.3	70.68	70.68	21.35	825.4
3	1345.5	57.25	47.32	12.75	778.9
4	1702.9	47.32	47.32	12.33	877.8

Table 4.2.3 Summary of AASHTO Predicted Comparisons for CSU Girders

		Specimen #1 (nonsym.)	Specimen #2 (symmetric)	Specimen #3 (nonsym.)	Specimen #4 (symmetric)
D_{cp}/D	<i>Nominal</i>	0.594	0.5	0.571	0.5
	<i>Actual</i>	0.612	0.5	0.585	0.5
Classification	<i>Nominal</i>	Compact	Compact	Noncompact	Noncompact
	<i>Actual</i>	Noncompact	Noncompact	Noncompact	Noncompact
Experimental peak vs. M_p	<i>Nominal</i>	1.218	1.234	1.247	Exceed
	<i>Actual</i>	1.044	1.061	1.072	Exceed
Numerical peak vs. M_p	<i>Nominal</i>	1.190	1.192	1.151	1.148
	<i>Actual</i>	1.020	1.025	0.990	0.989
Experimental result vs. M_{pe}	<i>Nominal</i>	Exceed	Exceed	No Data	No Data
	<i>Actual</i>	Exceed	Exceed	No Data	No Data
Numerical result vs. M_{pe}	<i>Nominal</i>	Exceed	Exceed	Exceed	Exceed
	<i>Actual</i>	Exceed	Exceed	Exceed	Exceed

where:

D_{cp} = depth of web in compression, taken at the plastic moment (in.),

D = web depth inside flanges (in.),

M_p = plastic moment, and

M_{pe} = effective moment by AASHTO 6.10.10.1.2d (AASHTO, interim 2001).

Table 4.2.4 Nominal ISID Design Moment, M_n , and Effective Moment, $M_{pe(30)}$

Specimen #	Nominal M_p (ft-kip)	Nominal design moment M_n (ft-kip)	Improved-SID $M_{pe(30)}$ (ft-kip)
1	786.2	786.2	786.2
2	909.3	909.3	877.6
3	1156.6	1112.6	974.0
4	1467.1	1410.5	1103.2

Table 4.2.5 Actual ISID Design Moment, M_n , and Effective Moment, $M_{pe(30)}$

Specimen #	Actual M_p (ft-kip)	Nominal design moment M_n (ft-kip)	Improved-SID $M_{pe(30)}$ (ft-kip)
1	917.4	917.4	860.9
2	1057.3	1057.3	958.4
3	1345.5	1287.6	1049.8
4	1702.9	1634.3	1185.4

Table 4.2.6 Summary of ISID predicted comparisons for CSU girders

		Specimen #1 (nonsym.)	Specimen #2 (symmetric)	Specimen #3 (nonsym.)	Specimen #4 (symmetric)
D_{cp}/D	<i>Nominal</i>	0.594	0.5	0.571	0.5
	<i>Actual</i>	0.612	0.5	0.585	0.5
Classification	<i>Nominal</i>	Compact	Compact	Noncompact	Noncompact
	<i>Actual</i>	Noncompact	Noncompact	Noncompact	Noncompact
Experimental peak vs. M_n	<i>Nominal</i>	1.218	1.234	1.296	1.202
	<i>Actual</i>	1.044	1.061	1.120	1.042
Numerical peak vs. M_n	<i>Nominal</i>	1.190	1.192	1.197	1.195
	<i>Actual</i>	1.020	1.025	1.034	1.030
Experi. result vs. $M_{pe(30)}$	<i>Nominal</i>	1.218	1.264	No Data	No Data
	<i>Actual</i>	1.108	1.160	No Data	No Data
Nume. result vs. $M_{pe(30)}$	<i>Nominal</i>	1.190	1.235	1.306	1.420
	<i>Actual</i>	1.085	1.131	1.212	1.321

where:

D_{cp} = depth of web in compression, taken at the plastic moment (in.),

D = web depth inside flanges (in.),

M_n = Improved Simplified Inelastic Design (ISID) moment, and

$M_{pe(30)}$ = ISID effective moment at inelastic rotation of 30 mrads.

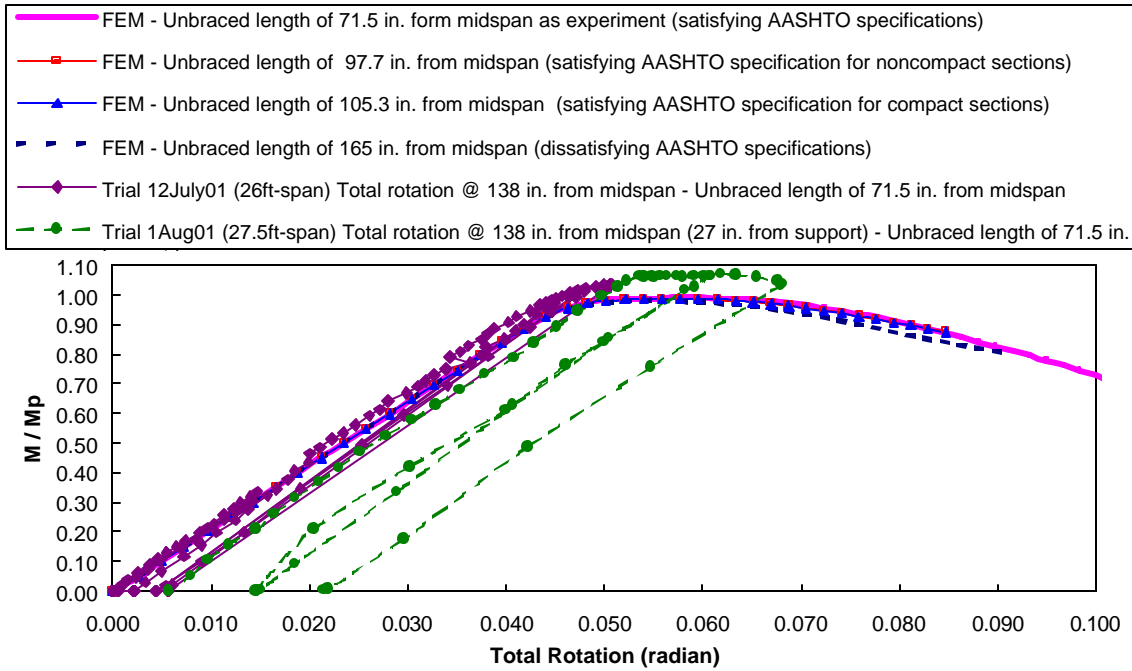
4.3 Bracing Lengths: Numerical Effects for Specimens #3 and Experimental and Numerical Effects for Specimen #4

The effects of lateral bracing lengths on pier moment-rotation behavior of CSU's HPS70W I-shape noncompact girders, Specimen #3 and Specimen #4, will be studied from the response of the specimens with lateral compression-flange bracing classified as either satisfying or dissatisfying the AASHTO requirements (AASHTO, 1998 and interims through 2001) categories. Specimen #3 was experimentally tested with lateral compression-flange bracing configuration at midspan and the supports, which satisfies the AASHTO specifications for both categories of compact and noncompact sections (see Section 3.2.4). Numerically, the finite element model for Specimen #3 was analyzed with four variations either satisfying or dissatisfying the AASHTO specifications of lateral compression-flange bracing. Specimen #4 was experimentally tested and numerically analyzed with two variations either satisfying or dissatisfying the AASHTO specifications of lateral compression-flange bracing.

As displayed in Figure 4.3.1, Specimen #3 with lateral compression-flange bracing satisfying AASHTO specifications experimentally presented the potential to exceed and maintain the plastic moment, M_p , of a noncompact girder. However, the four finite element models either satisfying or dissatisfying the AASHTO specifications of lateral compression-flange bracing for the noncompact girder barely reach the plastic moment, M_p . The numerical models showed an insignificant effect of the studied unbraced lengths, only slightly on the plateau and the decreasing part, on the inelastic moment-rotation relationship for Specimen #3.

The corresponding numerical model of Specimen #4 was analyzed with two bracing configurations as tested in the experimental portion of the research. As shown in Figure 4.3.2, the experimental lateral compression-flange bracing configurations had no effect on the ascending portion and the plateau of the moment-rotation relationship for the noncompact girder Specimen #4. However, the numerical models displayed an insignificant effect of the studied unbraced lengths, only slightly on the decreasing part, on the inelastic moment-rotation relationship for Specimen #4.

Group of Specimen #3 - Bracing length Effects
Normalized Moment vs. Total Rotation



Group of Specimen #3 - Bracing length Effects
Normalized Moment vs. Inelastic Rotation

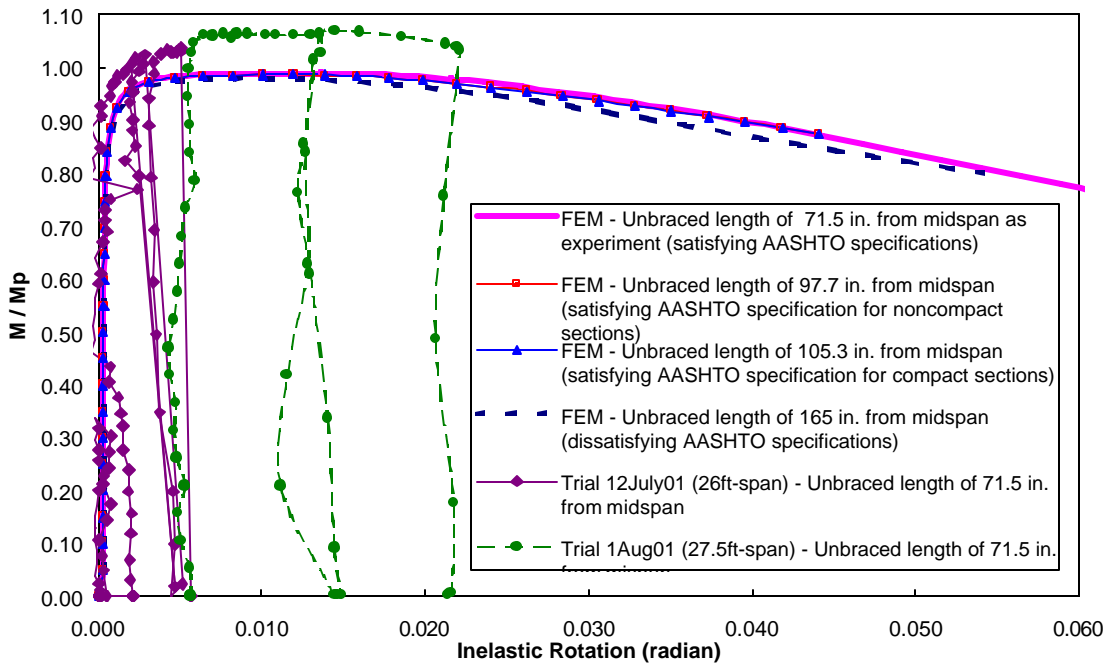
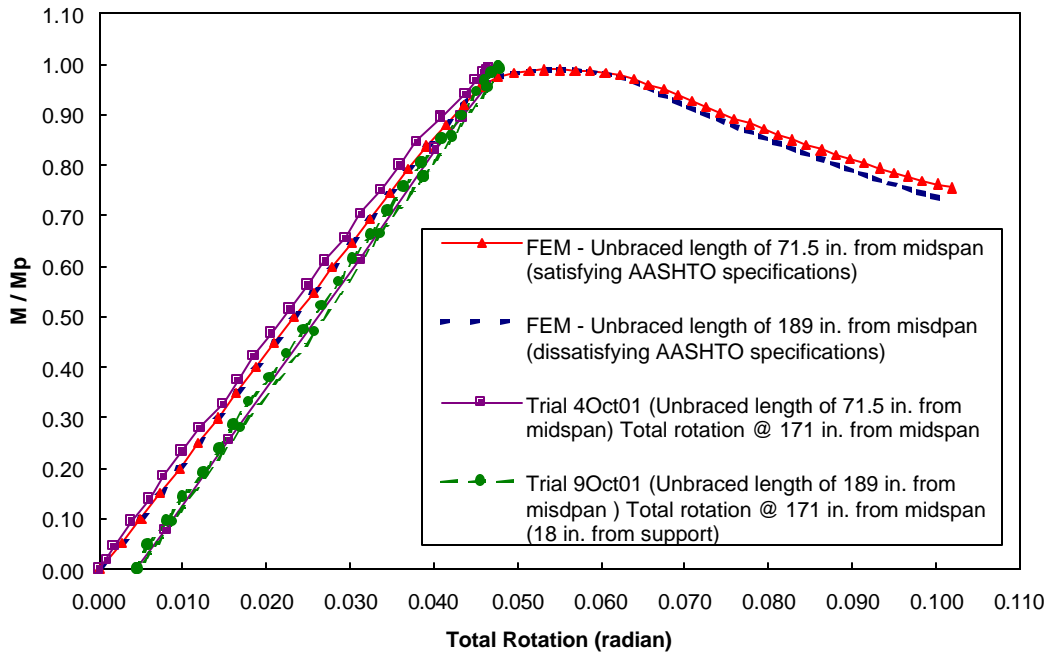


Figure 4.3.1 Numerical Effects of Bracing Lengths on Moment-Rotation Relationship for Specimen #3

Group of Specimen #4 - Bracing length Effects
Normalized Moment vs. Total Rotation



Group of Specimen #4 - Bracing length Effects
Normalized Moment vs. Inelastic Rotation

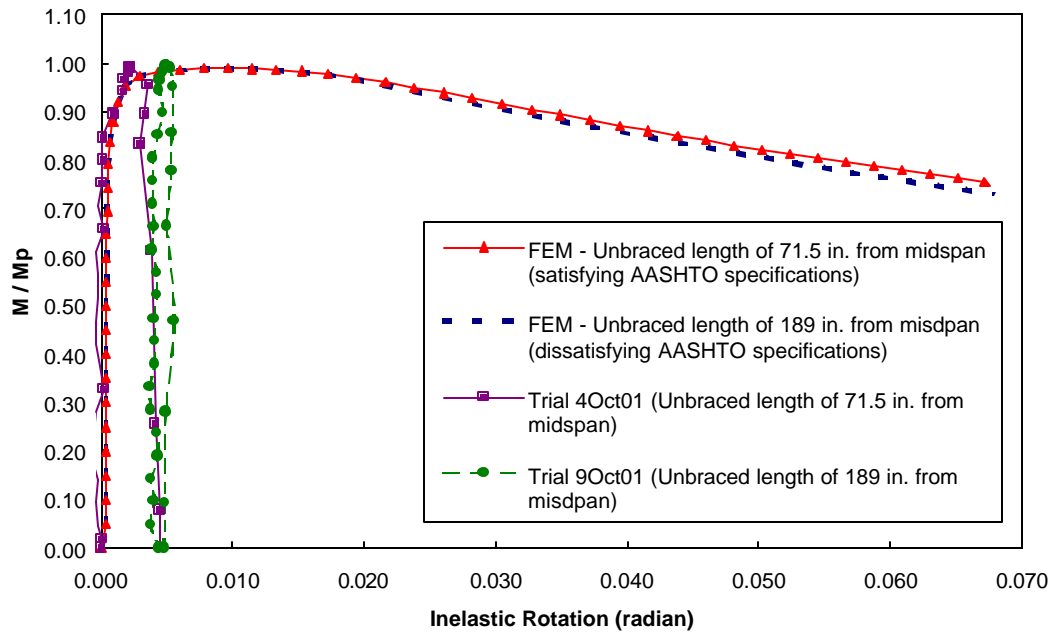


Figure 4.3.2 Experimental and Numerical Effects of Bracing Lengths on Moment-Rotation for Specimen #4

5. SUMMARY AND CONCLUSION

5.1 Introduction

Inelastic analysis and design offers the potential for significant cost savings since it accounts for the reserve strength inherent in continuous-span steel girder bridges. Inelastic procedures allow for the yielding of entire steel cross sections to occur at the interior supports and permit moment-redistribution from negative pier moments to positive moment regions. Since the moment-redistribution causes slight inelastic rotation at the pier regions, small permanent deflection, and some residual moments, the bridge is still serviceable. After an initial overload, deformations stabilize, the structure achieves shakedown, and future loads will be resisted elastically.

A project to study the pier moment-rotation behavior of compact and noncompact high performance steel HPS70W I-girders was conducted at Colorado State University in the context of examining two restrictions for inelastic design of steel bridge girders in the current edition of the AASHTO LRFD bridge design specifications (AASHTO, 1998 and interims through 2001). The first restriction is that inelastic design involving the moment-rotation relationship of steel girders with a yield strength exceeding 50 ksi is prohibited, although, bridge designers are currently allowed to go to plastic moment for I-girders having yield strength of 70 ksi. The second restriction is that the AASHTO LRFD inelastic design methods cannot be used on girders that do not meet the compactness requirements stated in the provisions.

To determine whether or not these restrictions should be modified, an examination of the pier moment-rotation behavior of HPS70W I-shape girders was undertaken through experimental testing and numerical modeling. Large-scale laboratory experiments were performed for noncomposite girders. Finite element models of the tested specimens were then analyzed based on the material inputs obtained from experimental examination of the stress-strain relationships for HPS70W. The inelastic moment-rotation behavior of HPS70W girders was determined both experimentally and numerically.

5.2 Pier Moment-Rotation Behavior of HPS70W I-Girders

The pier moment-rotation behaviors of HPS70W I-shape girders were synthetically developed from the response of specimens classified as either compact or noncompact. For the CSU “nominal compact/noncompact” noncomposite HPS70W girders, the experimental results obtained from girder testing and the numerical results acquired from ABAQUS analyses are very similar and verify each other. For each of the four CSU HPS70W girders, the comparisons with AASHTO specifications (AASHTO 1998 and interims through 2001) consist of a division for “nominal compact/noncompact,” in which the nominal yield stress, $F_y = 70$ ksi, is applied and another portion for “actual noncompact” (see Section 2.3.2), in which average tested yield strengths, $F_{yw} = 69.83$ ksi for the web and $F_{yf} = 83.35$ ksi for the flanges, are utilized in the predicting equations.

In addition, a number of experimental curves and numerical moment-total rotation and moment-inelastic rotation relationships at different locations were compared. At different locations near the supports, the moment-inelastic rotation relationships are numerically nearly identical, although the moment-total rotation relationships are different.

5.2.1 Effect of Compact or Noncompact Steel Section

For both compact girders, Specimen #1 and Specimen #2, the experimental and numerical results of inelastic moment-rotation relationship exceed the current AASHTO specifications and the proposed improved simplified inelastic design predictions (Barth, Hartnagel, White, and Barker, 2001), nominally and with actual yield strengths. Their moment-rotation responses using actual yield strengths developed a moment resistance greater than their plastic moment capacities until their inelastic rotations approximately reached 40 mrad and 44 mrad, respectively. These values are much greater than the maximum rotation of 30 mrad now thought necessary for redistribution of moments in bridges (Schilling, 1986; Barth, Hartnagel, White, and Barker, 2001).

For both noncompact specimens, Specimens #3 and #4, the experimental and numerical results of inelastic moment-rotation relationship nominally exceed the current AASHTO specifications and the proposed improved simplified inelastic design predictions. Using actual yield strengths, the experimental inelastic moment-rotation curves for both specimens still exceed plastic moments, M_p . However, both numerical inelastic moment-rotation curves of the noncompact specimens do not reach the plastic moment, M_p , although using actual yield strengths they exceed the design moment, M_n , and the effective moment, $M_{pe(30)}$, predicted by the proposed improved simplified inelastic design.

5.2.2 Effect of Bracing Length

The effects of lateral bracing lengths on pier moment-rotation behavior of CSU's HPS70W Ishape noncompact girders, Specimen #3 and Specimen #4, were studied from the response of the specimens with lateral compression-flange bracing classified as either satisfying or dissatisfying the AASHTO requirements (AASHTO, 1998 and interims through 2001). Specimen #3 with lateral compression-flange bracing satisfying AASHTO specifications experimentally presented the potential to exceed and maintain the plastic moment, M_p , of a noncompact girder. In addition, the numerical models showed an insignificant effect of the studied unbraced lengths, only slightly affecting the plateau and the decreasing portion, on the inelastic moment-rotation relationship for Specimen #3.

The corresponding numerical model of Specimen #4 was analyzed with two bracing configurations as the experimental portion of the research. The experimental lateral compression-flange bracing configurations had no effect on the ascending portion and the plateau of the moment-rotation relationship for the noncompact girder Specimen #4. However, the numerical models displayed an insignificant effect of the studied unbraced lengths, only slightly affecting the decreasing portion, on the inelastic moment-rotation relationship for Specimen #4.

5.2.3 Effect of Initial Residual Stress and Initial Geometric Imperfection

The effects of initial residual stresses and imperfections on the numerical results are in agreement with previous studies of Yakel, Mans, and Azizinamini (1999) and Zubeck (2000). The effect of residual stresses in the moment-rotation diagram was "rounding off" the curve as the girder yields, even though the magnitude of residual stresses has no effect on the ultimate moment capacity. In addition, what type or how much imperfection was introduced into the model does not influence the results significantly, and thus one does not have to exactly recreate the imperfections found in the real girder. As expected, more imperfection introduced into the model makes the post-plateau portion of the moment-rotation curve descend with steeper slopes, although the influence was not significant.

In this research, the residual stresses are introduced as a constant value over each element. The piecewise-negative residual stress is applied as recommended by Yakel, Mans, and Azizinamini (1999) and Zubeck (2000) for the flanges and web. On the other hand, the maximum-positive residual stress is modified for going from ramp distribution to block distribution. Also, the piecewise residual stress distributions for the flange and the web were also adjusted to account for the tendency of a deeper web having lower residual stresses at the web-flange junction. Furthermore, if the maximum residual stress of +16.5 ksi for welded shape (AISC 1998) is applied, the entire distribution over the web and flanges will be proportioned from the applied maximum value to the corresponding peak of +16.5 ksi.

The imperfection input for numerical analyses was modeled similarly to the study of Yakel, Mans, and Azizinamini (1999), in which the resulting first-eigenvector from the buckling analysis was scaled down such that the maximum displacement was 0.1 inch, and these scaled displacements were superimposed on the original geometry, thus generating a distorted mesh. In this research, an arbitrary combination of eigenvectors, which are weighted descending from the first eigenvector down to the fourth eigenvector (Hibbitt, Karlsson & Sorensen, Inc., 1999), was scaled down such that the maximum combined displacement is from 0.1 to 0.2 inch and then applied as an initial imperfection.

5.3 Summary and Conclusion

This research provides experimental and numerical evidence of the pier moment-rotation behavior of compact and noncompact I-shape HPS70W bridge girders. The experimental and numerical responses agree well and thus validate the numerical model. These results also show that compact/noncompact and composite/noncomposite HPS70W I-girders have the strength and ductility suitable for the application of inelastic analysis and design. For the “nominal compact – actual noncompact” HPS girders (Specimen #1 and Specimen #2), the fact that material failure occurs before geometric failure is also demonstrated. In addition, the effects of the spacing arrangements of the lateral braces were studied for noncompact girders. Spacing arrangements were examined that both did and did not satisfy the AASHTO specifications. The results of the experiments on the lateral compression-flange bracing configurations demonstrate that it is possible to reach the plastic moment, M_p , of the noncompact girder.

This study extends the knowledge base on inelastic moment-rotation behavior of high performance steel HPS70W compact and noncompact I-girders. Such behavior is restricted by current AASHTO specifications (AASHTO, 1998 and interims through 2001). Since HPS70W girders have adequate strength and ductility for inelastic design, it is suggested that the two restrictions for inelastic design of steel bridge girders in the current AASHTO LRFD bridge design specifications (AASHTO, 1998 and interims through 2001) should be modified for such girders. The results of the study also conclude that proposed improved simplified inelastic design (ISID) procedures (Barth, Hartnagel, White, and Barker, 2001) are suitable for high performance steel HPS70W compact and noncompact I-girders.

Nonetheless, this work is not intended to be a determining factor in the development of inelastic bridge design procedures. The results herein are intended to be an objective blind test for the ISID procedures. It is understood that the conclusions herein are based on a limited number of large-scale experiments and numerical models. Future work in large-scale testing on composite HPS70W I-girders is recommended in order to validate the finite element approach for application to the pier moment-rotation behavior of composite sections (Tran and Hartnagel, 2002). The results of this research can be utilized to develop new design provisions, which in turn, can be employed to produce a more consistent, reliable, and economical bridge inventory.

6. REFERENCES

1. American Association of State Highway Transportation Officials (1998 and interims 1999, 2000, and 2001). AASHTO LRFD Bridge Design Specifications, 2nd Edition.
2. American Institute of Steel Construction (1998). AISC Load & Resistance Factor Design, 2nd Edition.
3. Barth, Karl E., White, Donald W. (1998). "Finite Element Evaluation of Pier Moment-Rotation Characteristics in Continuous-span Steel I Girders," Engineering Structures, 20(8) 761-788.
4. Barth, K. E., White, D. W., and Bobb, B. M. (2000). "Negative Bending Resistance of HPS70W Girders." Journal of Construction Steel Research, Elsevier, 53(1), 1-31.
5. Barth, Karl E., Hartnagel, Bryan A., White, Donald W., Barker, Michael G. (December 2001). "Improved Simplified Inelastic Design of Steel I Girder Bridges." Submitted to Journal of Bridge Engineering, ASCE, under review.
6. Bethlehem Lukens Plate, Inc. (1999). High Performance Steels for Bridges: HPS70W - A Technical Overview, 008-HPS-70W Brochure.
7. Griffeth, Michael (March 2001). Experimental Moment-Rotation Tests of HPS70W Steel Girders, Master of Science Thesis, Colorado State University.
8. Hartnagel, Bryan A. (August 1997). Inelastic Design and Experimental Testing of Compact and Noncompact Steel Girder Bridges, Ph.D. dissertation, University of Missouri-Columbia.
9. Hibbitt, Karlsson & Sorensen, Inc. (1997). ABAQUS/Theory Manual, Version 5.7.
10. Hibbitt, Karlsson & Sorensen, Inc. (1999). Buckling, Postbuckling, and Collapse Analysis with ABAQUS.
11. Schilling, Charles G. (July 1986). Exploratory Autostress Girder Designs, Report on Project 188, American Iron and Steel Institute.
12. Schilling, Charles G., Morcos, Sherif S. (July 1988). Moment-Rotation Tests of Steel Girders With Ultracompact Flanges, American Iron and Steel Institute.
13. Tran, An V. (2002). Pier Moment-Rotation Behavior of High Performance Steel HPS70W I Girders, Ph.D. dissertation, Colorado State University, Fort Collins, CO.
14. Tran, An V., Hartnagel, Bryan A. (2002). "Pier Moment-Rotation of HPS 485W I Bridge Girders." Submitted to Journal of Bridge Engineering, ASCE, under review.
15. White, Donald W., Barth, Karl E., Bobb, Betsy M. (December 1998). Strength and Ductility of HPS70W Girders, Final Report to American Iron and Steel Institute, School of Civil and Environmental Engineering, Georgia Institute of Technology.

16. Yakei, A. J., Mans, P., Azizinamini, A. (November 1999). Flexural Capacity of HPS70W Bridge Girders, National Bridge Research Organization, University of Nebraska-Lincoln.
17. Zubeck, Michael W. (May 2000). Nonlinear Analysis of Intermediate Support Regions of Continuous Span Steel Girders, Ph.D. dissertation, University of Missouri-Columbia.

7. NOTATION

The following symbols are used in this research:

a_r	=	ratio of web compression area to flange compression area, taken at the plastic moment;
b_f, b_{fc}	=	width of compression flange;
D	=	total web depth;
D_c	=	depth of web in compression for elastic section;
D_{cp}	=	depth of web in compression at theoretical plastic-moment capacity;
E	=	elastic modulus;
F_u	=	ultimate strength;
F_y	=	yield stress;
F_{yc}	=	yield stress of compression flange;
F_{yf}	=	yield stress of flange;
F_{ys}	=	yield strength of stiffener;
F_{yt}	=	yield stress of tension flange;
F_{yw}	=	yield stress of web;
I	=	moment of inertia;
L	=	span length;
L_b	=	laterally unsupported length between brace points;
L_p	=	maximum unbraced length;
M	=	internal bending moment;
M_l	=	lower factored moment at either end of the unbraced length;
M_n	=	nominal moment capacity;
M_p	=	cross-section plastic-moment capacity;
M_{pe}	=	effective plastic moment;
$M_{pe(30)}$	=	effective plastic moment corresponding to 30 mrad of plastic rotation;

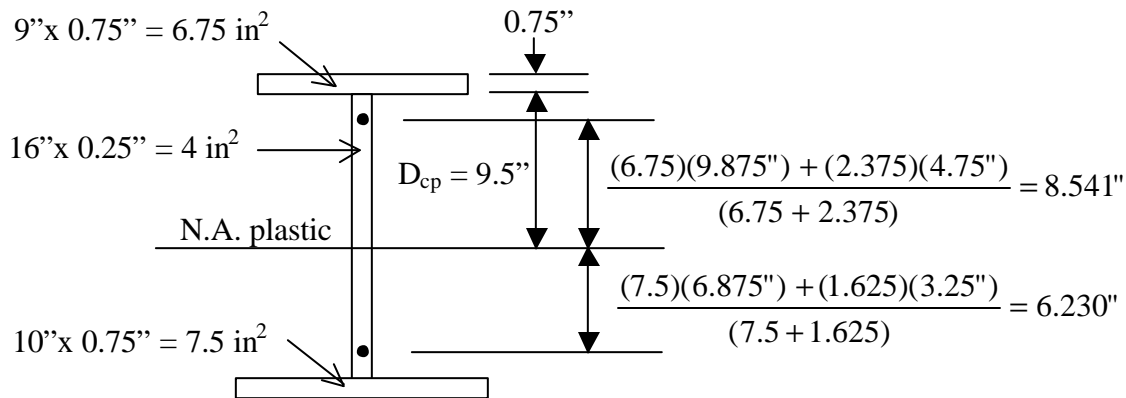
- M_{pf} = flange plastic moment capacity component;
 M_{pw} = web plastic moment capacity component;
 M_y = nominal yield moment capacity;
 M_{yc} = compression flange yield moment capacity;
 P = midspan load;
 R = rotation capacity;
 R_f = flange local buckling reduction factor;
 R_w = web local buckling reduction factor;
 r_t = radius of gyration about the weak bending axis of the area of the compression flange plus 1/3 area of the web in compression;
 r_y = radius of gyration about the weak bending axis of whole section;
 S_{xc} = compression flange elastic section modulus;
 S_{xt} = tension flange elastic section modulus;
 t_f = compression flange thickness;
 t_p = thickness of stiffener;
 t_s = thickness of the concrete slab;
 t_w = web thickness;
 YR = F_y/F_u = yield ratio;
 e_{st}/e_y = ratio of strain at which strain-hardening begins, ϵ_{st} , to yield strain, ϵ_y ;
 θ_{inel} = total inelastic rotation (sum of end inelastic rotations, $\theta_{inel-left}$ and $\theta_{inel-right}$);
 θ_p = plastic rotation;
 θ_{RL} = plastic rotation at which pier-section flexural resistance theoretically will start to decrease with increasing rotations;
 θ_u = the rotation at which the moment capacity returns to M_p after exceeding M_p and deforming past θ_p .

8. APPENDIX

A.1 Plastic moments, M_p , for Specimens #1, #2, #3, and #4

1) Plastic moment & load, M_p & P , of Specimen #1, 19.5 ft-span, simply supported

a) If using $F_{yf} = F_{yw} = 70$ ksi



N.A. of plastic section:

$$A_C = A_T$$

$$6.75 \text{ in}^2 + 0.25D_{cp} = 7.5 \text{ in}^2 + (16 - D_{cp})(0.25 \text{ in})$$

$$0.5 D_{cp} = 4.75$$

$$D_{cp} = \underline{9.5 \text{ in}}$$

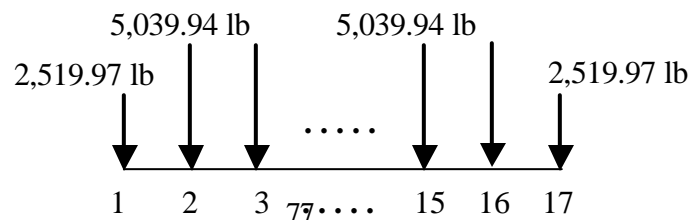
$$F_y = \sigma_y \cdot A = (70 \text{ ksi})(9.125 \text{ in}^2) = 638.75 \text{ K}$$

$$M_p = F_y \cdot l_a = (638.75 \text{ K})(8.541" + 6.230") = 9,434.7 \text{ K-in} = \underline{786.23 \text{ K-ft}}$$

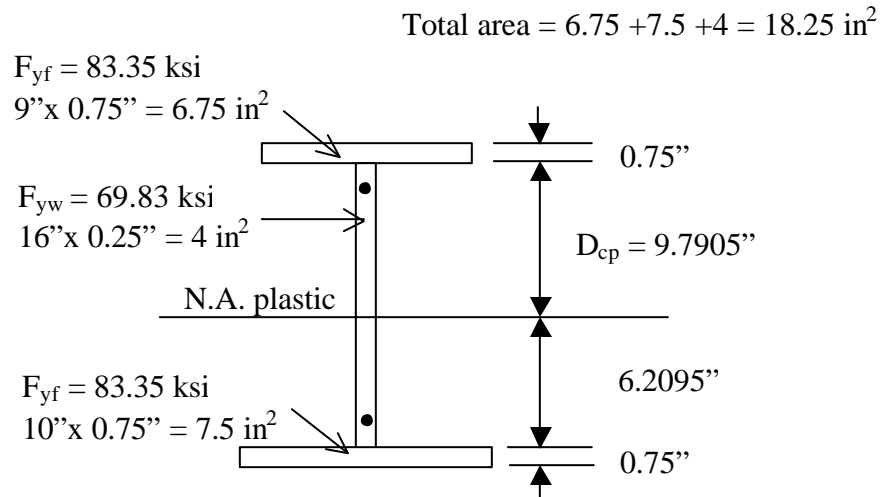
$$P = \frac{4M_p}{L} = \frac{4(786.23 \text{ Kft})}{19.5 \text{ ft}} = \underline{161.278 \text{ K}}$$

$$\text{For half beam \& 16 segments} \Rightarrow \frac{161,278 \text{ lb}}{(2)(16)} = \underline{5,039.94 \text{ lb}}$$

Nodal loads for FEM:



b) If using $F_{yf} = 83.35$ ksi and $F_{yw} = 69.83$ ksi



N.A. of plastic section: $F_C = F_T$

$$F_C = (83.35 \text{ ksi})(6.75 \text{ in}^2) + (69.83 \text{ ksi})(0.25 D_{cp})$$

$$F_T = (69.83 \text{ ksi})(16 - D_{cp})(0.25 \text{ in}) + (83.35 \text{ ksi})(7.5 \text{ in}^2)$$

$$D_{cp} = \underline{9.7905 \text{ in}}$$

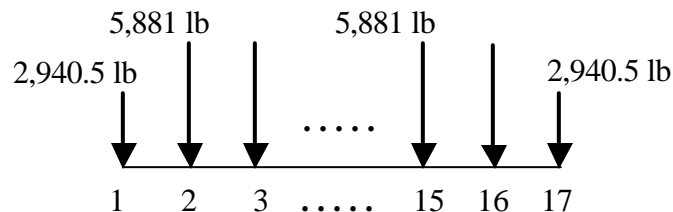
$$M_p = \Sigma(F_i a_i)$$

$$= \left\{ \begin{array}{l} (83.35 \text{ ksi})(6.75 \text{ in}^2)(9.7905'' + 0.75''/2) \\ + (69.83 \text{ ksi})(2.4476 \text{ in}^2)(9.7905''/2) \\ + (69.83 \text{ ksi})(1.5524 \text{ in}^2)(6.2095''/2) \\ + (83.35 \text{ ksi})(7.5 \text{ in}^2)(6.2095'' + 0.75''/2) \end{array} \right\} = \begin{array}{l} 11,009.1 \text{ K-in} \\ \underline{917.4 \text{ K-ft}} \end{array}$$

$$P = \frac{4M_p}{L} = \frac{4(917.4 \text{ Kft})}{19.5 \text{ ft}} = \underline{188.19 \text{ K}}$$

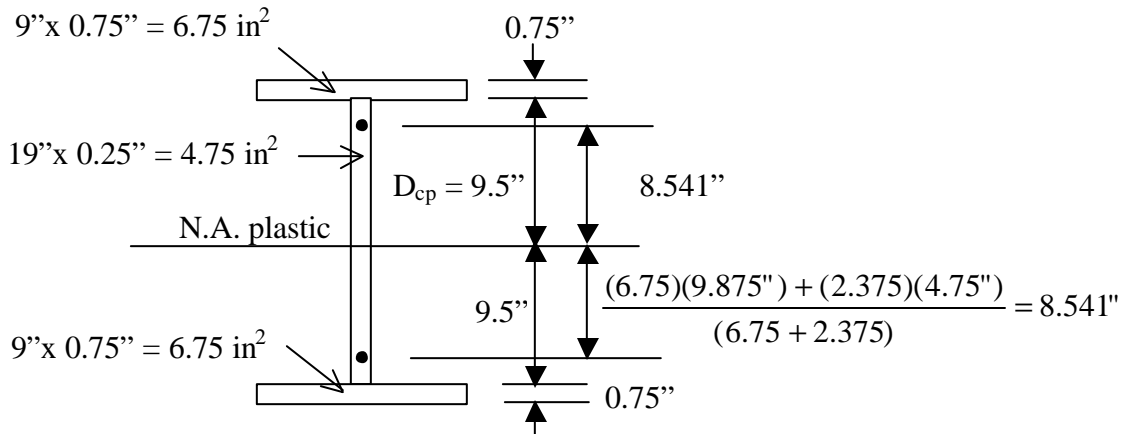
$$\text{For half beam \& 16 segments} \Rightarrow \frac{188,190.5 \text{ lb}}{(2)(16)} = \underline{5,881 \text{ lb}}$$

Nodal loads for FEM:



2) Plastic moment & load, M_p & P , of Specimen #2, 22.0 ft-span, simply supported

a) If using $F_{yf} = F_{yw} = 70$ ksi



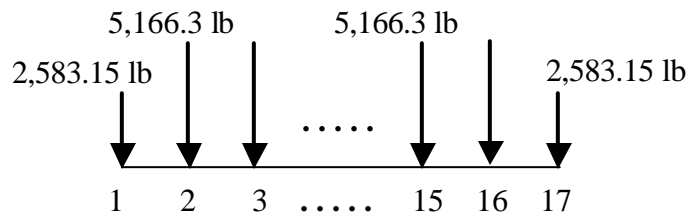
$$F_y = \sigma_y \cdot A = (70 \text{ ksi})(6.75 \text{ in}^2 + 2.375 \text{ in}^2) = 638.75 \text{ K}$$

$$M_p = F_y \cdot I_a = (638.75 \text{ K})(8.541'' + 8.541'') = 10,911 \text{ K-in} = \underline{909.27 \text{ K-ft}}$$

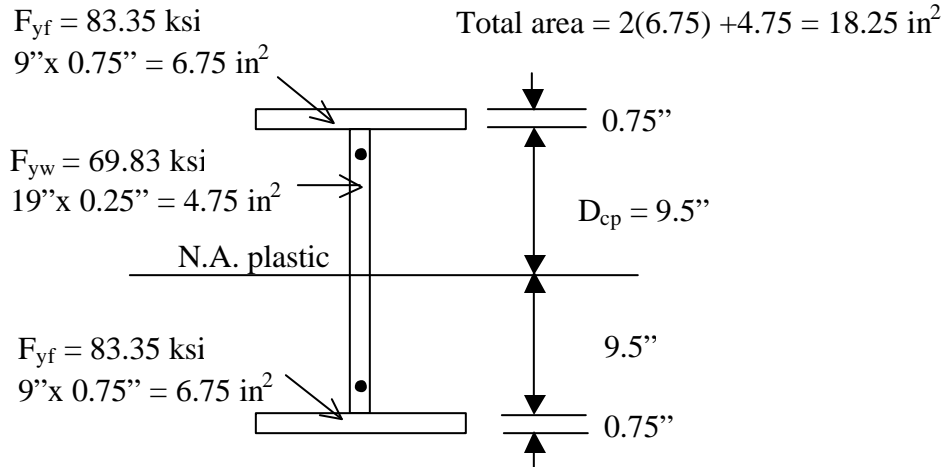
$$P = \frac{4M_p}{L} = \frac{4(909.27 \text{ Kft})}{22 \text{ ft}} = \underline{165.322 \text{ K}}$$

$$\text{For half beam \& 16 segments} \Rightarrow \frac{165,322 \text{ lb}}{(2)(16)} = \underline{5,166.3 \text{ lb}}$$

Nodal loads for FEM:



b) If using $F_{yf} = 83.35 \text{ ksi}$ and $F_{yw} = 69.83 \text{ ksi}$

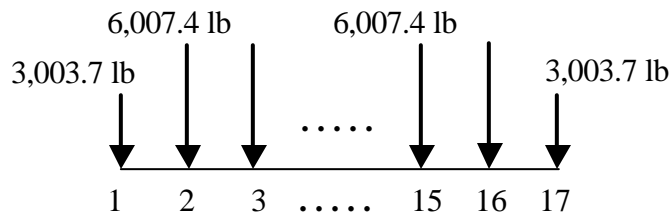


$$\begin{aligned}
 M_p &= \Sigma(F \cdot l \cdot a) \\
 &= 2 \left\{ (83.35 \text{ ksi})(6.75 \text{ in}^2)(9.5'' + 0.75''/2) \right. \\
 &\quad \left. + (69.83 \text{ ksi})(2.375 \text{ in}^2)(4.75'') \right\} = 12,687.7 \text{ K-in} \\
 &= \underline{1,057.3 \text{ K-ft}}
 \end{aligned}$$

$$P = \frac{4M_p}{L} = \frac{4(1,057.3 \text{ Kft})}{22 \text{ ft}} = \underline{192.2 \text{ K}}$$

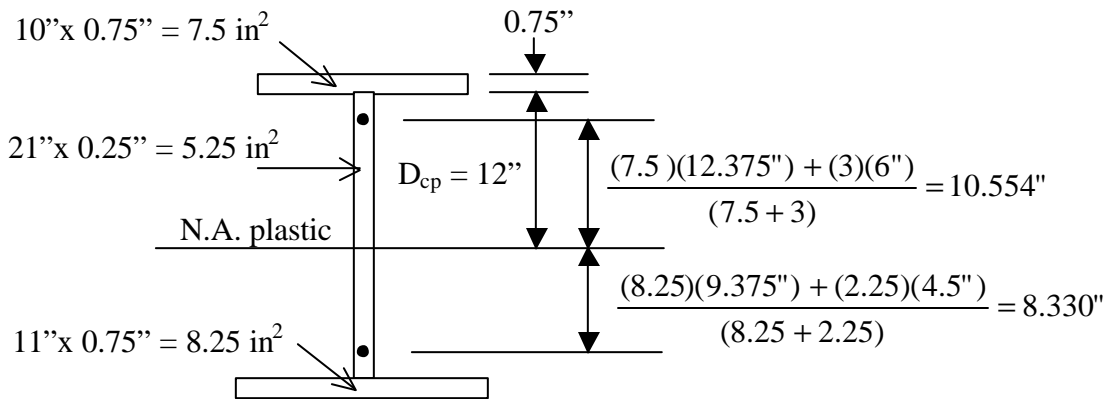
$$\text{For half beam \& 16 segments} \Rightarrow \frac{192,238 \text{ lb}}{(2)(16)} = \underline{6,007.4 \text{ lb}}$$

Nodal loads for FEM:



3) Plastic moment & load, M_p & P , of Specimen #3, 26.0 ft-span (7/12/01 test) and 27.5 ft-span (8/1/01 test), simply supported

a) If using $F_{yf} = F_{yw} = 70$ ksi



N.A. of plastic section:

$$A_C = A_T$$

$$7.5 \text{ in}^2 + 0.25 D_{cp} = 8.25 \text{ in}^2 + (21 - D_{cp})(0.25 \text{ in})$$

$$0.5 D_{cp} = 6 \text{ in.}$$

$$D_{cp} = \underline{12 \text{ in}}$$

$$F_y = \sigma_y \cdot A = (70 \text{ ksi})(10.5 \text{ in}^2) = 735 \text{ K}$$

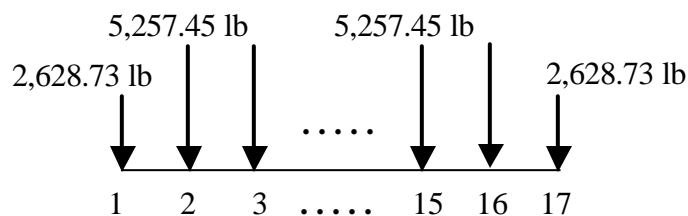
$$M_p = F_y \cdot l_a = (735 \text{ K})(10.554" + 8.330") = 13,879.7 \text{ K-in} = \underline{1,156.64 \text{ K-ft}}$$

- If $L = 26$ ft: $P = \frac{4M_p}{L} = \frac{4(1,156.64 \text{ Kft})}{26 \text{ ft}} = \underline{177.945 \text{ K}}$

- If $L = 27.5$ ft: $P = \frac{4M_p}{L} = \frac{4(1,156.64 \text{ Kft})}{27.5 \text{ ft}} = \underline{168.24 \text{ K}}$

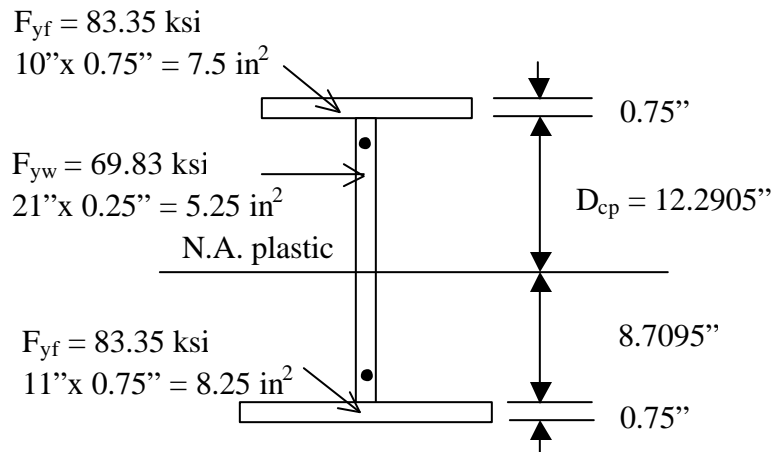
For half beam & 16 segments $\Rightarrow \frac{168,238.6 \text{ lb}}{(2)(16)} = \underline{5,257.45 \text{ lb}}$

Nodal loads for FEM:



b) If using $F_{yf} = 83.35$ ksi and $F_{yw} = 69.83$ ksi

$$\text{Total area} = 7.5 + 8.25 + 5.25 = 21 \text{ in}^2$$



N.A. of plastic section:

$$F_C = F_T$$

$$F_C = (83.35 \text{ ksi})(7.5 \text{ in}^2) + (69.83 \text{ ksi})(0.25 D_{cp})$$

$$F_T = (69.83 \text{ ksi})(21 - D_{cp})(0.25 \text{ in}) + (83.35 \text{ ksi})(8.25 \text{ in}^2)$$

$$D_{cp} = \underline{12.2905 \text{ in}}$$

$$M_p = \Sigma(F.la)$$

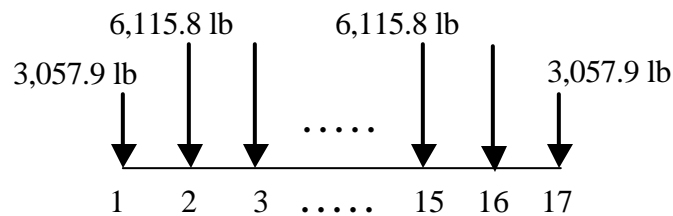
$$= \left\{ \begin{array}{l} (83.35 \text{ ksi})(7.5 \text{ in}^2)(12.2905'' + 0.75''/2) \\ + (69.83 \text{ ksi})(3.0726 \text{ in}^2)(12.2905''/2) \\ + (69.83 \text{ ksi})(2.1774 \text{ in}^2)(8.7095''/2) \\ + (83.35 \text{ ksi})(8.25 \text{ in}^2)(8.7095'' + 0.75''/2) \end{array} \right\} = \begin{array}{l} 16,145.8 \text{ K-in} \\ 1,345.5 \text{ K-ft} \end{array}$$

- If $L = 26$ ft: $P = \frac{4M_p}{L} = \frac{4(1,345.5 \text{ Kft})}{26 \text{ ft}} = \underline{207.0 \text{ K}}$

- If $L = 27.5$ ft: $P = \frac{4M_p}{L} = \frac{4(1,345.5 \text{ Kft})}{27.5 \text{ ft}} = \underline{195.7 \text{ K}}$

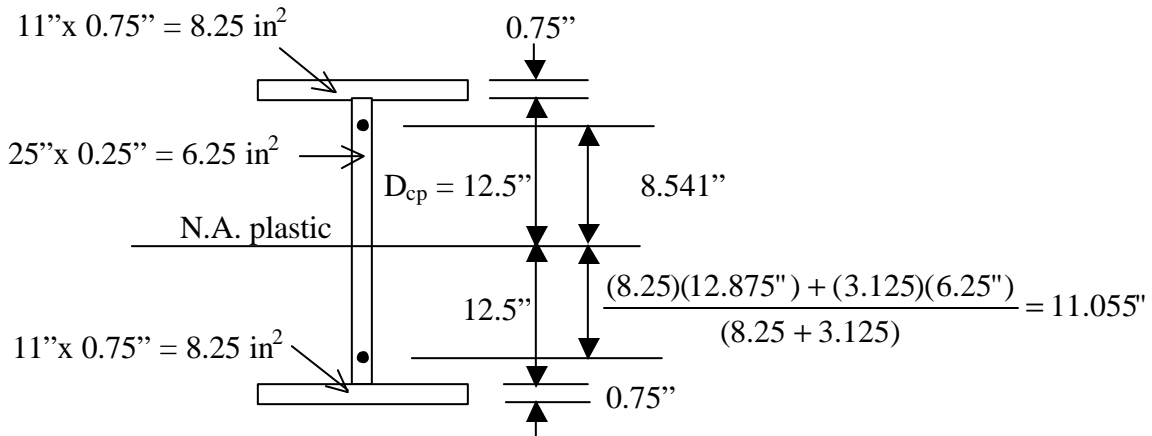
For half beam & 16 segments $\Rightarrow \frac{195,706.4 \text{ lb}}{(2)(16)} = \underline{6,115.8 \text{ lb}}$

Nodal loads for FEM:



4) Plastic moment & load, M_p & P , of Specimen #4, 31.5 ft-span, simply supported

a) If using $F_{yf} = F_{yw} = 70$ ksi



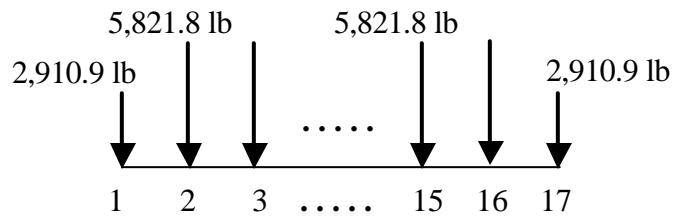
$$F_y = \sigma_y \cdot A = (70 \text{ ksi})(8.25 \text{ in}^2 + 3.125 \text{ in}^2) = 796.25 \text{ K}$$

$$M_p = F_y \cdot I_a = (796.25 \text{ K})(11.055" + 11.055") = 17,605.0 \text{ K-in} = \underline{1,467.08 \text{ K-ft}}$$

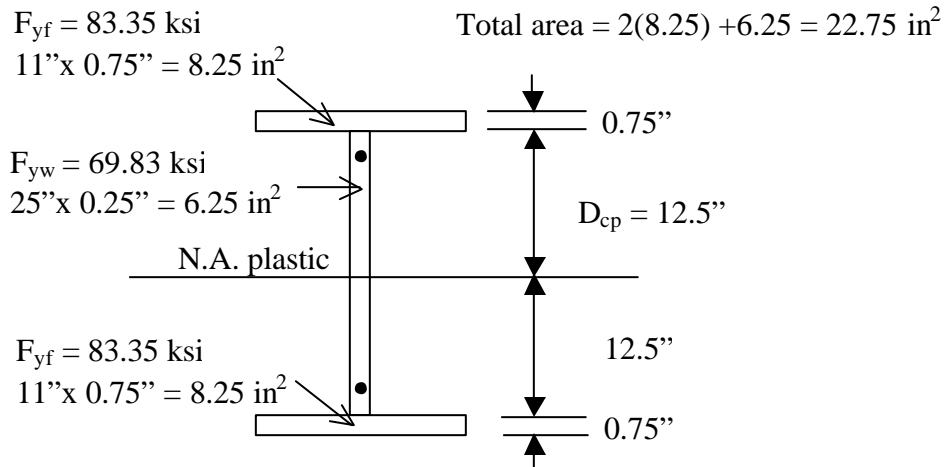
$$P = \frac{4M_p}{L} = \frac{4(1,467.08 \text{ Kft})}{31.5 \text{ ft}} = \underline{186.30 \text{ K}}$$

$$\text{For half beam \& 16 segments} \Rightarrow \frac{186,296 \text{ lb}}{(2)(16)} = \underline{5,821.75 \text{ lb}}$$

Nodal loads for FEM:



b) If using $F_{yf} = 83.35$ ksi and $F_{yw} = 69.83$ ksi



$$\begin{aligned}
 M_p &= \Sigma(F \cdot l \cdot a) \\
 &= 2 \left\{ (83.35 \text{ ksi})(8.25 \text{ in}^2)(12.5'' + 0.75''/2) \right. \\
 &\quad \left. + (69.83 \text{ ksi})(3.125 \text{ in}^2)(6.25'') \right\} = 20,435.34 \text{ K-in} \\
 &= \underline{1,702.9 \text{ K-ft}}
 \end{aligned}$$

$$P = \frac{4M_p}{L} = \frac{4(1,702.9 \text{ Kft})}{31.5 \text{ ft}} = \underline{216.25 \text{ K}}$$

$$\text{For half beam \& 16 segments} \Rightarrow \frac{216,247 \text{ lb}}{(2)(16)} = \underline{6,757.72 \text{ lb}}$$

Nodal loads for FEM:

